Recrystallization and Grain Growth Kinetics in Binary Alpha Titanium-Aluminum Alloys

by

Anna Marie Trump

A dissertation submitted in partial fulfillment
of the requirements for the degree of
Doctor of Philosophy
(Materials Science and Engineering)
in the University of Michigan
2017

Doctoral Committee:

Professor John Allison, Chair
Professor J. Wayne Jones
Associate Professor Veera Sundararaghavan
Professor Katsuyo Thornton

Acknowledgments

This work would never have been possible without so much love, help and support from so many people in my life.

First I would like to thank God for all the blessings He has provided me with throughout my life. I owe all of my successes in life to Him and I hope that everything I do, including my work, is proof of His unfailing love.

I would like to thank Bill Mullins and the Office of Naval Research for the funding that made my research and time here at Michigan possible. I am also extremely thankful for the endless patience, help and support of my adviser, Dr. John Allison. I am thankful that he brought me to Michigan and gave me the opportunity to do this research along with continuously supporting and encouraging me throughout my time here. He never gave up on me, even when I was giving up on myself and has done so much to help further my engineering career. I also must thank my committee members: Dr. Katsuyo Thornton, Dr. Wayne Jones, and Dr. Veera Sundararaghavan. Their advice and various expertise has been vital to guiding and improving my research. I would also like to thank Susan Gentry, Arunabha Roy, Sriram Ganesan, and Pinar Acar for all of their work on the ODF, CPFE and phase field computational modeling that has helped to validate my research. I also need to thank both Peng-Wei Chu and Qianying Shi for performing the STEM and EDS scans presented in this dissertation.

I owe many thanks to all of the members, past and present, of the Allison and Jones research groups who made my day to day work experience in the office and labs more enjoyable. All their help and guidance around the labs along with their friendships will never be forgotten. I also owe thanks to John Lasecki for all of his help with my experimental work, much of which would not have been possible without his knowledge and assistance.

My achievements during my time in graduate school would also not have been possible without the love and support of Sally and Marty Kope, who selflessly dedicated themselves to helping me succeed. They truly turned my life around and they will forever have a place in my heart.

I also owe special thanks to all my close friends who supported me through the highs and lows of graduate school. To my best friend, Kara Krawiec, thank you for your love and friendship throughout the years and especially for your emotional support throughout my entire academic career. To all my Ann Arbor friends, thank you for making my 5 years in Michigan so wonderful. I will never forget all the support you provided to me and all the good times we had.

Lastly, for all of their love and support throughout my life, I must thank my family. Thank you to my brother, Nick Colletti, for always being a best friend. I owe endless gratitude to my loving parents, Jim and Helen Colletti, for the countless sacrifices they have made to get me to where I am today. Finally, all my love to my wonderful husband, Ben, who has always been by my side and with whom I can't wait to venture through the rest of life.

Thank you to everyone who has done so much for me.

Table of Contents

List of Figures

List of Tables

Abstract

Alpha and alpha+beta titanium alloys are used in a variety of important naval and aerospace applications including a wide range of aerospace structural parts and aero-engine parts, such as fan and compressor blades. The production of these parts requires thermomechanical processing where the material undergoes deformation and subsequent annealing, leading to recrystallization and grain growth. Both of these processes have a significant impact on the mechanical properties of the material, such as strength and ductility. Therefore, understanding the kinetics of these processes is crucial to being able to predict the final properties of a material after undergoing a thermomechanical process such as forging. The materials studied in this work are binary alpha Ti-Al alloys that serve as model alloys for the dominant alpha phase in commercial alloys. Three alloys are studied with varying concentrations of aluminum. This allows for the direct quantification of the effect of aluminum content on the kinetics of recrystallization and grain growth. Even though aluminum is the most common alpha stabilizing alloying element used in titanium alloys, the effect of aluminum on these processes has not previously been experimentally investigated.

This work is also part of a larger Integrated Computational Materials Engineering (ICME) effort whose goal is to combine both computational and experimental efforts to develop computationally efficient models that predict materials microstructure and properties based on processing history. The experimental results from this research are used to guide the development of and provide validation of phase field models for recrystallization and grain growth that predict microstructural evolution.

The static recrystallization kinetics are measured using an electron backscatter diffraction (EBSD) technique and a significant retardation in the kinetics is observed with

increasing aluminum concentration. The time to 50% recrystallization ($t_{0.5}$) decreases exponentially with increasing aluminum content. An analytical model is then used to capture these results and successfully predicts the effect of solute concentration on $t_{0.5}$. The model reveals that this solute effect is due to a combination of a decrease in grain boundary mobility and a decrease in driving force with increasing aluminum concentration.

The resulting trends in static recrystallization kinetics are quantified using the JMAK relationship and an Avrami exponent of approximately one is observed for all three alloys. This value differs from the Avrami exponent of three that is predicted based on the assumption of site saturated nucleation and a random distribution of nuclei. It is hypothesized that the observed Avrami exponent is due to microstructural inhomogeneities such as a non-random distribution of nuclei. This hypothesis is supported by quantifying the homogeneity of nuclei distribution by measuring the free surface fraction of grain boundaries between recrystallized and non-recrystallized regions. These results are also validated by incorporating inhomogeneous distributions of stored energy and nuclei into the initial microstructure of phase field simulations for recrystallization.

The grain growth kinetics are then studied by capturing the grain size using polarized optical imaging after annealing at various temperatures and times. Similar to the effect seen in recrystallization, the addition of aluminum significantly slows downs the grain growth kinetics. This is generally attributed to the solute drag effect due to segregation of solute atoms at the grain boundaries, however aluminum segregation is not observed in these alloys. This can be explained by the fact that at higher solute concentrations, solute-solute interactions cause the aluminum atoms to prefer to be near each other in the bulk rather than segregate to the grain boundaries. Therefore, the solute atoms exert a drag force on the grain boundaries by being pushed ahead of a migrating boundary. A linear decrease in mobility is observed with increasing aluminum concentration. This result validates the Cahn model for solute drag, which predicts an inversely proportional relationship between grain boundary mobility and solute concentration regardless of the direction of the interaction energy between the solute atoms and grain boundaries.

Chapter 1. Background and Literature Review

1.1 Integrated Computational Materials Engineering

The goal of the Integrated Computational Materials Engineering (ICME) field is to combine both computational and experimental studies to develop computational tools that will relate materials processing methods to materials structure and properties. These tools are used to accelerate the development of new materials and their manufacturing processes. Decreasing the time and resources needed to develop new materials is important because of the significant economic benefit.

This work is part of an ICME project that focuses on the physical-mechanical metallurgy of α titanium alloys during thermomechanical processing. Microstructural phenomena including texture, recrystallization, grain growth and precipitate formation are quantified as a function of processing parameters and used to predict material properties such as modulus, yield strength, stress-strain response and fatigue strength. These processing-microstructure-properties relationships are integrated into computational models such as crystal plasticity models and phase field models to develop predictive computational tools.

The research described in this dissertation focuses on experimentally quantifying recrystallization, grain growth and texture during deformation and subsequent thermal processing. These results will be used to calibrate and validate a phase field model of recrystallization and grain growth along with crystal plasticity models for texture development.

1.2 Titanium Alloys

1.2.1 Phases and phase transformation

The alpha phase of titanium alloys exhibits a hexagonal close packed (HCP) crystal structure that transforms to the body centered cubic (BCC) beta phase when heated above the alloy's beta transus temperature. Certain alloying elements, referred to as alpha stabilizers, raise the beta transus temperature allowing the alpha phase to be stable at a wider range of temperatures. The most common alpha stabilizer is aluminum (the Ti-Al phase diagram is shown in Figure 1) while others include oxygen, nitrogen, and carbon. Beta stabilizers lower the beta transus temperature and commonly used beta stabilizers include vanadium, molybdenum, and niobium. [1]

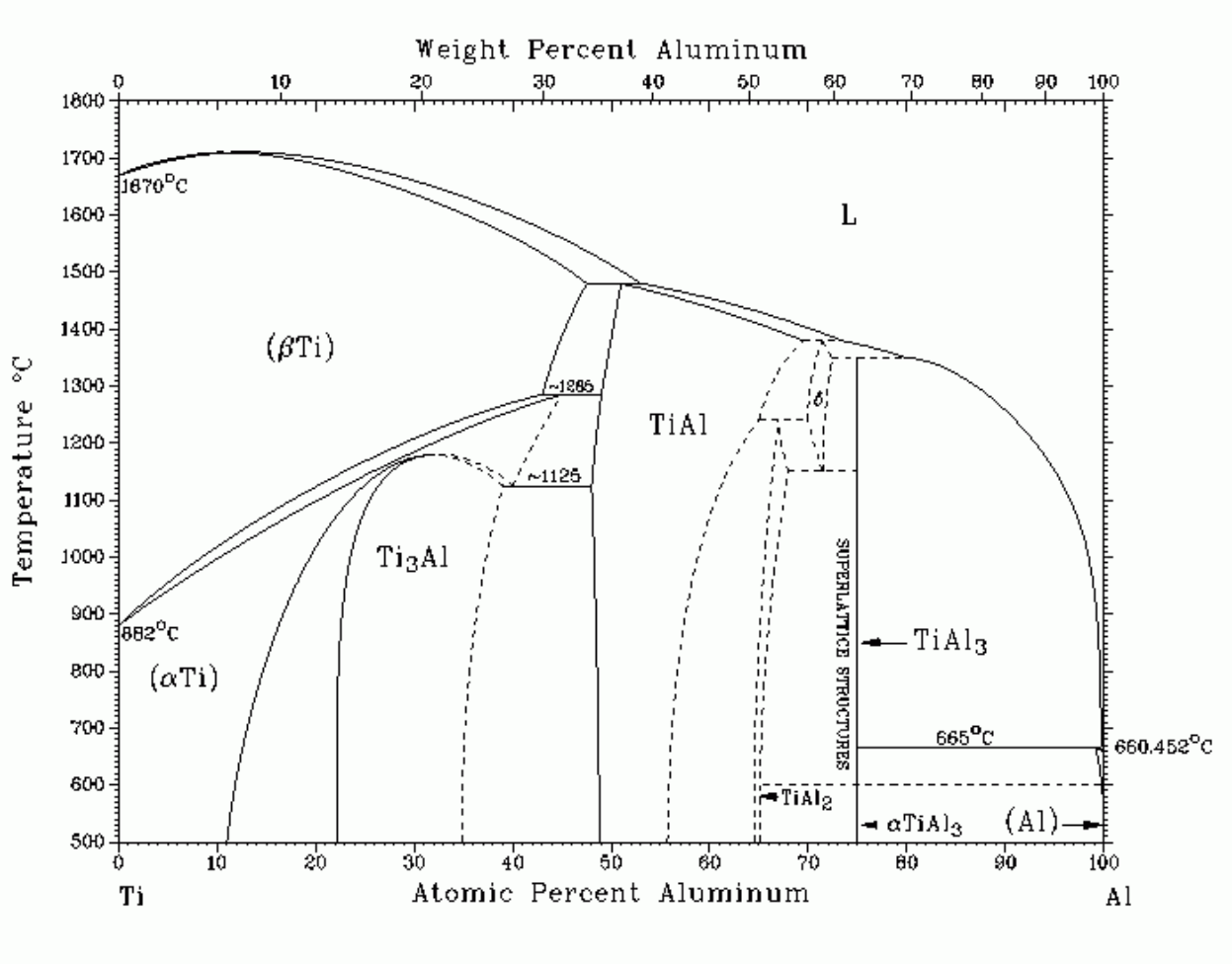

Figure 1. The titanium-aluminum phase diagram [1]

When titanium is cooled from the beta regime to below the beta transus temperature, the phase transformation from beta to alpha occurs. The alpha phase first nucleates along beta grain boundaries and creates a continuous layer of alpha along the grain boundaries. The alpha phase then proceeds to grow from the grain boundaries into the interior of the grains in the form of parallel alpha plates. These parallel plates have the same orientation based on the variant of the Burger's relationship and therefore belong to the same alpha colony. The alpha colony grows into the beta grain until it impinges on another alpha colony that nucleated at a different grain boundary. The faster the cooling rate is, the smaller the width of the alpha plates will be. [1]

1.2.2 Alloy Classification

Titanium alloys can be classified into three groups, alpha, alpha+beta, and beta alloys depending on the concentration of beta stabilizers in the alloys. Commercially pure (CP) titanium and alpha titanium alloys are known for their good corrosion resistance, weldability and fabricability. They are often used for chemical processing equipment because of their corrosion resistance and are also used for tubing, for example in heat exchangers, because of their ease of fabrication. Alpha+beta alloys, such as Ti-6Al-4V, are known for their high strength-weight ratio, good corrosion resistance, and high temperature capability. For these reasons, these alloys are often used in aerospace applications, both structural, such as landing gears and wing attach fittings, and engine parts, such as fan and compressor blades. Beta alloys are known for their high strength and are also used for a variety of aerospace applications such as parts of the cargo handling system, landing gear parts, and springs. [1]

1.2.3 Deformation modes

Pure HCP titanium has a c/a ratio of 1.587 and is very plastically anisotropic. The main slip modes occur on the $\{10\bar{1}0\}$, $\{10\bar{1}1\}$, and $\{0001\}$ planes with the $\langle 11\bar{2}0\rangle$ slip direction, which makes up four independent slip systems (Figure 2). However, according to the Von Mises criterion, five independent slip systems are needed for plastic deformation. Therefore, deformation twinning or <c+a> pyramidal slip must occur. Given the very high critical resolved shear stress of <c+a> slip, about twice that of basal or prismatic slip, deformation twinning is

the predominant final slip mode in pure titanium [1]–[4]. The values of CRSS are highly dependent both on the temperature and alloying concentration. The CRSS for all three types of slip decrease with increasing temperature and the values for basal and prismatic slip converge at high temperatures (Figure 3). Williams et al. [4] investigated the deformation behavior of Ti-Al alloy single crystals and found that the CRSS for both basal and prismatic slip increased with increasing aluminum content as seen in Figure 4. The degree of deformation twinning also depends on alloying concentration. Fitzner et al. [5] investigated the effects of aluminum concentration on the twinning behavior in titanium and found that above 7at%Al (approximately 4wt%Al) twinning is significantly suppressed though not completely removed, which correlated strongly with increasing evidence of short range ordering at 7at%Al and above.

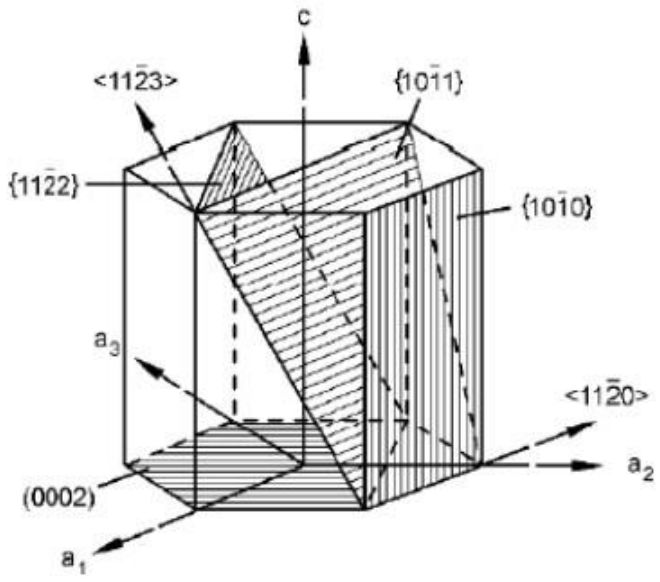

Figure 2. Slip planes and directions in HCP alpha titanium [1]

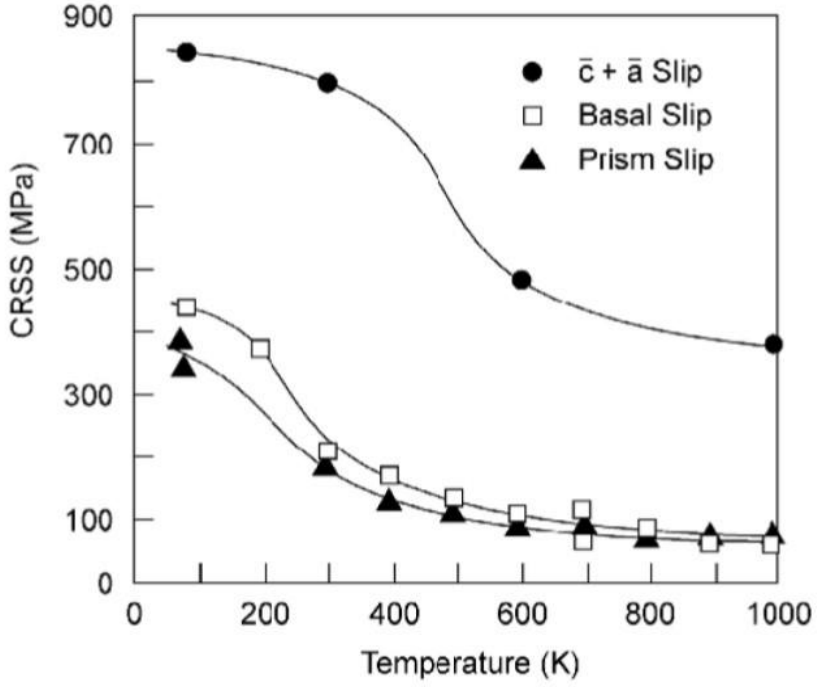

Figure 3. Effect of temperature on CRSS in HCP titanium [1]

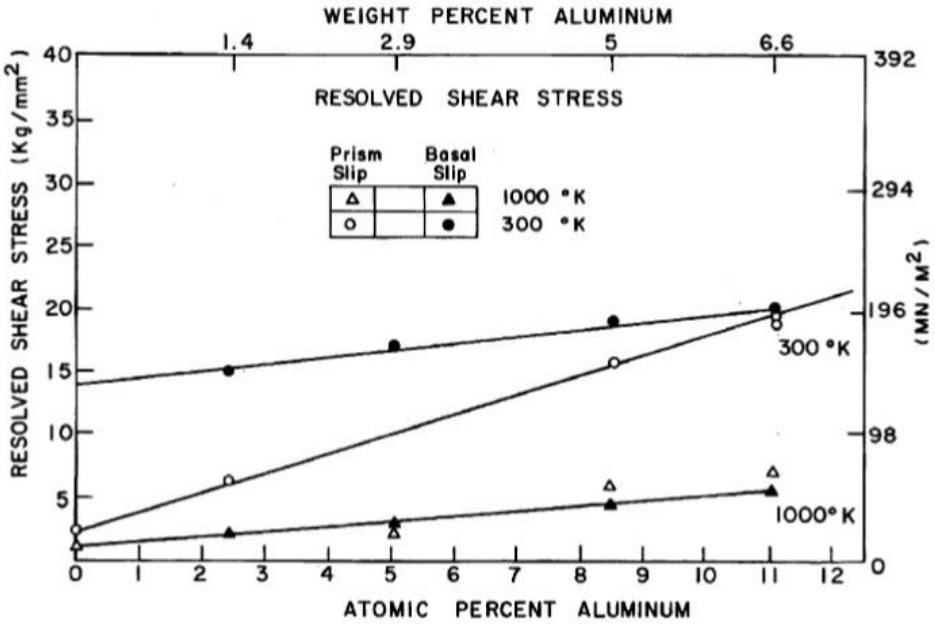

Figure 4. Effect of aluminum concentration on CRSS [4]

1.3 Static Recrystallization

1.3.1 Concept of Recrystallization

When a metal is plastically deformed, energy is stored generally in the form of dislocations. If the material is then subsequently heated, either recovery or recrystallization will occur in order to reduce the stored energy produced by deformation. Recovery occurs when dislocations migrate leading to the annihilation of dislocations of opposite sign and the reorganization of dislocations in cell structures made up of subgrains separated by low angle grain boundaries. The main modes of recovery include dislocation climb and cross slip that occur readily at high temperatures in metals that have high stacking fault energies (SFE). In metals with low or medium stacking fault energies, dislocation climb and cross slip do not occur easily [6] and therefore the nucleation and growth of strain free grains, or recrystallization, will occur in order to decrease the dislocation density and overall energy [7].

Pure titanium is considered to have a high SFE and therefore softens primarily by recovery, depending on processing conditions [8]. However, it has been shown that alloying titanium with aluminum decreases the SFE [9]. Guo et al. developed a relationship between SFE and aluminum concentration for titanium alloys and determined that increasing the aluminum concentration to 6.3wt% from pure titanium decreased the SFE from 0.30 J/m^2 to 0.134 J/m^2 [10].

Recrystallization can be considered as a results of two processes: nucleation and growth. Nucleation is the development of new, strain free grains within the deformed microstructure. Nucleation generally occurs at inhomogeneities such as grain boundaries and triple junctions because of their high dislocation densities. One of the most accepted nucleation mechanisms is strain induced grain boundary migration (SIBM) [7], [11]. SIBM occurs via the bulging of a subgrain through a prior high angle grain boundary (HAGB). The driving force for this mechanism is the difference in dislocation density between the subgrain and the matrix of the material on the opposing side of the prior grain boundary. The formation and growth of new grains along the prior grain boundaries is referred to as necklacing [7], [12].

The progression of recrystallization is generally represented by plotting the fraction of the microstructure that is recrystallized vs. the annealing time and produces a sigmoidal shaped curve as shown in Figure 5.

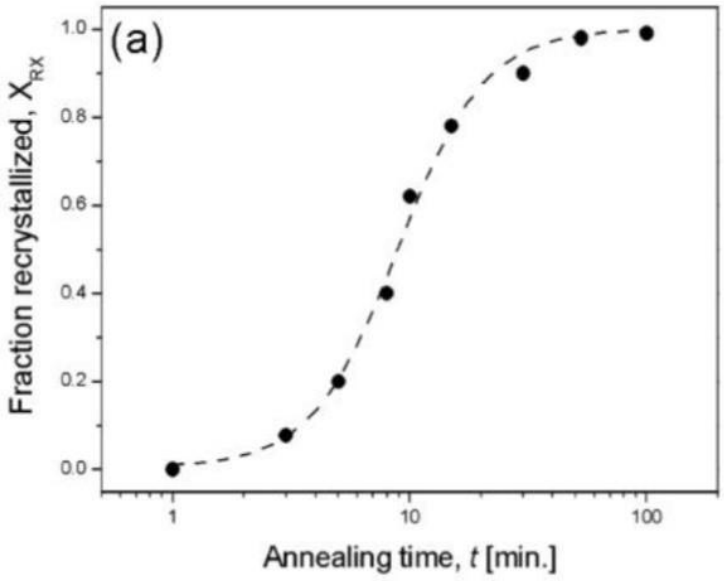

Figure 5. Recrystallization kinetics of 60% cold rolled CP titanium when heat treated at 600°C [13]

The progression begins with an incubation period where nucleation of new grains is beginning to take place, followed by an increasing rate of recrystallization as nuclei begin to grow, then a linear region of rapid recrystallization, and ends with a decreasing rate of recrystallization as the driving force for recrystallization decreases due to reduced dislocation density along with a decrease in the rate of grain growth due to the impingement of grains on each other. The kinetics are often quantified using the JMAK relationship that relates X, the fraction recrystallized, to t, the annealing time [7]:

$$X = 1 - exp\left[-0.693\left(\frac{t}{t_{0.5}}\right)\right]^{n} \quad (1)$$

where $t_{0.5}$ is the time to 50% recrystallization and n is the Avrami exponent.

1.3.2 Factors that Influence Recrystallization

There are a wide range of factors that influence the recrystallization behavior of a metal including various thermomechanical processing variables such as degree of strain, strain rate, deformation temperature and annealing temperature, along with solute concentration.

The thermomechanical processing steps that an alloy undergoes determines the type of recrystallization the material experiences. Annealing at high temperatures after room temperature deformation will lead to static recrystallization (SRX), during which new grains nucleate and grow. Deforming a material at high temperatures leads to dynamic recrystallization (DRX). During DRX, after a critical amount of strain is induced, new grains will nucleate at prior grain boundaries and grow but as the material continues to be deformed the dislocation density of the new grains will increase and the driving force for their growth will decrease and eventually a new set of strain free grains will then nucleate and grow.

The degree of strain that the material experiences before annealing affects the kinetics of static recrystallization. The amount of strain determines the dislocation density, which determines the driving force for recrystallization. Figure 6b demonstrates how higher levels of pre-strain lead to faster recrystallization kinetics as seen by the increased rate of softening [12], [14]. A similar effect is observed when the annealing temperature is changed and the degree of pre-strain is held constant. An increase in annealing temperature leads to increased boundary migration and therefore faster recrystallization kinetics (Figure 6a) [14].

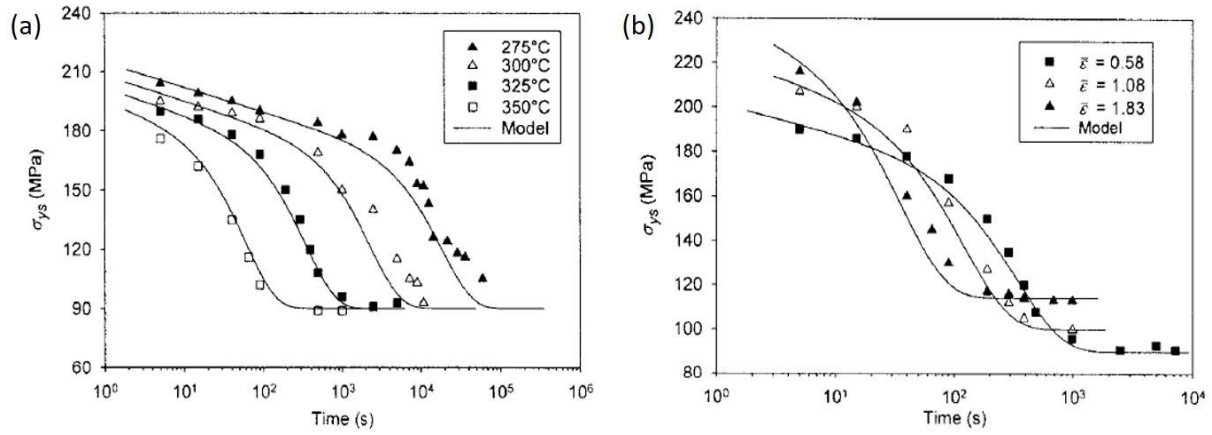

Figure 6. Effect of (a) temperature and (b) pre strain on recrystallization behavior of a cold rolled aluminum alloy annealed at 325°C [14]

Deformation temperature and strain rate during hot working have an impact on both the static and dynamic recrystallization kinetics. A higher strain rate allows less time for recrystallized nuclei to grow before becoming deformed. The deformation of the new grains increases their dislocation density and stored energy causing the driving force for growth to decrease and therefore hinders DRX and increasing the flow stress. This leaves a greater amount of stored energy in the material and therefore increases the driving force for SRX during any subsequent annealing as seen in Figure 7 [15]–[18].

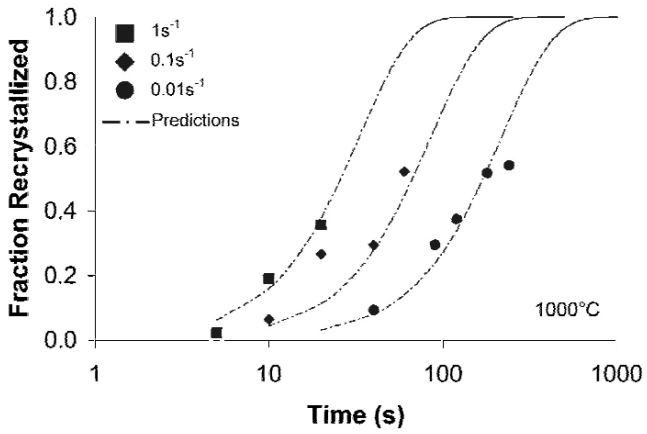

Figure 7. Effect of strain rate on static recrystallization kinetics in a near alpha Ti alloy [15]

Deformation temperature has the opposite effect on flow stress since flow stress decreases with increasing temperature [17], [19]. An increased deformation temperature will increase the driving force for grain boundary migration and therefore allow for a higher degree

of dynamic recovery and recrystallization to occur during the high temperature deformation. This results in a smaller driving force for any subsequent SRX to occur during annealing [20].

The solute concentration of the alloy also has an impact on the recrystallization behavior during thermomechanical processing. In general, solutes are known to hinder recrystallization [21]–[25]. This phenomenon is often attributed to solute drag, meaning solute atoms exert a force on grain boundaries as they migrate and this decreases grain boundary mobility [26]. The effect that solute atoms have on the recrystallization kinetics depends on the solute/solvent pair and the diffusivity of the solute atoms across a grain boundary. Kwon et al. [27] studied the effect of Nb in C-Mn steels on the SRX kinetics and found a retardation in recrystallization kinetics with the addition of Nb as seen in Figure 8. There have been a wide range of studies on solute effects on recrystallization kinetics in steel [28]–[33] but very limited studies quantifying these effects in titanium.

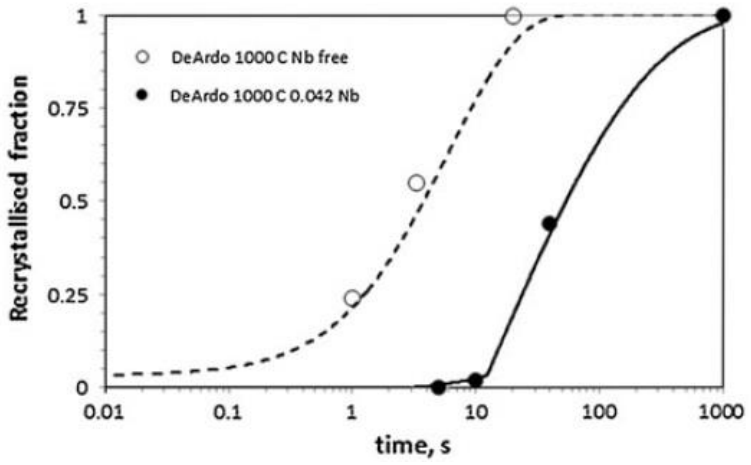

Figure 8. Effect of alloying steel with Nb on SRX kinetics [27]

1.3.3 Static Recrystallization in Titanium

While the microstructural evolution during hot deformation and the dynamic recrystallization kinetics has been widely studied in titanium alloys [8], [34]–[40], the static recrystallization kinetics, and especially the effect of alloying elements on the kinetics, has not been well studied. Contieri et al. [41] investigated static recrystallization in cold worked CP

titanium by periodically characterizing the microstructure during annealing via optical microscopy. Vickers hardness measurements were used to estimate the dislocation density and therefore the driving force, which was found to be 6.67×10^6 J/m^3. Differential scanning calorimetry was used to measure the activation energy for recrystallization, which was found to be 165 kJ/mol. The study of the recrystallization kinetics found an increase in the time to 50% recrystallization with increasing annealing temperature as seen in Figure 9. Chun et al. [42] investigated the effect of deformation temperature on the static recrystallization kinetics in warm-rolled CP titanium and found that, contrary to the expected trend based on recovery, increasing the rolling temperature up to 450°C increases the recrystallization rate. This is explained by an enhanced nucleation rate due to strain localization during deformation. A higher deformation temperature leads to the activation of more diverse slip systems, which creates more high angle grain boundaries and therefore nucleation sites.

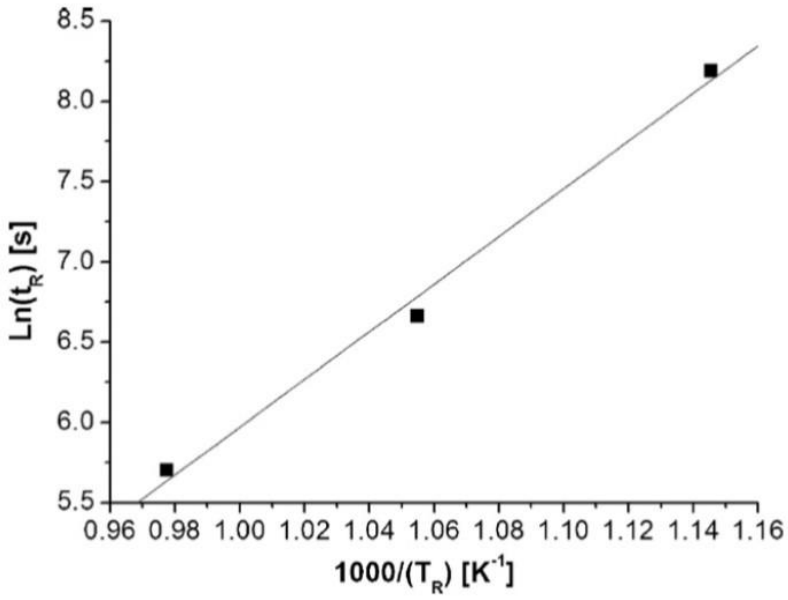

Figure 9. Relationship between time to 50% recrystallization (tR) with annealing temperature (TR) in cold rolled CP titanium [41]

Chun and Semiatin et al. [43] used EBSD maps of cold rolled CP titanium as input to a Monte Carlo simulation for static recrystallization to create realistic starting microstructures based on stored energy distribution (Figure 10a) and texture. The simulations were then run using both random and non-random distributions of stored energy and nuclei to investigate the effects of

these distributions on the resulting kinetics. They found that the recrystallization kinetics deviated from the standard JMAK kinetics when heterogeneous nucleation or an uneven distribution of stored energy was used (Figure 10a-b). Therefore, they concluded that deviations from the JMAK kinetics occurred when the average recrystallization front velocity decreased with time due to these heterogeneities.

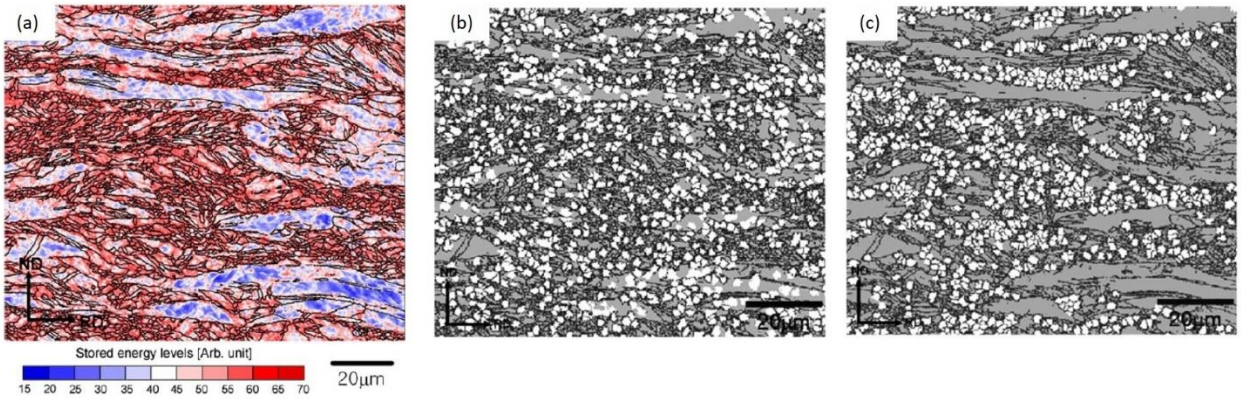

Figure 10. (a) Stored energy map based on EBSD scan of cold rolled CP titanium and corresponding Monte Carlo simulation initial microstructures with (a) random and (b) non-random nucleation [43]

Won et al. [44] investigated the effect of twinning on the static recrystallization kinetics of alpha titanium. They found that even with the same amount of deformation and annealing temperature, that the degree of twinning depended highly on the orientation of the deformation axis. The twin density was very low when the texture of the sample was oriented unfavorably for slip with respect to the deformation axis. Static recrystallization occurred much slower in the samples with lower twin densities, indicating that twinning has an impact on recrystallization kinetics. This is explained by the pile up of dislocations at twin boundaries enhancing the recrystallization rate.

1.3.4 Deformation and Recrystallization Texture in Titanium

The mechanical properties of many metals are dependent on the crystallographic orientation and are thus anisotropic and, in polycrystals, dependent on the overall preferred orientation of the grains or the texture of the material. Some important properties that depend on texture include elastic modulus, Poison's ratio, strength and ductility [45]. For example, the elastic modulus of titanium with respect to a uniaxial stress in the $[2\bar{1}\bar{1}0]$ or

$[01\bar{1}0]$ directions is calculated to be 104 GPa while the elastic modulus with respect to a uniaxial stress in the [0001] direction is calculated to be 146 GPa [46]. Bache et al. [47] studied the tensile responses of Ti-6Al-4V samples with both transverse (samples axis parallel to c-axis) and longitudinal (samples axis perpendicular to c-axis) orientations after cold rolling and found that the transverse samples had significantly higher yield and ultimate tensile strengths. Both deformation and recrystallization annealing during the forging process alter the texture of the material, therefore it is important to study the texture evolution during deformation and recrystallization.

The texture evolution of titanium during deformation has been primarily studied in rolled material. It is observed in HCP metals with c/a ratios below 1.633 such as titanium, that, during rolling, textures form with the basal poles split about 20 - 40° from the normal direction towards the transverse direction and with the $\langle 10\bar{1}0 \rangle$ poles aligned in the rolling direction (Figure 11) [45]. While the rolling texture of titanium is well known, deformation texture is rarely studied during forging, compression or extrusion. Coghe et al. [48] and Warwick et al. [49] studied the room temperature compression deformation behavior of Ti-6Al-4V and CP Ti respectively. When comparing the non-deformed texture to the deformed texture, both studies found an increase in intensity of a basal texture in the compression direction meaning the grains are rotating such that the [0001] direction is aligning with the compression axis. Stark et al. [50] studied the texture formation during hot deformation of γ-TiAl alloys. The phases of the alloys were examined separately and the deformation texture of the α phase was found to be similar of those found by Coghe and Warwick.

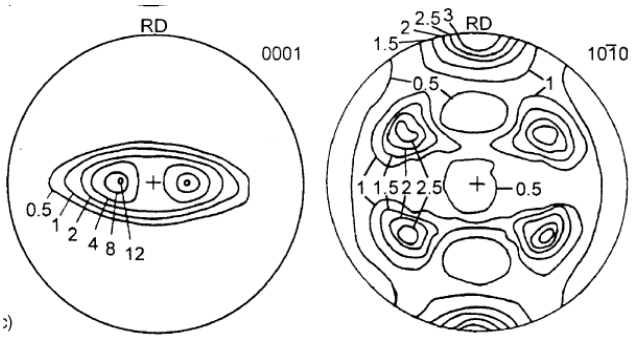

Figure 11. Pole figures for experimental Ti rolling texture [45]

While recrystallization is known to weaken texture that was developed during deformation [51], [52], it does not necessary eliminate texture. Recrystallization after deformation leads to the nucleation and growth of new grains that are not necessarily randomly oriented. There are a number of factors that can influence the resulting recrystallization texture such as the orientation of the nuclei, the growth rate of the new grains, the location of new grains of similar texture relative to each other, and the stored energy of the deformed grains.

1.4 Grain Growth

1.4.1 Concept of Grain Growth

Once the process of recrystallization is complete and the recrystallized grains have replaced all deformed regions, the dislocation density on either side of the grain boundaries will be equal so that the driving force for recrystallization is no longer active. Due to the presence of grain boundaries and the energy penalty that is associated with them, the microstructure is still not in a stable state. With continued annealing, a decrease in the total grain boundary area and therefore overall energy acts as a driving force for grain growth. The kinetics of grain growth are often quantified using the relationship developed by Burke and Turnbull [53] who started with the assumption that the driving pressure that causes grain boundary motion is derived from the grain boundary curvature. This curvature creates a concentration gradient with a higher density of atoms on the inside of the curve compared to the outside. Therefore, atoms will diffuse across the grain boundary from the higher concentration to the lower concentration. This will cause the grains from which the atoms are diffusing from to shrink and the grain the atoms are diffusing into to grow. This process leads to the shrinkage of small grains and growth of large grains, which produces overall grain coarsening. The following parabolic growth law can be used to represent the grain growth kinetics:

$$D - D_0 = kt^n \tag{2}$$

where D is the average grain size, t is the annealing time and n is the grain growth exponent. The theoretical derivation of this relationship results in a grain growth exponent of 0.5, however this analysis assumes that the grain boundary energy for all boundaries is the same. A

value of 0.5 is rarely observed experimentally given that there are multiple factors that can lower the grain growth exponent, including texture, solutes and annealing temperature [7].

1.4.2 Factors that affect grain growth

Since grain growth is a diffusion based process, the annealing temperature will have a significant impact on the kinetics. An increased annealing temperature will increase the diffusivity and therefore lead to faster grain growth kinetics [7]. Two examples of this trend are shown for titanium alloys in Figure 12. Texture will also influence the grain growth kinetics because of the impact texture has on grain boundary energy. A material with a strong texture will have neighboring grains with a more similar orientation than in a material with no texture. Therefore, a material with a strong texture will have lower angle grain boundaries that will have a lower grain boundary energy, which leads to a lower driving force for grain growth [7]. Alloying elements can also affect the grain growth kinetics. Solute atoms tend to decrease the grain boundary mobility due to solute drag and can also decrease the grain boundary energy if solute segregation at the grain boundaries occur [54]. Both of these effects will lead to slower grain growth kinetics and examples of this will be shown in the following sections.

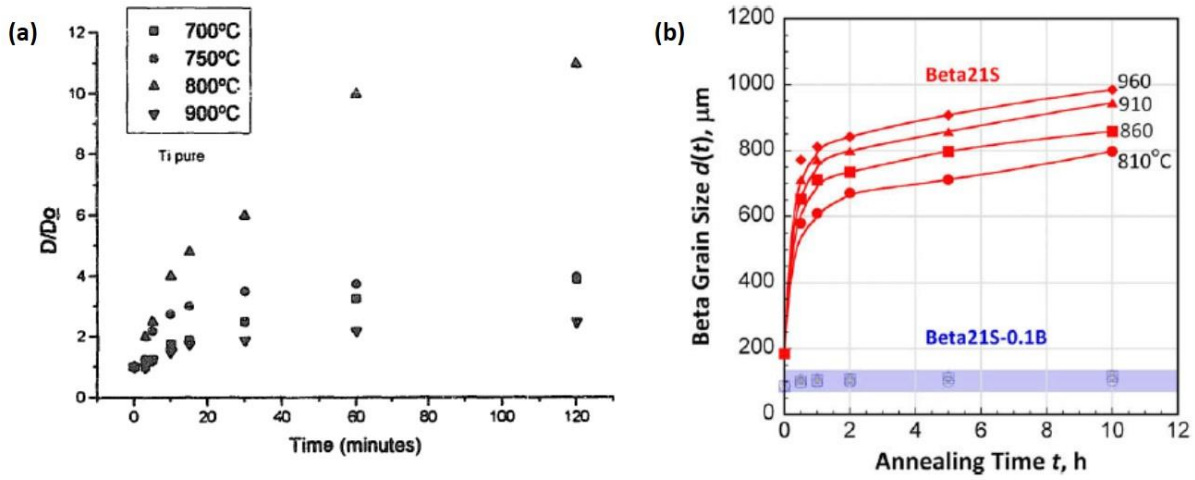

Figure 12. Effect of annealing temperature on grain growth kinetics in (a) pure titanium [55] (D is grain size and D_0 is initial grain size) and (b) a beta titanium alloy [56], showing faster kinetics with increasing annealing temperature

1.4.3 Grain growth in titanium

Grain growth kinetics have been studied in a range of titanium alloys including alpha alloys [55], [57], alpha+beta alloys [57], [58], and beta alloys [56], [59]–[62]. All of these studies consistently see an increase in grain growth kinetics and n values with increasing annealing temperature and those studies that investigate solute effects [55]–[57], [62] all see a decrease in kinetics with the addition of alloying elements. Gil et al. [55], [57] investigated the effect of Pd additions in titanium and found the n value of Ti-0.2Pd to be about half the n value for CP titanium at 700°C. They observed an ideal n value 0.5 for CP titanium, which is explained by their use of high purity and fully recrystallized (therefore low dislocation density) titanium. They also observed very low n values when grain growth was studied right at the beta transus temperature of each alloy. This is caused by the thermal energy from annealing being used for the nucleation of the beta phase instead of grain growth. A much lower activation energy for grain growth was seen for these alloys when heat treated in the beta phase compared to the alpha phase. This is explained by easier diffusivity in the beta phase due to the more open BCC crystal structure. Cherukuri et al. [56] investigated the effects of boron additions in beta titanium alloys and found that the presence of TiB precipitates significantly slowed down the grain growth kinetics due to Zener pinning of the grain boundaries. The average grain growth exponent value seen in titanium experimental studies is approximately 0.3 [57], [59], [61], [62]. An exception is seen from Lee et al. [60] who observed n values of about 0.1-0.2 in a high strength beta alloy. This is attributed to the solute drag due to the high Mo content since Mo has a low diffusivity in titanium. This agrees with the work of Lu et al. [62] who studied binary Ti-Mo alloys and measured an n value of 0.42 in Ti-4Mo and 0.26 in Ti-20Mo. They also saw an increase in activation energy from 65 kJ/mol for Ti-4Mo to 270 kJ/mol for Ti-20Mo. While studies have been done on the solute drag effect of beta stabilizing elements such as Mo, work is yet to been done on alpha stabilizing elements, including aluminum.

1.5 Solute Drag Effect in Recrystallization and Grain Growth

The vast majority of research thus far on the solute drag effect in recrystallization has been done in steels. These studies analyze the effects of a range of alloying elements including

Mn [31], [63], V [29], [64], Nb [28], [32], [33], [65]–[68], Pd [69], Al [25], [70], and C [63]. Roucoules et al. [28] compared the solute drag effects of Nb and Mo on the metadynamic recrystallization (MDRX) of steel and found the kinetics to be slower for the Nb alloyed steel than the Mo alloyed steel. This result is supported by Andrade et al. [29] who found the retardation of the SRX kinetics of steel to be the most significant with Nb additions followed by Mo and V. Zhang et al. [33] found Nb to have a solute drag effect in the DRX kinetics for steel by comparing a Nb alloyed steel with a plain carbon steel as seen in Figure 13. They found that the activation energy required to induce DRX increased from 230 kJ/mol to 318 kJ/mol with the addition of Nb.

Many analytical models that capture the solute drag effect during recrystallization use the relationship developed by Cahn [26] that relates the grain boundary mobility to the solute concentration:

$$M_s = \left(\frac{1}{M_{INT}} + \alpha C_s\right)^{-1} \tag{3}$$

where C_s is the solute concentration, M_{INT} is the intrinsic mobility or the mobility in the solute free material, and α is a constant. The important parameters included in the constant α that govern the solute drag effect are the cross boundary diffusivity and the binding energy of the solute atoms to the grain boundaries. Others use a model developed by Hillert and Sundman [71] for the solute drag effect on grain boundaries in binary alloys. This model uses the amount of energy dissipated due to diffusion within the interface to determine the solute drag force.

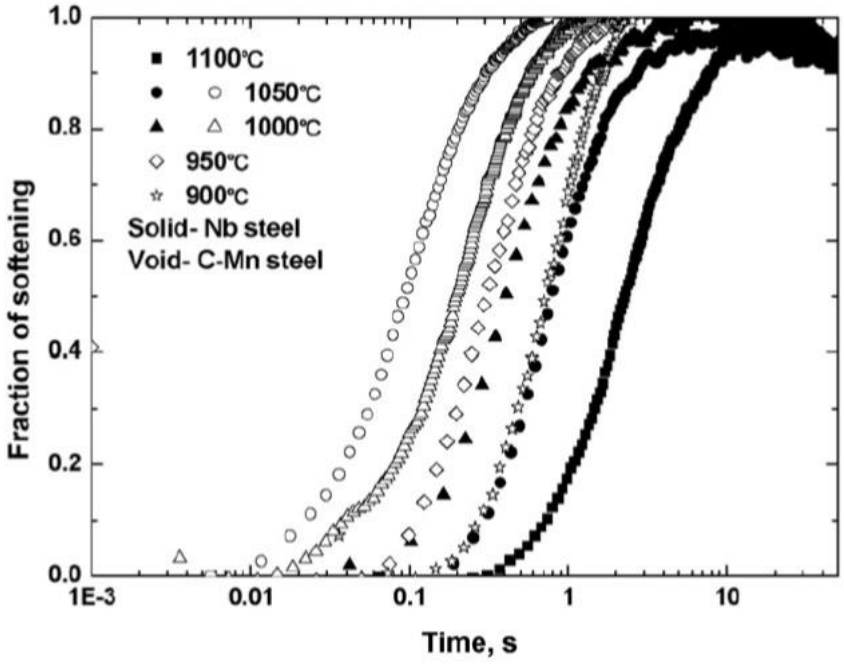

Figure 13. DRX kinetics for a Nb alloyed steel compared to a plain carbon steel showing the effect of solute drag [33]

Similar solute drag effects have been observed on grain growth kinetics as they have on recrystallization kinetics. Examples in titanium alloys were discussed in a previous section and other work has been done in materials such as steel [72]–[75] and magnesium [76]. Yogo et al [75] investigated the drag effect of multiple alloying elements on the grain growth kinetics in steel and found that Nb had a significantly larger effect in slowing down the kinetics than the addition of Si, Mn, Al, or V. Silva et al. [76] studied the addition of Sc to Mg and only observed a very minimal drag effect. This is attributed to the low tendency of Sc atoms to migrate to the grain boundaries due to their small atomic size and mass.

1.6 Summary

In conclusion, there is a gap in titanium literature about the effects of aluminum on recrystallization and grain growth kinetics. This information is crucial given that aluminum is the most commonly used alpha stabilizer and exists in many commercial alloys. Also, the majority of solute drag studies have been on alloys with dilute concentrations of alloying elements and there is a range of models that exist to capture solute drag. The work in this

thesis will focus on quantifying the effect of aluminum on recrystallization and grain growth kinetics in alpha titanium along with investigating the solute drag effect at higher solute concentrations. These results will then be used to validate the Cahn model for solute drag.

1.7 References

[1] G. Lutjering and J. C. Williams, *Titanium*, Second. New York: Springer, 2007.

[2] S. Nemat-Nasser, W. G. Guo, and J. Y. Cheng, "Mechanical Properties and Deformation Mechanisms of a Commercially Pure Titanium," *Acta Mater.*, vol. 47, no. 13, pp. 3705–3720, 1999.

[3] T. Hama, H. Nagao, A. Kobuki, H. Fujimoto, and H. Takuda, "Work-hardening and twinning behaviors in a commercially pure titanium sheet under various loading paths," *Mater. Sci. Eng. A*, vol. 620, pp. 390–398, 2015.

[4] J. C. Williams, R. G. Baggerly, and N. E. Paton, "Deformation Behavior of HCP Ti-Al Alloy Single Crystals," *Metall. Mater. Trans. A*, vol. 33A, no. March, pp. 837–850, 2002.

[5] A. Fitzner, D. G. L. Prakash, J. Quinta, M. Thomas, S. Zhang, J. Kelleher, P. Manuel, M. Preuss, I. Facility, H. Oxford, and D. Ox, "The effect of aluminium on twinning in binary alpha-titanium," *Acta Mater.*, vol. 103, pp. 341–351, 2016.

[6] T. H. Courtney, *Mechanical Behavior of Materials*, 2nd ed. Long Grove, IL: Waveland Pr Inc, 2005.

[7] F. J. Humphreys and M. Hatherly, *Recrystallization and Related Annealing Phenomena*, 2nd ed. Elsevier Science, 2004.

[8] O. De-lai, W. Ke-lu, and C. U. I. Xia, "Dynamic recrystallization of Ti-6Al-2Zr-1Mo-1V in beta forging process," *Trans. Nonferrous Met. Soc. China*, vol. 22, no. 4, pp. 761–767, 2012.

[9] E. A. Metzbower, "Stacking Fault Probability Determinations in HCP Ti-AI Alloys," *Metall. Mater. Trans.*, vol. 2, no. November, pp. 3099–3103, 1971.

[10] Z. Guo, a. P. Miodownik, N. Saunders, and J.-P. Schillé, "Influence of stacking-fault energy on high temperature creep of alpha titanium alloys," *Scr. Mater.*, vol. 54, no. 12, pp. 2175–2178, Jun. 2006.

[11] F. J. Humphreys, "A unified theory of recovery, recrystallization and grain growth, based on the stability and growth of cellular microstructures," *Acta Mater.*, vol. 45, no. 10, pp. 4231–4240, 1997.

[12] E. A. Holm, K. J. Healey, and C. C. Battaile, "Coupled Computer Simulations of Recrystallization in Deformed Polycrystals," *Mater. Sci. Forum*, vol. 467–470, pp. 641–646, 2004.

[13] Y. B. Chun, S. L. Semiatin, and S. K. Hwang, “Monte-Carlo Modeling of Recrystallization Kinetics of Cold-Rolled Titanium,” *Mater. Sci. Forum*, vol. 654–656, pp. 1486–1491, Jun. 2010.

[14] J. Go, W. J. Poole, M. Militzer, and M. A. Wells, “Modelling recovery and recrystallisation during annealing of AA 5754 aluminium alloy,” *Mater. Sci. Technol.*, vol. 19, no. 10, pp. 1361–1368, Oct. 2003.

[15] P. Vo, M. Jahazi, and S. Yue, “FEM Modelling of Recrystallization Behaviour for Near-Alpha Ti Alloy IMI834,” *Adv. Mater. Res.*, vol. 89–91, pp. 592–597, Jan. 2010.

[16] S.-H. Cho, K.-B. Kang, and J. J. Jonas, “The Dynamic, Static and Metadynamic Recrystallization of a Nb-microalloyed Steel.,” *ISIJ Int.*, vol. 41, no. 1, pp. 63–69, 2001.

[17] S. Roy and S. Suwas, “The influence of temperature and strain rate on the deformation response and microstructural evolution during hot compression of a titanium alloy Ti–6Al–4V–0.1B,” *J. Alloys Compd.*, vol. 548, pp. 110–125, Jan. 2013.

[18] P. Vo, M. Jahazi, and S. Yue, “Recrystallization during Thermomechanical Processing of IMI834,” *Metall. Mater. Trans. A*, vol. 39, no. 12, pp. 2965–2980, Sep. 2008.

[19] X. Y. Liu, X. C. Zhao, X. R. Yang, C. Xie, and G. J. Wang, “Compression deformation behaviours of ultrafine and coarse grained commercially pure titanium,” *Mater. Sci. Technol.*, vol. 29, no. 4, pp. 474–479, Apr. 2013.

[20] L. Cheng, H. Chang, B. Tang, H. Kou, and J. Li, “Characteristics of metadynamic recrystallization of a high Nb containing TiAl alloy,” *Mater. Lett.*, vol. 92, pp. 430–432, Feb. 2013.

[21] T. Schambron, L. Chen, T. Gooch, A. Dehghan-Manshadi, and E. V. Pereloma, “Effect of Mo Concentration on Dynamic Recrystallization Behavior of Low Carbon Microalloyed Steels,” *Steel Res. Int.*, vol. 84, no. 12, pp. 1191–1195, Dec. 2013.

[22] E. I. Galindo-Nava, A. Perlade, and P. E. J. Rivera-Díaz-del-Castillo, “A thermostatistical theory for solid solution effects in the hot deformation of alloys: an application to low-alloy steels,” *Model. Simul. Mater. Sci. Eng.*, vol. 22, no. 1, p. 015009, Jan. 2014.

[23] H. S. Zurob, G. Zhu, S. V. Subramanian, G. R. Purdy, C. R. Hutchinson, and Y. Bréchet, “Analysis of Mn Effect on Recrystallization Kinetics in High Nb Steels,” *Mater. Sci. Forum*, vol. 500–501, pp. 123–130, 2005.

[24] M. K. Rehman and H. S. Zurob, “A Novel Approach to Model Static Recrystallization of Austenite During Hot Rolling of Nb Microalloyed Steel. Part I: Precipitate-Free Case,” *Metall. Mater. Trans. A*, vol. 44, no. 4, pp. 1862–1871, Nov. 2012.

[25] Z. Aretxabaleta, B. Pereda, and B. López, “Analysis of the Effect of Al on the Static Softening Kinetics of C-Mn Steels Using a Physically Based Model,” *Metall. Mater. Trans. A*, vol. 45, no. 2, pp. 934–947, Oct. 2013.

[26] J. W. Cahn, “The impurity-drag effect in grain boundary motion,” *Acta Mater.*, vol. 10, pp. 789–798, 1962.

[27] O. Kwon and A. J. Deardo, “Interations between recrystalization and precipitation in hot-deformed microalloyed steels,” *Acta Metall.*, vol. 39, no. 4, pp. 529–538, 1991.

[28] C. Roucoules, S. Yue, and J. J. Jonas, “Effect of Alloying Elements on Metadynamic Recrystallization in HSLA Steels,” *Metall. Mater. Trans. A*, vol. 26A, pp. 181–190, 1995.

[29] H. L. Andrade, M. G. Akben, and J. J. Jonas, “Effect of Molybdenum , Niobium , and Vanadium on Static Recovery and Recrystallization and on Solute Strengthening in Microalloyed Steels,” *Metall. Trans. A*, vol. 14A, no. October, pp. 1967–1977, 1983.

[30] C. Yue, L. Zhang, S. Liao, and H. Gao, “Mathematical models for predicting the austenite grain size in hot working of GCr15 steel,” *Comput. Mater. Sci.*, vol. 45, no. 2, pp. 462–466, Apr. 2009.

[31] S. Cho, K. Kang, and J. J. Jonas, “Effect of manganese on recrystallisation kinetics of niobium microalloyed steel,” *Mater. Sci. Technol.*, vol. 18, pp. 389–396, 2002.

[32] S. F. Medina and J. E. Mancilla, “Static Recrystallization Modelling in Hot Deformed Steels Containing Several Alloying Elements,” *ISIJ Int.*, vol. 36, no. 8, pp. 1070–1076, 1996.

[33] Z. Zhang, Y. Liu, X. Liang, and Y. She, “The effect of Nb on recrystallization behavior of a Nb micro-alloyed steel,” *Mater. Sci. Eng. A*, vol. 474, no. 1–2, pp. 254–260, Feb. 2008.

[34] L. Cheng, H. Chang, B. Tang, H. Kou, and J. Li, “Deformation and dynamic recrystallization behavior of a high Nb containing TiAl alloy,” *J. Alloys Compd.*, vol. 552, pp. 363–369, Mar. 2013.

[35] T. Furuhara, B. Poorganji, H. Abe, and T. Maki, “Dynamic Recovery and Recrystallization in Titanium Alloys by Hot Deformation,” *JOM*, vol. 1, no. January, pp. 4–7, 2007.

[36] H. Y. Kim and S. H. Hong, “High Temperature Deformation Behavior and Microstructural Evolution of Ti-47Al-2Cr-4Nb Intermetallic Alloys,” *Scr. Mater.*, vol. 38, no. 10, pp. 1517–1523, Apr. 1998.

[37] H. Peng, Y. Chen, and F. Liu, “Effects of Alloying on Nanoscale Grain Growth in Substitutional Binary Alloy System : Thermodynamics and Kinetics,” *Metall. Mater. Trans. A*, vol. 46, no. 11, pp. 5431–5443, 2015.

[38] H. Chen, C. Cao, L. Guo, and H. Lin, “Hot deformation mechanism and microstructure evolution of TC11 titanium alloy in β field,” *Trans. Nonferrous Met. Soc. China*, vol. 18, pp. 1021–1027, 2008.

[39] F. Ma, W. Lu, J. Qin, and D. Zhang, “Microstructure evolution of near-α titanium alloys during thermomechanical processing,” *Mater. Sci. Eng. A*, vol. 416, no. 1–2, pp. 59–65, Jan. 2006.

[40] M. Hayashi, H. Yoshimura, M. Ishii, and H. Harada, “Recrystallization behavior of comercially pure titanium during hot rolling.” Nippon Steel Techinal Report, 1994.

[41] R. J. Contieri, M. Zanotello, and R. Caram, “Recrystallization and grain growth in highly cold worked CP-Titanium,” *Mater. Sci. Eng. A*, vol. 527, no. 16–17, pp. 3994–4000, Jun. 2010.

[42] Y. B. Chun and S. K. Hwang, “Static recrystallization of warm-rolled pure Ti influenced by microstructural inhomogeneity,” *Acta Mater.*, vol. 56, no. 3, pp. 369–379, Feb. 2008.

[43] Y. B. Chun, S. L. Semiatin, and S. K. Hwang, “Monte Carlo modeling of microstructure evolution during the static recrystallization of cold-rolled, commercial-purity titanium,” *Acta Mater.*, vol. 54, no. 14, pp. 3673–3689, Aug. 2006.

[44] J. W. Won, T. Lee, S. Hong, Y. Lee, J. H. Lee, and C. S. Lee, “Role of Deformation Twins in Static Recrystallization Kinetics of High-Purity Alpha Titanium,” *Met. Mater. Int.*, vol. 22, no. 6, pp. 1041–1048, 2016.

[45] Y. . Wang and J. . Huang, “Texture analysis in hexagonal materials,” *Mater. Chem. Phys.*, vol. 81, no. 1, pp. 11–26, Jul. 2003.

[46] D. Tromans, “Elastic Anisotropy of HCP Metal Crystals and Polycrystals,” *IJRRAS*, vol. 6, no. March, pp. 462–483, 2011.

[47] M. Bache and W. Evans, “Impact of texture on mechanical properties in an advanced titanium alloy,” *Mater. Sci. Eng. A*, vol. 319–321, pp. 409–414, Dec. 2001.

[48] F. Coghe, W. Tirry, L. Rabet, D. Schryvers, and P. Van Houtte, “Importance of twinning in static and dynamic compression of a Ti–6Al–4V titanium alloy with an equiaxed microstructure,” *Mater. Sci. Eng. A*, vol. 537, pp. 1–10, Mar. 2012.

[49] J. L. W. Warwick, N. G. Jones, K. M. Rahman, and D. Dye, “Lattice strain evolution during tensile and compressive loading of CP Ti,” *Acta Mater.*, vol. 60, no. 19, pp. 6720–6731, Nov. 2012.

[50] A. Stark, F. P. Schimansky, and H. Clemens, “Texture Formation during Hot-Deformation of High-Nb Containing γ-TiAl Based Alloys,” *Solid State Phenom.*, vol. 160, pp. 301–306, Feb. 2010.

[51] H. Kou, Y. Chen, B. Tang, Y. Cui, F. Sun, J. Li, and X. Xue, “An experimental study on the mechanism of texture evolution during hot-rolling process in a β titanium alloy,” *J. Alloys Compd.*, vol. 603, pp. 23–27, Aug. 2014.

[52] P. Lin, A. Feng, S. Yuan, G. Li, and J. Shen, “Microstructure and texture evolution of a near-α titanium alloy during hot deformation,” *Mater. Sci. Eng. A*, vol. 563, pp. 16–20, Feb. 2013.

[53] J. E. Burke and D. Turnbull, “Recrystallization and grain growth,” *Prog. Met. Phys.*, vol. 3, pp. 220–292, 1952.

[54] J. R. Trelewicz and C. A. Schuh, “Grain boundary segregation and thermodynamically stable binary nanocrystalline alloys,” *Phys. Rev. B*, vol. 79, 2009.

[55] F. J. Gil, J. A. Picas, J. M. Manero, A. Forn, and J. A. Planell, “Effect of the addition of palladium on grain growth kinetics of pure titanium,” *J. Alloys Compd.*, vol. 260, no. 1–2, pp. 147–152, Sep. 1997.

[56] B. Cherukuri, R. Srinivasan, S. Tamirisakandala, and D. B. Miracle, “The influence of trace boron addition on grain growth kinetics of the beta phase in the beta titanium alloy Ti–15Mo–2.6Nb–3Al–0.2Si,” *Scr. Mater.*, vol. 60, no. 7, pp. 496–499, 2009.

[57] F. J. Gil and J. A. Planell, “Behaviour of normal grain growth kinetics in single phase titanium and titanium alloys,” *Mater. Sci. Eng. A*, vol. 283, no. 1–2, pp. 17–24, May 2000.

[58] S. L. Semiatin, J. Soper, and I. Sukonnik, “Grain growth in a conventional titanium alloy during rapid, continuous heat treatment,” *Scr. Mater.*, vol. 30, no. 7, pp. 951–955, 1994.

[59] P. Xiaona, “Isothermal Beta Grain Growth Kinetics of TC4-DT Titanium Alloy under Two Different Prior Processing Conditions : Deformed vs . Undeformed,” *Rare Met. Mater. Eng.*, vol. 43, no. 8, pp. 1855–1861, 2014.

[60] D.-G. Lee, C. Li, Y. Lee, X. Mi, and W. Ye, “Effect of temperature on grain growth kinetics of high strength Ti–2Al–9.2Mo–2Fe alloy,” *Thermochim. Acta*, vol. 586, pp. 66–71, Jun. 2014.

[61] J. Fan, J. Li, H. Kou, K. Hua, B. Tang, and Y. Zhang, “Influence of solution treatment on microstructure and mechanical properties of a near b titanium alloy Ti-7333,” *Mater. Des.*, vol. 83, pp. 499–507, 2015.

[62] J.-W. Lu, Y.-Q. Zhao, P. Ge, and H.-Z. Niu, “Microstructure and beta grain growth behavior of Ti–Mo alloys solution treated,” *Mater. Charact.*, vol. 84, no. 96, pp. 105–111, Oct. 2013.

[63] L. Llanos, B. Pereda, B. López, and J. M. Rodriguez-ibabe, “Modelling of Static Recrystallization Behavior of High Manganese Austenitic Steels with Different Alloying Contents,” *ISIJ Int.*, vol. 56, no. 6, pp. 1038–1047, 2016.

[64] H. Wu, L. Du, Z. Ai, and X. Liu, “Static Recrystallization and Precipitation Behavior of a Weathering Steel Microalloyed with Vanadium,” *J. Mater. Sci. Technol.*, vol. 29, no. 12, pp. 1197–1203, 2013.

[65] M. Suehiro, “An Analysis of the Solute Drag Effect of Nb on Recrystallization of Ultra Low Carbon Steel,” *ISIJ Int.*, vol. 38, no. 6, pp. 547–552, 1998.

[66] L. Bäcke, “Modeling the Effect of Solute Drag on Recovery and Recrystallization during Hot Deformation of Nb Microalloyed Steels,” *ISIJ Int.*, vol. 50, no. 2, pp. 239–247, 2010.

[67] K. Khlopkov, G. Paul, and T. Pretorius, “Characterization and Modeling of Softening Kinetics during Hot Deformation in Modern Steels,” *Mater. Sci. Forum*, vol. 762, pp. 134–139, 2013.

[68] A. Karmakar, S. Kundu, S. Roy, S. Neogy, D. Srivastava, and D. Chakrabarti, “Effect of microalloying elements on austenite grain growth in Nb – Ti and Nb – V steels,” *Mater. Sci. Technol.*, vol. 30, no. 6, pp. 653–664, 2014.

[69] M. Schinhammer, C. M. Pecnik, F. Rechberger, A. C. Ha, F. Lo, and P. J. Uggowitzer, “Recrystallization behavior , microstructure evolution and mechanical properties of biodegradable Fe–Mn–C(–Pd) TWIP alloys,” *Acta Mater.*, vol. 60, pp. 2746–2756, 2012.

[70] A. S. Hamada, L. P. Karjalainen, and M. C. Somani, “The influence of aluminum on hot deformation behavior and tensile properties of high-Mn TWIP steels,” *Mater. Sci. Eng. A*, vol. 467, pp. 114–124, 2007.

[71] M. Hillert and B. O. Sundman, “A treatment of the solute drag on moving grain boundaries and phase interfaces in binary alloys,” *Acta Metall.*, vol. 24, pp. 731–743, 1976.

[72] C. Qiu, H. S. Zurob, D. Panahi, Y. J. M. Brechet, and G. R. Purdy, “Quantifying the Solute Drag Effect on Ferrite Growth in Fe-C-X Alloys Using Controlled Decarburization Experiments,” *Metall. Mater. Trans. A*, vol. 44A, pp. 3472–3483, 2013.

[73] C. Qiu, H. S. Zurob, and C. R. Hutchinson, “The coupled solute drag effect during ferrite growth in Fe–C–Mn–Si alloys using controlled decarburization,” *Acta Mater.*, vol. 100, pp. 333–343, 2015.

[74] H. Kotan, K. A. Darling, and M. Saber, “Thermal stability and mechanical properties of nanocrystalline Fe – Ni – Zr alloys prepared by mechanical alloying,” *J. Mater. Sci.*, vol. 48, pp. 8402–8411, 2013.

[75] Y. Yogo, K. Tanaka, H. Ikehata, N. Iwata, K. Nakanishi, T. Ishikawa, Y. Yogo, K. Tanaka, H. Ikehata, N. Iwata, K. Nakanishi, and T. Ishikawa, “Calculation for grain growth rate of carbon steels by solute drag model considering segregation effect of each substitutional element,” *Mater. Sci. Technol.*, vol. 27, no. 10, pp. 1593–1598, 2011.

[76] C. J. Silva, A. Kula, R. K. Mishra, and M. Niewczas, “Grain growth kinetics and annealed texture characteristics of Mg-Sc binary alloys,” *J. Alloys Compd.*, vol. 687, pp. 548–561, 2016.

Chapter 2. Materials Processing and Characterization

2.1 Materials Processing

The materials studied in this work are binary alpha titanium aluminum alloys that serve as model alloys for the dominant alpha phase of many commercial titanium alloys. Three different alloys are studied with varying concentrations of aluminum, 0wt%, 4wt%, and 7wt%, and trace amounts of iron and oxygen as listed in Table 1. At room temperature, these alloys are solely comprised of the stable HCP alpha phase. This phase remains stable until the temperature is raised above the beta transus temperature of the alloy, at which point the alpha phase will transform into the metastable BCC beta phase [1]. All of the experiments conducted in this research will be within the alpha regime for the three alloys as marked in Figure 14.

Table 1. Chemical compositions and beta transus temperatures of alloys studied

Alloy	**Chemical Composition**			**Beta transus temperature**
	Al (wt%)	Fe (wt%)	O (wt%)	
Ti-0wt%Al	0.005	0.008	0.086	1163K (890°C)
Ti-4wt%Al	3.85	0.013	0.096	1263K (990°C)
Ti-7wt%Al	6.92	0.016	0.087	1322K (1049°C)

All materials used in this research were provided by Timet Metals Corporation. The ingots of the alloys were first produced via vacuum arc remelting (VAR). This process includes a secondary controlled melting step where the ingot is continuously melted into a cooled crucible where it is cooled back to room temperature. The melting and cooling rate are closely controlled in order to produce a very homogenous material. The resulting ingots were then heated in a furnace to 93°C above the beta transus temperatures and held for 3 hours to ensure a uniform temperature. The heated ingots were cogged from a 7.5” round cross section

to a 4” square cross section using a large mechanical press. This was done using multiple compression steps by compressing by an incremental distance in one direction, then rotating the ingot by 90° and compressing by the same distance, as depicted in Figure 15. This was repeated until the desired cross section was achieved. The ingots were then air cooled and a small thickness of the Ti-7wt%Al ingot surface was cut off in order to remove surface cracking.

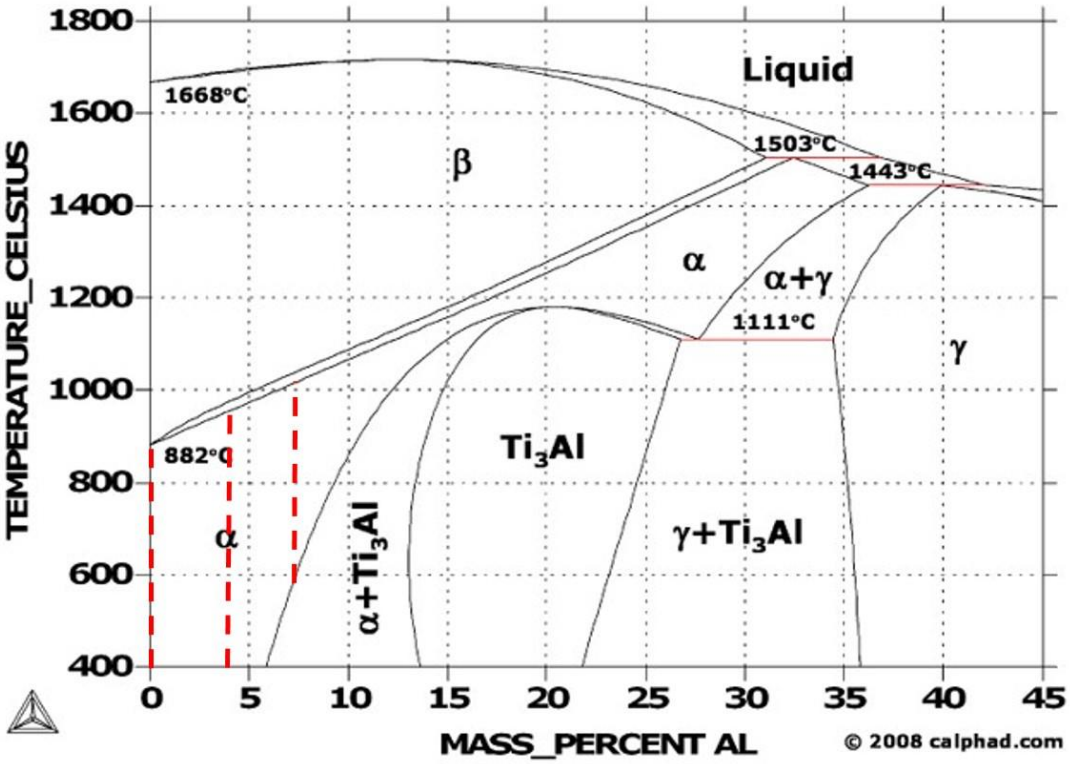

Figure 14. Titanium-Aluminum phase diagram with the alpha regime temperature ranges indicated for the three alloys being studied

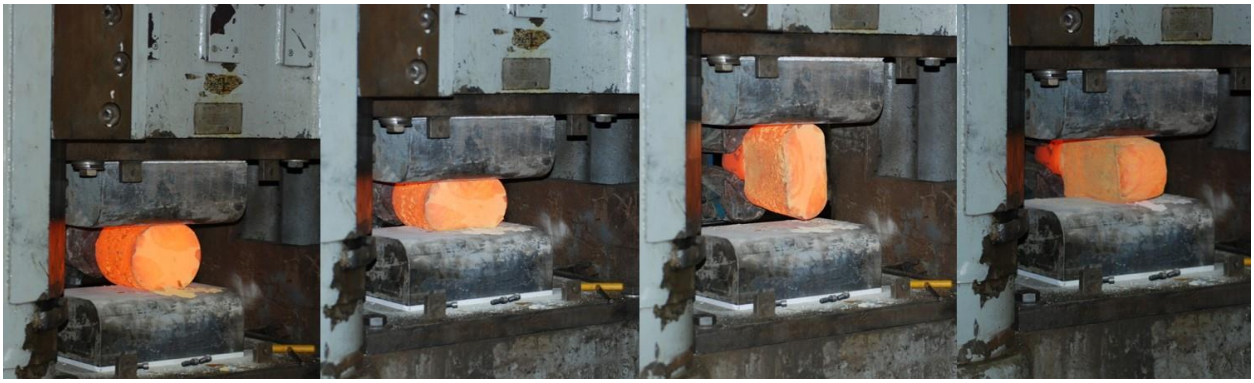

Figure 15. Beta forging process

2.2 Microstructure

The as-beta-forged microstructure is shown in Figure 16 and consists of a deformed lamellar microstructure. As the alloys are heating above their respective beta transus temperatures, they transform from the alpha phase to the beta phase. While they are soaked at a high temperature, the beta phase is stable and large beta grains are able to form. During air cooling, the materials transform back into alpha by growing alpha lamellae into the prior beta grains [1]. Some of these alpha colonies, or groups of alpha lamellae with the same orientation, look deformed or distorted in Figure 16, which can be explained by the simultaneous cooling that occurs during deformation due to heat lost via the air and the anvils. The orientation of the alpha phase that forms is related to the prior beta grain that it is replacing based on the Burger's relationship between the BCC and HCP crystal structures. Therefore, due to the difference in orientation between prior beta grains, there is some variation in the texture of the as forged material. Figure 17 includes EBSD scans of the as forged texture for both Ti-4wt%Al and Ti-7wt%Al that include prior beta grain boundaries. In the image of the Ti-7wt%Al, it is clear that the top region has a mostly basal texture while the bottom region has a mostly prismatic texture. This indicates that the dividing line between the two regions is a prior beta grain boundary.

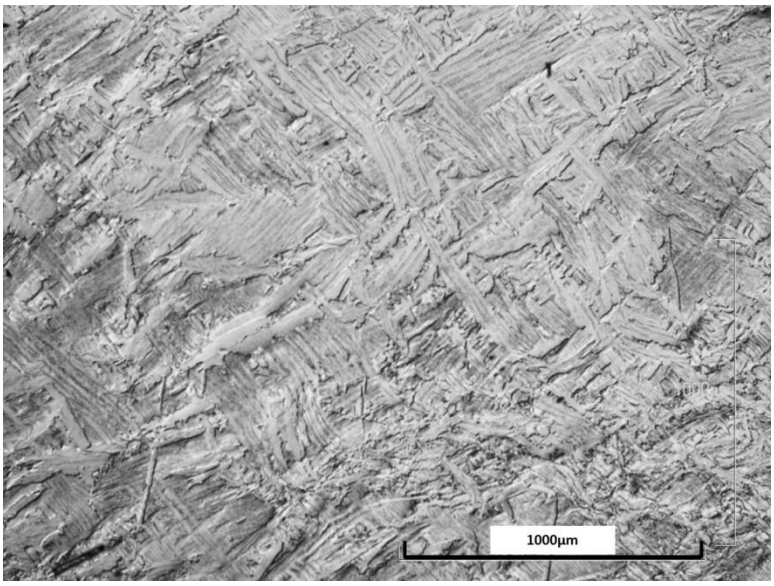

Figure 16. Initial microstructure of as beta forged Ti-4wt%Al

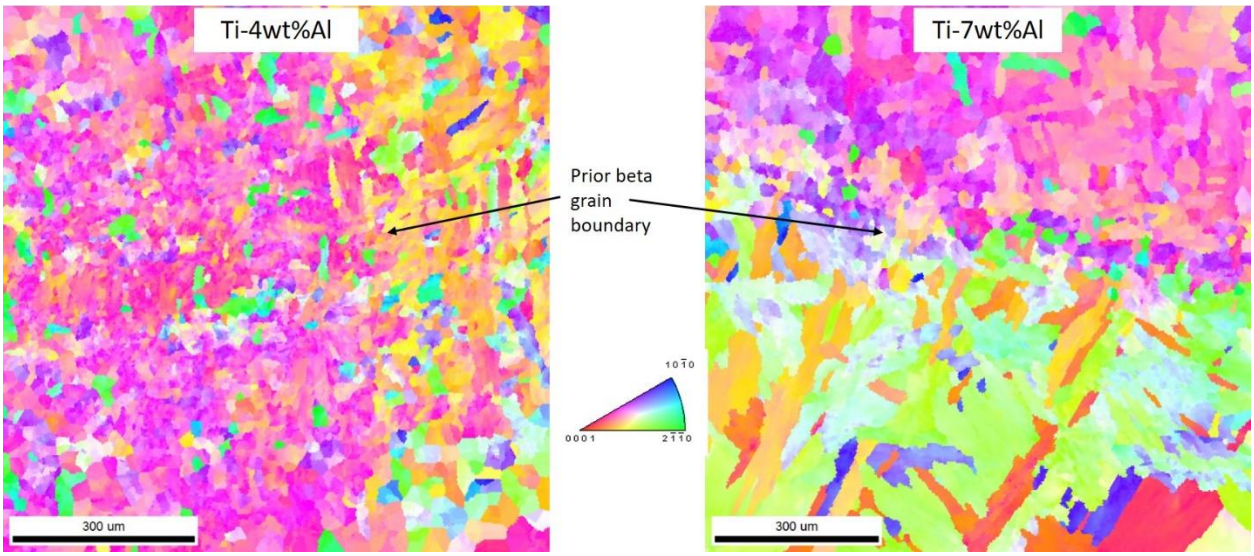

Figure 17. Examples of the as forged texture in Ti-4wt%Al and Ti-7wt%Al that include prior beta grains

The distribution of stored energy in the beta forged material was investigated by annealing the as received samples for various times and observing the distribution of recrystallization. Figure 18 shows both inverse pole figure (IPF) maps collected via EBSD and corresponding grain orientation spread (GOS) maps for Ti-4wt%Al samples that have been annealed at 900°C for one and two hours. In the GOS maps, grains highlighted in light blue have a very low GOS and therefore are considered to be recrystallized. After one hour, a few

small regions have begun to recrystallize and many of the recrystallized grains have experienced grain growth with some of the grains reaching sizes of approximately 100µm. After two hours, there is a clear string of recrystallized grains with very large grain sizes indicating that these regions nucleated early and grain growth has occurred relatively quickly. However, this recrystallized region is surrounded by regions where nucleation has not occurred and that are still deformed as indicated by the orange coloring in the GOS maps that represent high GOS values. This variation in recrystallization rates indicates a significant variation in the distribution of stored energy. The regions containing bands of recrystallized grains were initially bands of high stored energy allowing nucleation and growth to occur rapidly at this annealing temperature. The regions where nucleation is not occurring have lower stored energy that is not sufficient enough for nucleation to occur at this temperature. For this reason, all samples are first compressed to a 20% height reduction at room temperature prior to annealing for recrystallization and grain growth studies in order to create a more uniform distribution of stored energy and to ensure sufficient stored energy is present to initiate recrystallization at various annealing temperatures.

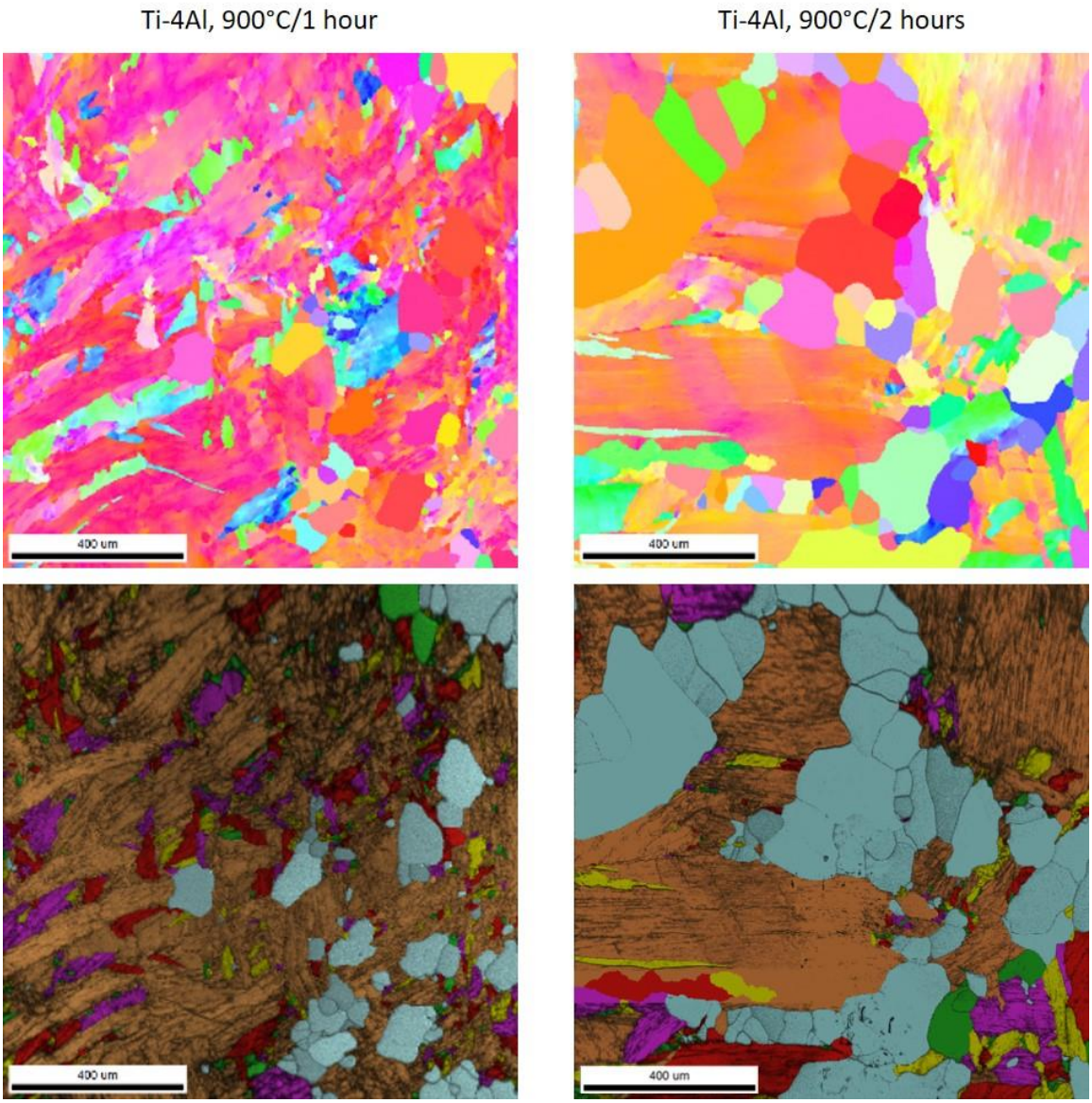

Figure 18. Inverse pole figure (IPF) maps (top row) and grain orientation spread (GOS) maps (bottom row) of Ti-4wt%Al samples annealed at 900°C for 1 hour (left column) and 2 hours (right column). Grains highlighted in blue in GOS maps indicate recrystallized grains.

2.3 Mechanical properties

The basic mechanical properties of the as received materials were determined via room temperature uniaxial tensile tests. Tests were performed using an MTS load frame at a strain rate of 0.01mm/s on circular dog bone shaped samples with a gage section diameter of 5mm and length of 13.45mm. An extensometer was attached to the gage section during testing to

accurately measure the strain and three samples of each alloy were tested. The resulting stress-strain curves are plotted in Figure 19 and the average values for yield strength, ultimate tensile strength and Young's modulus are listed in Table 2. These results show an increase in strength with increasing aluminum concentration, which is expected due to solute strengthening. This is known to occur in titanium with the addition of aluminum due to the fairly large atomic size difference. The yield stress for the Ti-0wt%Al is significantly higher than the value of 170MPa that is reported for CP titanium with low oxygen content (Grade 1) [1]. This is explained by the previous deformation the material underwent during forging that causes work hardening. Also, cooling the material from above the beta transus temperature creates a lamellar microstructure instead of an equiaxed microstructure that would result from solution heat treating the alpha regime. The lamellar microstructure has an increased number of grain boundaries that decreases the mean free distance for dislocation motion and therefore strengthens the material and increases the yield strength.

The work hardening behavior of these alloys was determined by analyzing the stress-strain response during plastic deformation. The measured stress-strain curves were first converted into true stress and true strain (Figure 20a) using the following relationships:

$$\varepsilon_T = \ln(1 + \varepsilon_e) \quad (1)$$

$$\sigma_T = \sigma_e(1 + \varepsilon_e) \quad (2)$$

where ε_T and ε_e are true and engineering strain respectively and σ_T and σ_e are true and engineering stress respectively. True stress and true strain are then plotted on a logarithmic scale (Figure 20b) and the plastic regime was isolated (Figure 20c). The slope of this curve is equal to the work hardening exponent, n, based on the work hardening power law:

$$\sigma = K\varepsilon^n \quad (3)$$

An n value of 0 corresponds to a fully plastic material while an n value of 1 corresponds to a fully elastic material. The calculated n values are listed in Table 3 and are seen to decrease with increasing aluminum concentration meaning the addition of aluminum to titanium decreases

the work hardening rate. This trend can be explained by considering how aluminum solute atoms influence the deformation modes in titanium.

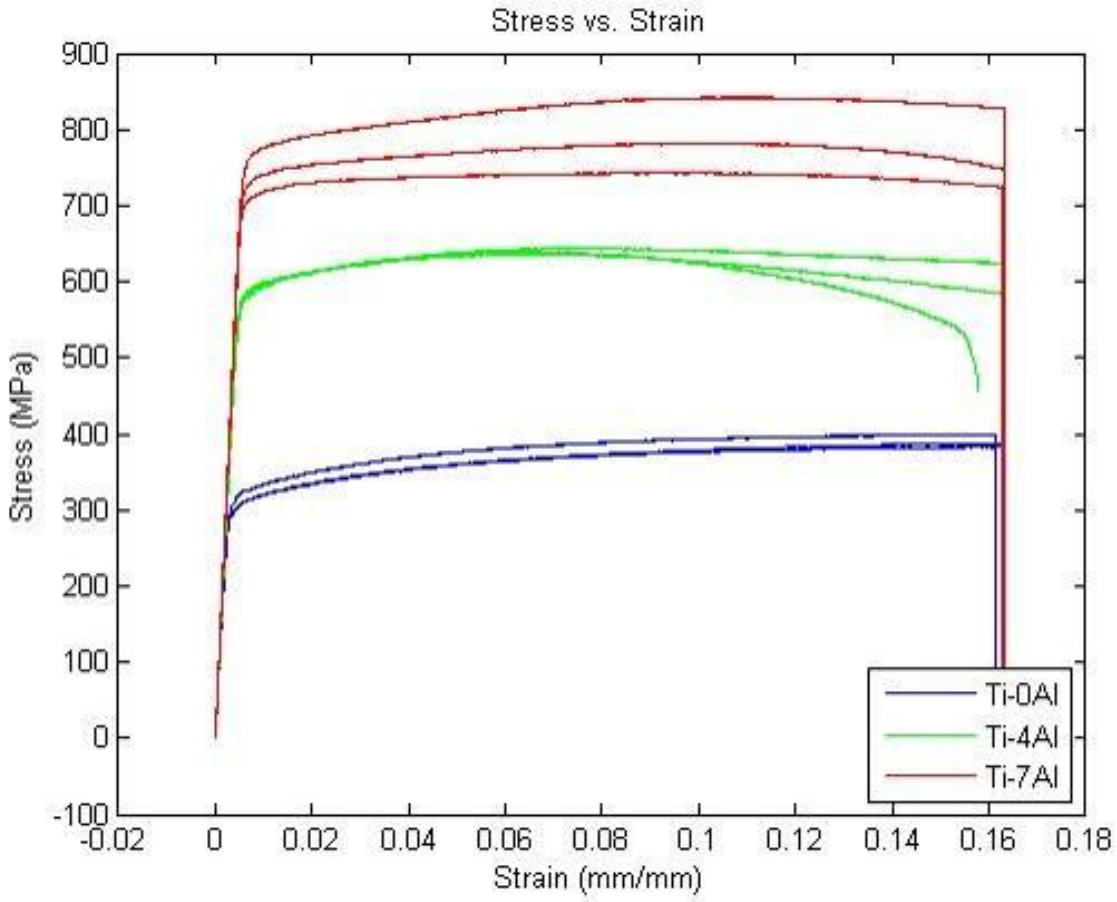

Figure 19. Stress-strain curves for all three alloys measured via uniaxial tensile tests

Table 2. Average values for yield stress, ultimate tensile strength and Young's modulus calculated from three stress-strain curves per alloy

Material	**σ_{YS} (Yield Stress, MPa)**	**σ_{UTS} (Ultimate Tensile Strength, MPa)**	**E (Young's Modulus, GPa)**
Ti-0Al	311	391	107
Ti-4Al	586	640	126
Ti-7Al	736	789	136

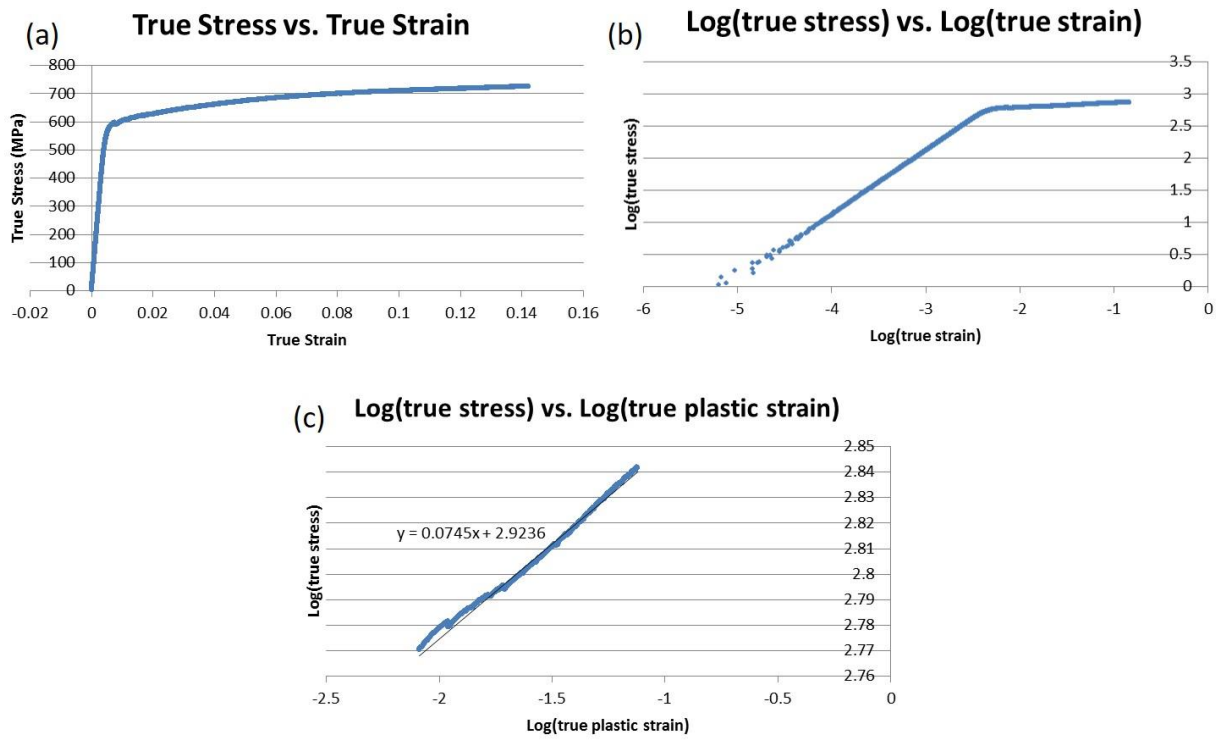

Figure 20. Example of work hardening analysis from experimentally measured tensile curve

Table 3. Calculated work hardening exponents and strength coefficients

Alloy	Average n	Average K (MPa)
Ti-0Al	0.12	550
Ti-4Al	0.071	832
Ti-7Al	0.066	1000

The most common slip modes in titanium are the $\{10\bar{1}0\}$, $\{10\bar{1}1\}$, and {0001} planes with the $\langle 11\bar{2}0\rangle$ slip direction, which makes up four independent slip systems. However, a total of five independent slip systems are required for plastic deformation so both twinning and dislocation slip occur in pure titanium during plastic deformation [1]–[4]. The addition of aluminum solute atoms suppresses twinning in titanium [5], causing $\langle c+a\rangle$ pyramidal slip to be required for plastic deformation. This causes plastic deformation to be more difficult because of the high critical resolved shear stress for pyramidal slip [1]. Twin boundaries block

dislocations hindering their motion and decreasing their mean free path, so high dislocation densities occur around twins, especially at their tips [2]. Therefore, increased twinning will increase the work hardening rate. Suppression of twinning by adding aluminum atoms will then lower the work hardening rate and the total dislocation density for a given strain.

In order to observe twinning in the alloys studied in this research, samples were first compressed and room temperature and annealed so that fully recrystallized and equiaxed microstructures were achieved with similar grain sizes for all three alloys. The samples were then compressed further to a 7% height reduction, etched and imaged optically as seen in Figure 21. As expected, there is a significant higher density of twins in the Ti-0wt%Al than in the 4 or 7wt%Al. Twinning is mostly, though not completely, suppressed in the Ti-4wt%Al and Ti-7wt%Al and there is not a significant different in twin density between the two. These observations correspond well with the work hardening results given that the n values for the 4 and 7wt%Al are similar but they are about half the value of n for Ti-0wt%Al.

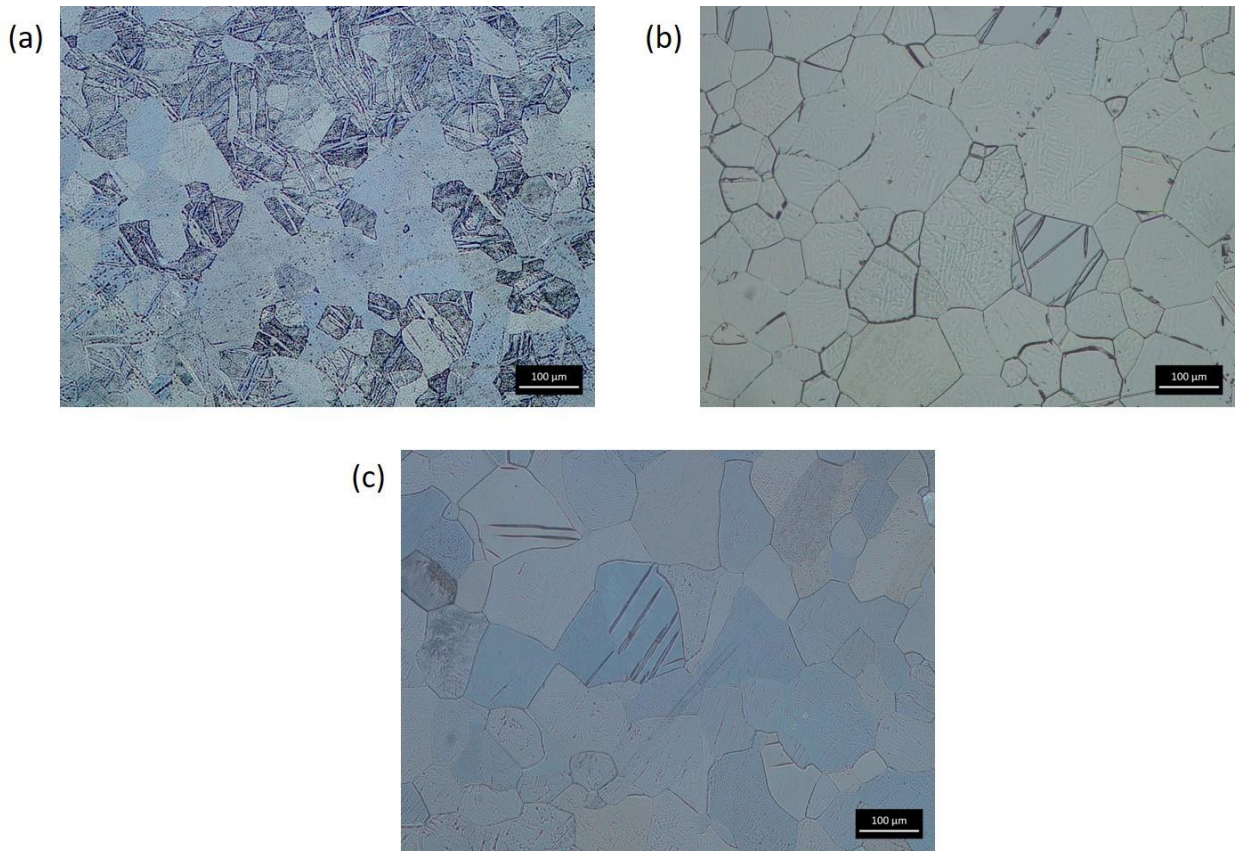

Figure 21. Twinning observed in (a) Ti-0wt%Al, (b) Ti-4wt%Al, and (c) Ti-7wt%Al after being fully recrystallized and plastically deformed via room temperature compression

2.4 References

[1] G. Lutjering and J. C. Williams, *Titanium*, Second. New York: Springer, 2007.

[2] D. Kang, K. Lee, E. Kwon, and T. Tsuchiyama, “Variation of work hardening rate by oxygen contents in pure titanium alloy,” *Mater. Sci. Eng. A*, vol. 632, pp. 120–126, 2015.

[3] T. Hama, H. Nagao, A. Kobuki, H. Fujimoto, and H. Takuda, “Work-hardening and twinning behaviors in a commercially pure titanium sheet under various loading paths,” *Mater. Sci. Eng. A*, vol. 620, pp. 390–398, 2015.

[4] S. Nemat-Nasser, W. G. Guo, and J. Y. Cheng, “Mechanical Properties and Deformation Mechanisms of a Commercially Pure Titanium,” *Acta Mater.*, vol. 47, no. 13, pp. 3705–3720, 1999.

[5] A. Fitzner, D. G. L. Prakash, J. Quinta, M. Thomas, S. Zhang, J. Kelleher, P. Manuel, M. Preuss, I. Facility, H. Oxford, and D. Ox, “The effect of aluminium on twinning in binary alpha-titanium,” *Acta Mater.*, vol. 103, pp. 341–351, 2016.

Chapter 3. The influence of aluminum content and annealing temperature on static recrystallization kinetics

3.1 Introduction

Titanium alloys are used for a range of naval and aerospace applications due to their desirable properties such as high strength to weight ratio, corrosion resistance, and thermal stability. One common processing route chosen for titanium alloys is hot forging, during which the material undergoes a variety of deformation and annealing steps. Deformation leads to a build-up of dislocations, increasing the stored energy in the material, driving the nucleation and growth of strain free grains upon subsequent annealing. This process of recrystallization and grain growth has a significant impact on the properties of the material. It is therefore important to understand the extent of recrystallization that occurs during processing and to be able to predict the effect of that microstructural evolution on the resulting material properties.

This work is part of a larger Integrated Computational Materials Engineering (ICME) effort whose goal is to combine both computational and experimental efforts to develop computationally efficient models that predict materials microstructure and properties based on processing history. The experimental recrystallization results detailed in this chapter are used to guide the development of and provide validation of phase field models for recrystallization and grain growth that predict microstructural evolution [1]. Ultimately the resulting microstructural distribution maps can be used to develop reduced order descriptors that provide computationally compact descriptions of predicted microstructures based on processing history [2].

The alloys chosen in this study are pure hcp α-phase, binary Ti-Al alloys with varying Al concentrations. These alloys serve as model alloys for the α phase that is the predominant phase in commercial α and near α titanium alloys. Studying alloys with varying solute concentration allows for the investigation of the effect of aluminum on the recrystallization kinetics. While there has been a range of studies on the effects of alloying elements on static recrystallization (SRX) in steels [3]–[6], few studies have been conducted on this topic for titanium alloys. These studies have investigated dynamic recrystallization (DRX) kinetics of titanium alloys during hot deformation [7]–[11] but little research has been conducted on SRX kinetics that results from cold deformation and subsequent annealing.

The goal of this chapter is to investigate the effects of solute concentration and thermomechanical processing variables such as annealing temperature on the SRX kinetics after cold deformation. These results are then captured using an analytical model. In addition, the effects of both deformation and recrystallization on texture have been studied.

3.2 Experimental

3.2.1 Materials

For this investigation, three binary α titanium alloys, Ti-0Al, Ti-4Al and Ti-7Al, were produced in 7.5" round ingots via vacuum arc remelting (VAR). These ingots were then β cogged at 366K (93°C) above the β transus temperature, reduceding the ingots to a 4" square cross section (ε≈1), followed by air cooling. Ingot production and cogging were conducted by Timet Corporation. A summary of the alloy chemical compositions and β transus temperatures is listed in Table 4.

Table 4. Chemical compositions and beta transus temperatures of alloys studied

Alloy	**Chemical Composition**			**Beta transus temperature**
	Al (wt%)	**Fe (wt%)**	**O (wt%)**	
Ti-0wt%Al	0.005	0.008	0.086	1163K (890°C)
Ti-4wt%Al	3.85	0.013	0.096	1263K (990°C)
Ti-7wt%Al	6.92	0.016	0.087	1322K (1049°C)

Figure 22 shows the initial microstructure of the as-received beta cogged material. A lamellar microstructure resulted from cooling the material from above the beta transus temperature.

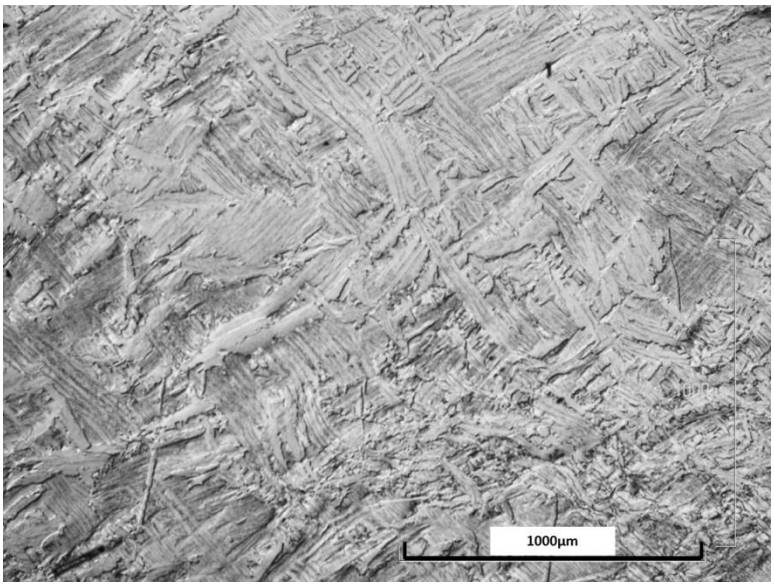

Figure 22. As-received beta cogged microstructure of Ti-4Al

3.2.2 Deformation and Annealing

Cylindrical samples 6mm in diameter and 9mm in height were machined via electrical discharge machining (EDM) from the beta cogged ingots. The samples were machined from the ingot so that the axis of the cylinder was parallel to the longitudinal direction of the ingot. The samples were compressed at room temperature using an Instron load frame equipped with a 100kN load cell. To reduce the friction between the samples and the compression dies, the ends of the cylindrical samples were hand ground using 240, 400, and 800 grit SiC paper and a commercial lubricant was applied between the two surfaces. Compression tests were performed at a strain rate of 0.03 mm/min ($5x10^{-5}$ s^{-1}) and resulted in a final deformed sample height of 7.6mm. A simulation of the compression of the cylindrical samples was performed using Abaqus finite element analysis software in order to determine the strain distribution within the compression samples of each alloy. A 1/8 axi-symmetric model was used for this model with a four-node bilinear axisymmetric quadrilateral mesh. The upper compression platen was modeled as a rigid body while the sample was modeled as a deformable body and

was assigned the properties of a given alloy. The input elastic modulus and tabular flow stress values for each alloy were determined through experimental tensile tests and the Poisson's ratio was assumed to be 0.33. The interaction between the sample and the platen are modeled using the constant friction model. The central axis is fixed in the x and z direction and the compression platen is displaced in the –z direction to model the compression test. As shown in Figure 23, the results indicate that a region of high and nominally uniform strain corresponds to an approximate area of 1.5mm by 1.5mm in the center of the sample would be a suitable area for quantifying recrystallization and grain growth using EBSD analysis as described below. The average true strain in this area after compression is 0.34.

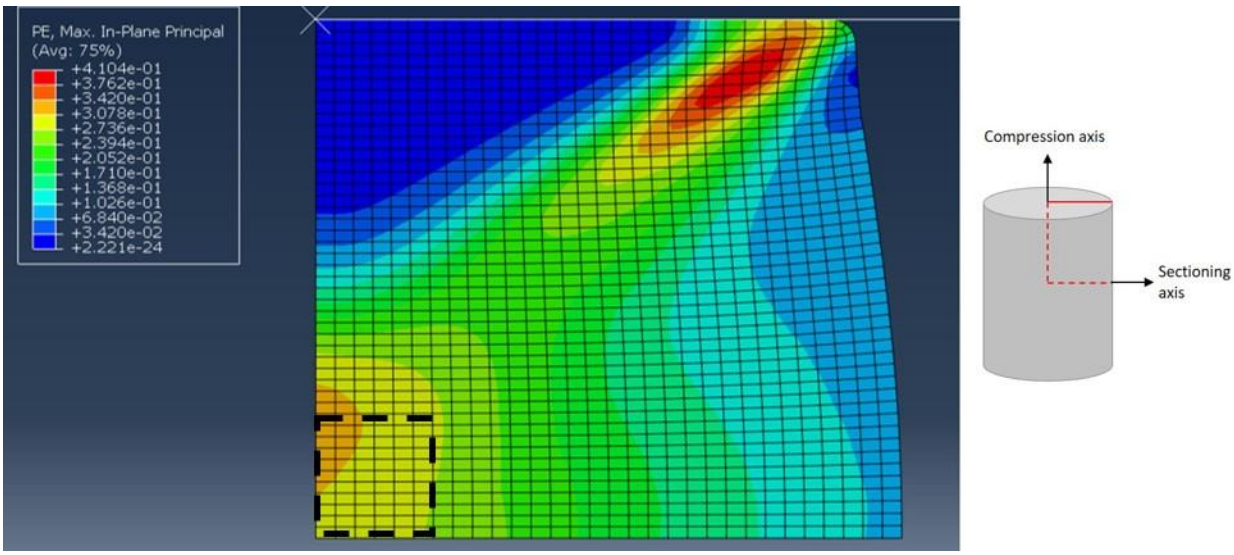

Figure 23. Abaqus simulation of compression test. The 1/8 axi-symmetric model is shown.

Compressed samples of all three alloys were subsequently heat treated at 1073K (800°C) for various times and water quenched in order to observe the effect of alloy composition on static recrystallization. Compressed samples of Ti-0Al were heat treated at 773K (500°C), 873K (600°C) and 1073K (800°C) for various times and water quenched in order to observe the effect of annealing temperature. All heat treatments were performed in a horizontal ceramic tube furnace. A thermocouple was placed in the center of the furnace for temperature calibration and all samples were placed at the end of the thermocouple to ensure temperature consistency from sample to sample.

A timed heat up test was performed in the tube furnace to measure the time required for a sample to reach 800°C. To accomplish this a hole was drilled into a compression sample and a thermocouple inserted into the center of the sample. This test demonstrated that it took approximately 90 seconds for the center of the sample to reach 800°C. While this heat up time is negligible for the long annealing times, it is important to take into account for the very short annealing times. Therefore, for the condition of annealing Ti-0wt%Al at 800°C, a 1mm slice of the compressed samples were sectioned from the center and annealed. These smaller samples were used in order to minimize the heat up time and more accurately capture the recrystallization process.

3.2.3 Electron backscatter diffraction (EBSD)

Electron backscatter diffraction was used to measure the fraction of recrystallization, grain size and to analyze texture. Samples were sectioned perpendicular to the cylindrical axis in the center of the sample so that the normal to the surface examined is perpendicular to the compression direction. The sectioned samples were mounted in epoxy and mechanically polished for metallography. The procedure for polishing consisted of grinding with SiC paper to a grit size of 800 followed by a final polishing step with a mixture of colloidal silica and hydrogen peroxide. EBSD scans were performed on a Tescan Mira 3 scanning electron microscope using a voltage of 25kV and beam intensity of 18, using a EDAX Hikari XP EBSD camera. TSL OIM software was used to analyze these scans. All scans were approximately 1500µm x 1500µm or less, ensuring that the plastic strain in this region was constant to within 10% of the average value. An average step size of 3 ± 0.5µm was used and an average confidence index of 0.5 ± 0.1 was obtained. A grain tolerance angle for grain recognition of 5° was used and scans of a fully recrystallized microstructure consisted of approximately 900 grains on average.

The grain orientation spread (GOS) method was chosen to quantify the amount of recrystallization present in each sample [12], [13]. This method is based on the concept that regions of the material that are deformed will have a large variation in local orientation due to lattice rotations caused by the dislocations that are produced during deformation. In contrast

newly recrystallized grains that are strain free will have a uniform orientation. A GOS value is assigned to each grain and is calculated using the procedure described below. The average grain orientation is computed for each individual grain by averaging the measured orientations for all of the points within the grain. That average orientation is then compared to each point in the grain and a misorientation value is calculated for each individual point within the grain. Those misorientation values are then averaged and the computed average misorientation value is assigned to the grain as the GOS value. A general formula for the GOS value is given by [14]:

$$GOS = \frac{1}{N}\sum_{A=1}^{N}\left\{min\left[cos^{-1}\left(\frac{trace\left[g_{ave}\left(h_i g^A\right)^{-1}\right]-1}{2}\right)\right]\right\} \quad (1)$$

where g_{ave} is the orientation matrix for the average orientation of the grain, h is an element of the symmetry group for the crystal structure, g^A is the orientation matrix for a given data point, and N is the number of data points in a given grain.

For this work, a grain is defined as being recrystallized if it has a GOS value of 1° or less. This cut-off value was determined by analyzing the GOS distributions for multiple samples with varying degrees of recrystallization (Figure 24). Partially recrystallized samples exhibit a bimodal GOS distribution because the recrystallized grains have low GOS values while the deformed regions have high GOS values. Analyzing these distributions showed that the low GOS peak consists of GOS values from 0° to 1° for all samples. The area fraction of the EBSD scan that has a GOS value of 1° or less is thus taken to be the area fraction of recrystallized grains. In the sample shown in Figure 25, the recrystallized grains are highlighted in light blue, which corresponds to the bin of GOS values of 0 to 1°, and the fraction recrystallized was determined to be 61%.

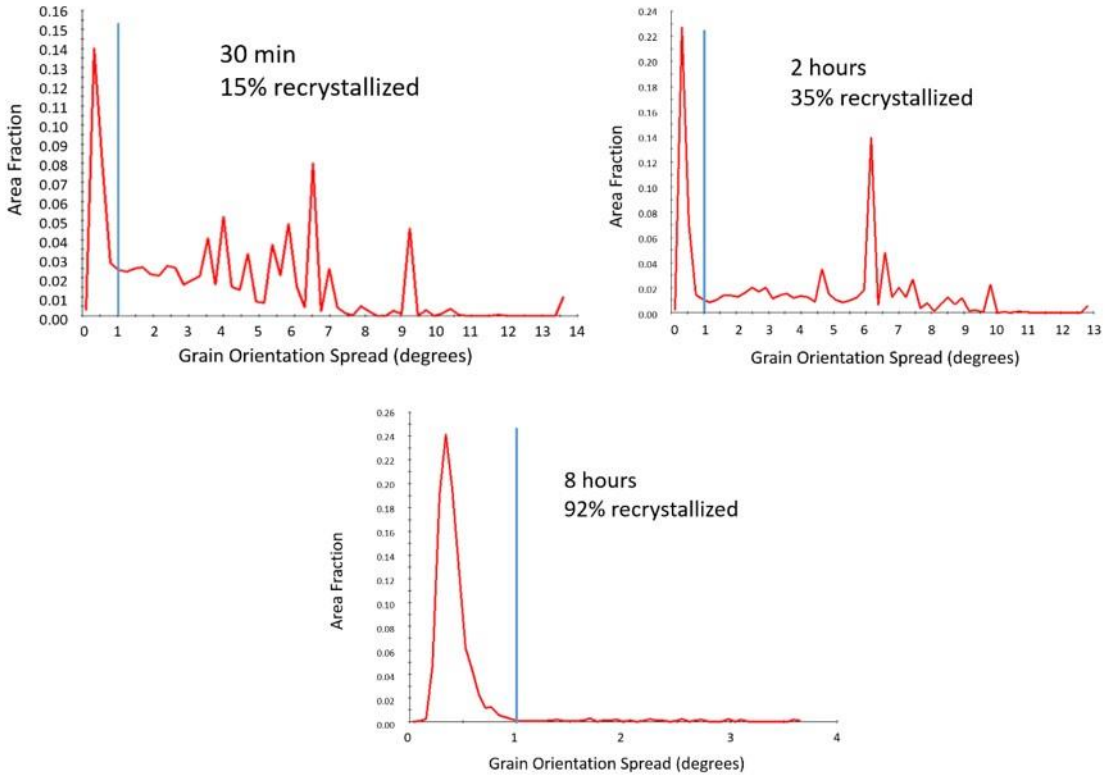

Figure 24. GOS distribution graphs for Ti-4Al samples compressed at room temperature and annealed at 1073K (800°C). Plots are displaying Area Fraction vs. Grain Orientation Spread (degrees) and the vertical lines mark the 1° GOS cutoff value.

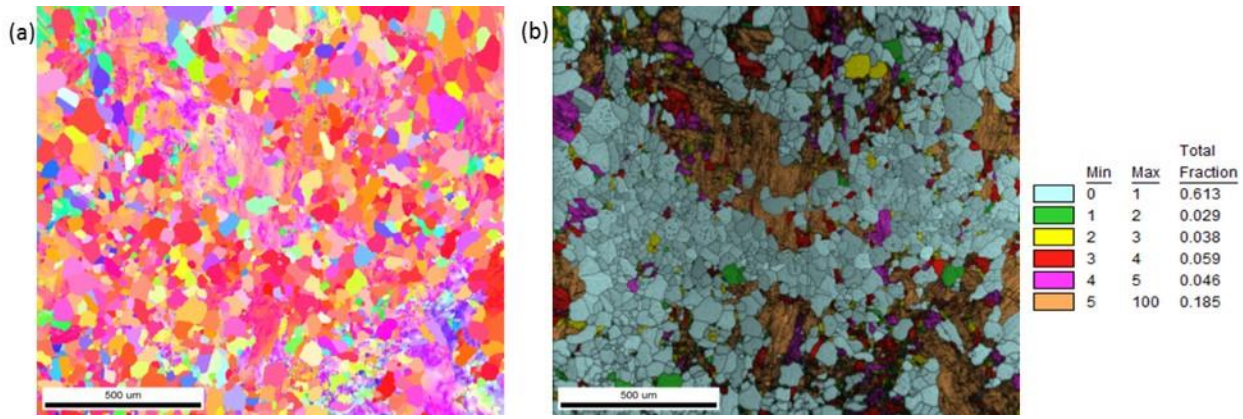

Figure 25. (a) Inverse pole figure (IPF) and (b) Grain orientation spread (GOS) map of Ti-7Al sample compressed at room temperature and annealed at 1073K (800°C) for 18hrs

3.3 Experimental Results and Discussion

3.3.1 Static recrystallization results

Samples of Ti-0wt%Al were compressed to 20% height reduction and subsequently annealed at 773K (500°C), 873K (600°C), and 1073K (800°C) for various annealing times. The GOS method was used on each sample to measure the area fraction of recrystallized grains and the results were plotted as a function of annealing time as seen in Figure 26. The resulting data points create sigmoidal shaped curves, which are expected for recrystallization kinetics. In order to quantify this trend, the well-known Avrami relationship is used [15], [16]:

$$X = 1 - exp\left[-0.693\left(\frac{t}{t_{0.5}}\right)\right]^n \quad (2)$$

which relates the area fraction of recrystallized grains (X) to the annealing time(t) and includes the time to 50% recrystallization ($t_{0.5}$) and the constant n or the Avrami exponent. The Avrami exponent is determined by plotting log(ln(1/(1-X))) vs. log(t) and determining the slope of a linear curve fit (Figure 27); the time to 50% recrystallization ($t_{0.5}$) is then calculated from the y-intercept. The results for all three annealing temperatures along with the R^2 values, which measure the fit of the curves to the experimental data points, are summarized in Table 5. Although a smaller sample size was used for Ti-0wt%Al at 800°C to minimize sample heat up time as mentioned in section 2.2, only fraction recrystallized values above 0.6 were able to be accurately measured. Due to the lack of information at the beginning of the recrystallization process, it is assumed that Ti-0wt%Al at 800°C will have a similar recrystallization behavior as Ti-0wt%Al at the lower temperatures along with the other alloys at 800°C. Therefore, the Avrami exponent is taken as the average of the other alloys and temperatures and the curve is fit to the data to determine the value for $t_{0.5}$.

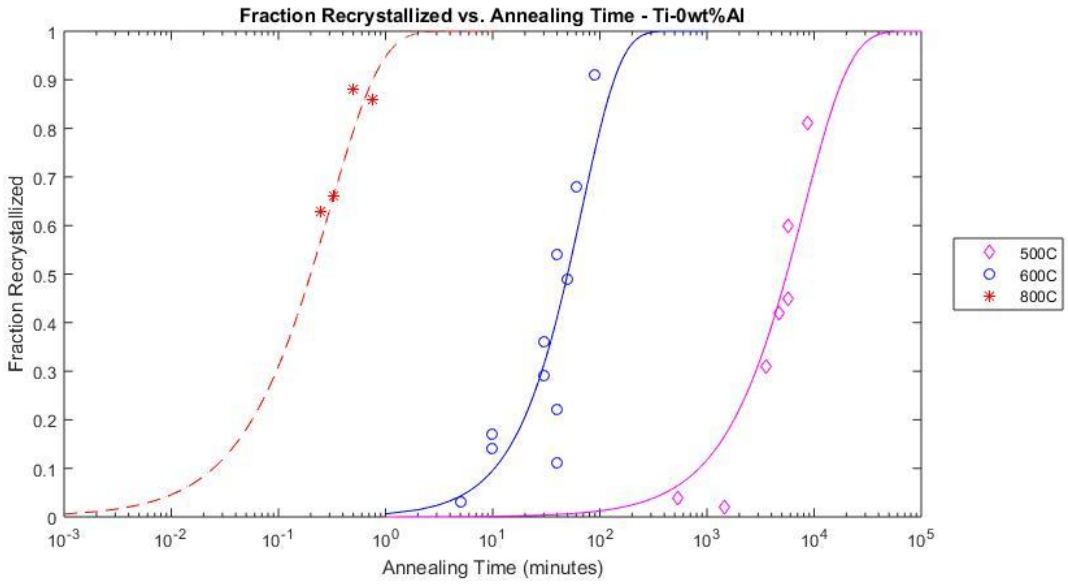

Figure 26. Fraction recrystallized as a function of annealing time for Ti-0Al samples compressed at room temperature and annealed at various temperatures and the corresponding Avrami relationships

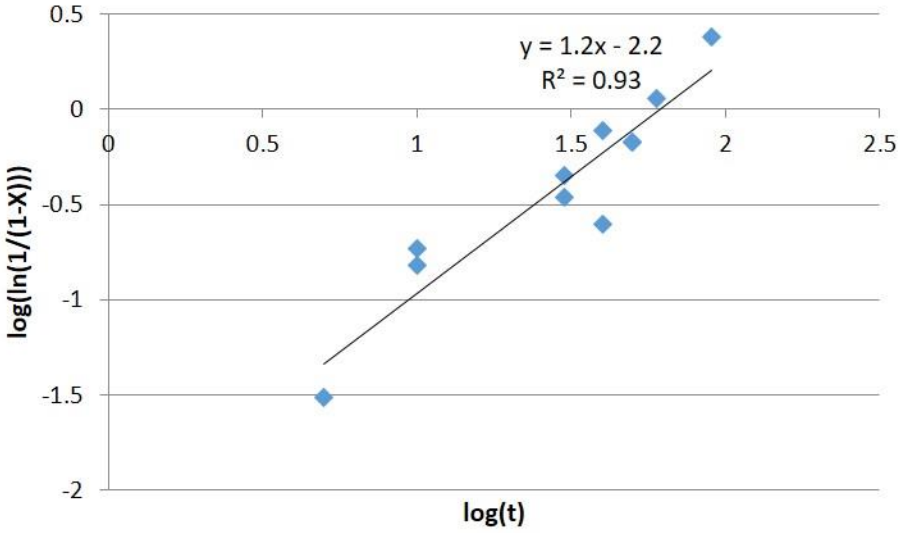

Figure 27. Determination of Avrami constant for Ti-0Al compressed and annealed at 873K (600°C)

Table 5. Summary of $t_{0.5}$ values, Avrami constants and R^2 values for Ti-0Al at varying annealing temperatures

Annealing Temperature	773K (500°C)	873K (600°C)	1073K (800°C)
$t_{0.5}$ (minutes)	6060	50	0.2
n	1.0	1.2	1.0
R^2	0.98	0.96	0.76

Using the values of $t_{0.5}$ as a representation of the SRX kinetics, it is clear that decreasing the annealing temperature significantly retards recrystallization as expected. Plotting $t_{0.5}$ vs annealing temperature reveals the trend that decreasing the annealing temperature exponentially increases $t_{0.5}$.

The value for $t_{0.5}$ for SRX is generally represented by [17]:

$$t_{0.5} = A\varepsilon^{p}\dot{\varepsilon}^{q}exp\left(\frac{Q}{RT}\right) \quad (3)$$

Since the compression in this study is done at a constant strain and strain rate, the activation energy for recrystallization can be determined from Eq 3. An Arrhenius relationship between $t_{0.5}$ and annealing temperature was used to determine the slope giving an activation energy of 230 kJ/mol. Comparing this value to the reported values for the activation energy for bulk self-diffusion in α titanium, 192 kJ/mol [18], and the activation energy for grain boundary self-diffusion in α titanium, 153 kJ/mol [18], shows that the recrystallization activation energy for Ti-0Al is more consistent with that of bulk self-diffusion.

The effect of solute concentration on the SRX kinetics was then studied by compressing samples of all three alloys to 20% height reduction and annealing all samples at 1073K (800°C) for various times. The fraction recrystallized was again determined via the GOS method and the results are plotted in Figure 7. Again the values of $t_{0.5}$ (Table 6) are used as a measure of SRX and it is seen that increasing the solute concentration from 0wt% to 7wt% increases $t_{0.5}$ from less than 1 minute to about 1240 minutes. It is evident that the addition of aluminum to the base titanium strongly retards recrystallization. We attribute this to the effect of solute drag, i.e., the Al solute atoms exert a force on the high angle grain boundaries surrounding recrystallized grains and hinder grain boundary motion [19]–[22].

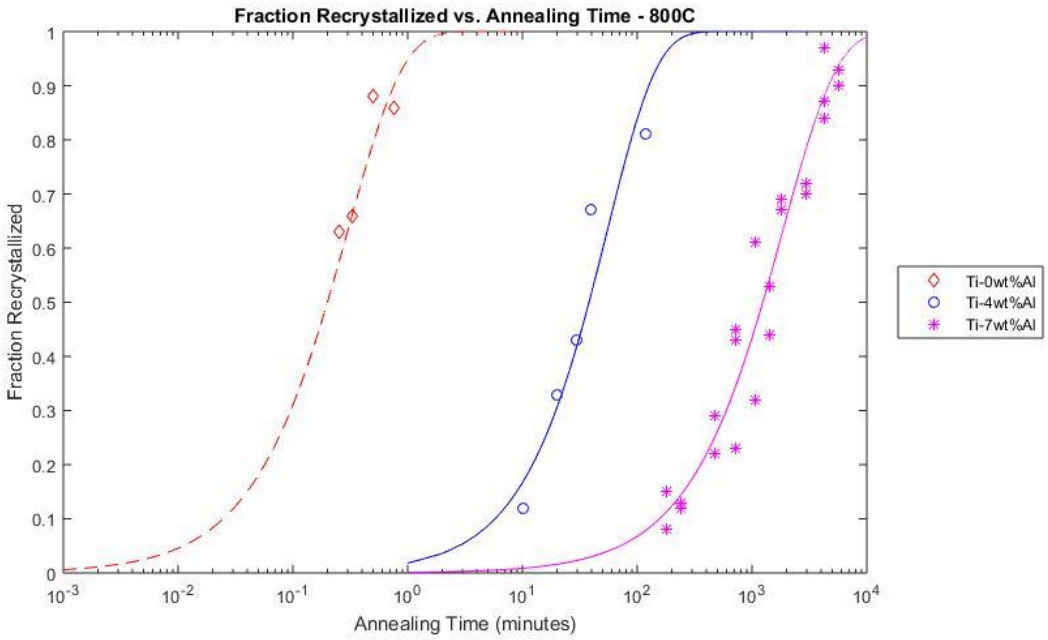

Figure 28. Fraction recrystallized vs. annealing time for all three alloys compressed at room temperature and annealed at 1073K (800°C) and corresponding Avrami curves

Table 6. Summary of $t_{0.5}$ values, Avrami constants and R^2 values for samples of varying aluminum concentration annealed at 1073K (800°C)

Al concentration	**0wt%**	**4wt%**	**7wt%**
$t_{0.5}$ (minutes)	0.2	38	1240
n	1.0	1.0	0.9
R^2	0.76	0.98	0.99

3.3.2 Discussion

The derivation of the JMAK relationship assumes a constant growth rate during the process of recrystallization. With the additional assumption of site saturated nucleation, the derivation will give an ideal Avrami exponent value of 3. A decrease in growth rate over time during recrystallization leads to a decrease in the Avrami exponent, which can explain the experimental Avrami exponent of close to 1. There are multiple factors that can contribute to this decrease in growth rate including recovery, a non-random distribution of nuclei, and a heterogeneous distribution of stored energy. Recovery occurs via dislocation rearrangement and annihilation and decreases the stored energy over time and therefore decreases the driving

force for grain growth. While this does decrease the growth rate, studies have shown that the effect of recovery is not significant enough to account for such a large decrease in the Avrami exponent and therefore is most likely not the main explanation for the difference between the experimental and model results [23]. A non-random distribution of nuclei and heterogeneous distribution of stored energy have been found to cause a significant change in the growth rate and therefore the Avrami exponent. When nuclei are clustered, generally along grain boundaries or in regions of high stored energy, the new grains begin to grow at a constant rate but then impinge on each other due to their close proximity. This grain boundary impingement causes a change from 3D growth to 1D growth during recrystallization and therefore decreases the Avrami exponent. A heterogeneous distribution of stored energy will cause nucleation and rapid growth to preferentially occur in regions of high stored energy first in order to decrease the overall stored energy. Once the regions of high stored energy have been consumed, the recrystallized grains will then continue to grow into regions of lower stored energy, creating a lower driving force and decreasing the rate of growth (Figure 29). Again, this decrease in growth rate during the recrystallization process leads to a reduction in the Avrami exponent. Therefore, it is predicted that the difference between the constant growth rate assumption and the actual microstructural inhomogeneity of the samples that leads to a decrease in growth rate over time explains the variation of the experimental Avrami exponents from the ideal value of 3.

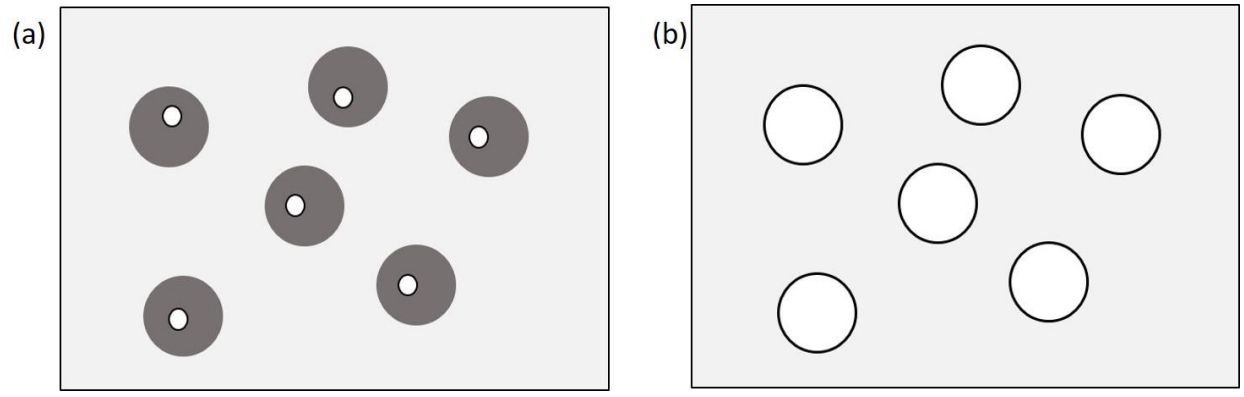

Figure 29. Effect of local variations in stored energy on rate of recrystallization. (a) Nuclei (small white regions) that form within regions of high stored energy (dark gray regions) will at a high growth rate, but (b) once the regions of high stored energy have been consumed, the recrystallized grains will enter regions of lower stored energy (light gray regions) and the growth rate will decrease.

3.3.3 Texture

The change in texture during deformation was investigated by comparing a sample of Ti-4Al that had been only β cogged to a sample of Ti-4Al that had been both β cogged and compressed at room temperature. The texture was measured by EBSD and the results can be seen in Figure 30.

The pole figures of the as-β cogged sample show no obvious preferential texture while the pole figures of the as-compressed sample show a strong basal texture in the compression direction. Therefore, during compression, the grains are rotating such that the [0001] direction is aligning with the compression axis, which agrees with previous results for titanium and other HCP materials [24]–[27].

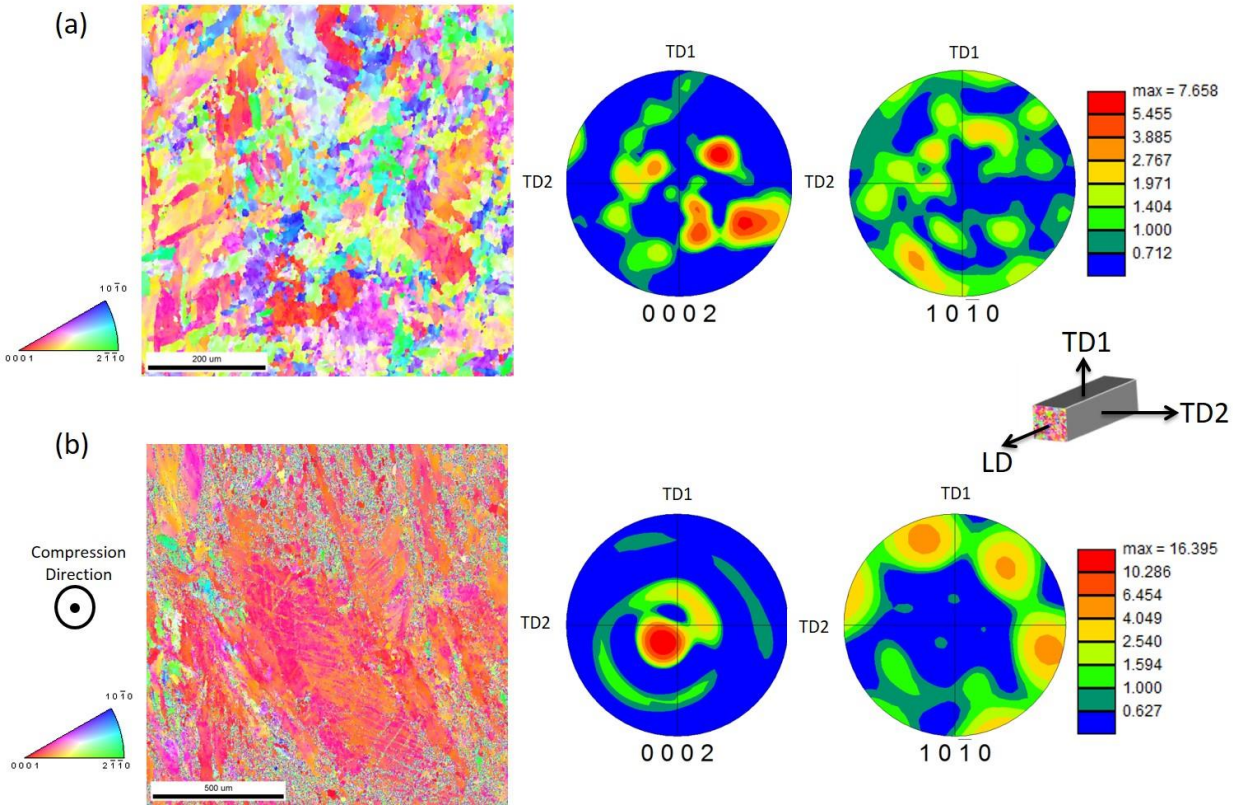

Figure 30. Inverse pole figures (left) and pole figures (right) of Ti-4Al (a) as beta cogged and (b) beta cogged and compressed

The texture evolution during recrystallization was also studied by performing EBSD on samples of Ti-4Al and Ti-7Al that had been β cogged, compressed and annealed at 1073K (800°C) for various times. The results for Ti-4Al samples are shown in Figure 31.

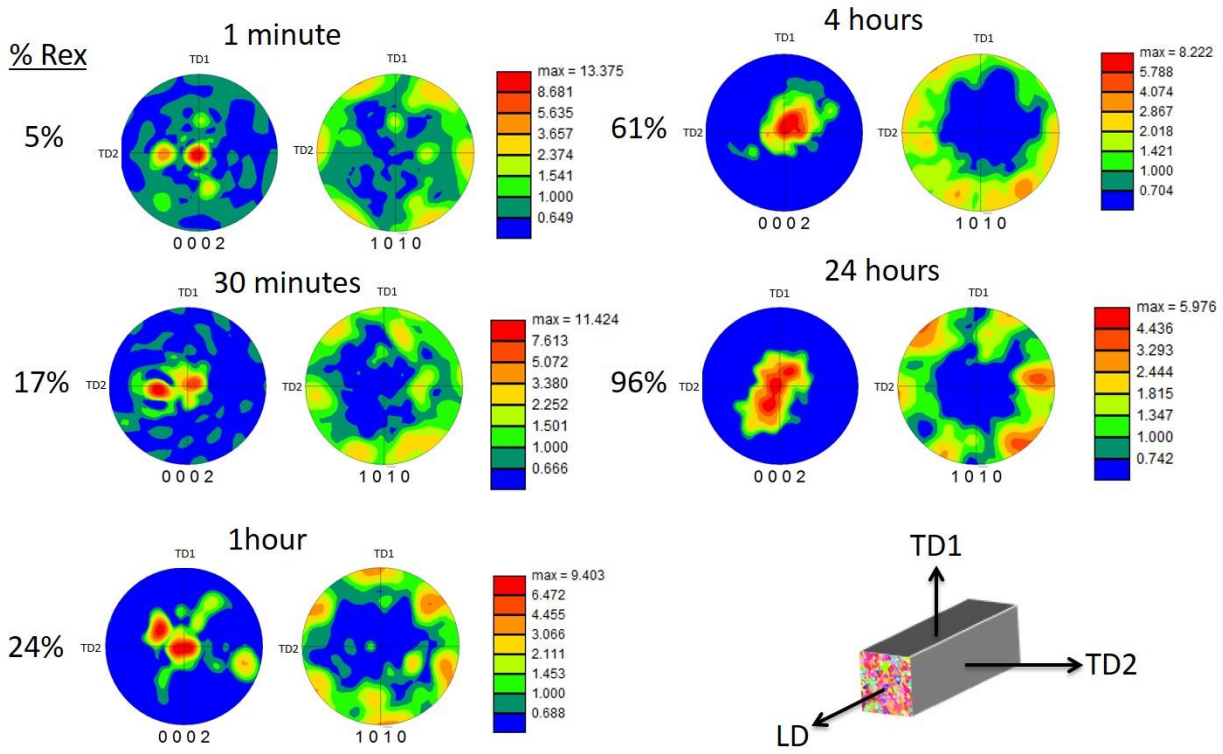

Figure 31. Pole figures for Ti-4Al samples beta cogged compressed and annealed at various times at 1073K (800°C)

The strong basal texture is still observed in the sample annealed for 1 minute. As the annealing time increases, the intensity of the basal texture is reduced but the preferential orientation of the c-axes in the compression direction still remains after 24 hours of annealing and a fully recrystallized microstructure. Therefore, either new grains are preferentially nucleating with a basal texture or the nuclei with that orientation are growing faster than grains with other orientations. The evolution of the maximum intensity with respect to fraction recrystallized is plotted for both Ti-4Al and Ti-7Al in Figure 32 and a general trend of texture weakening with recrystallization can be seen.

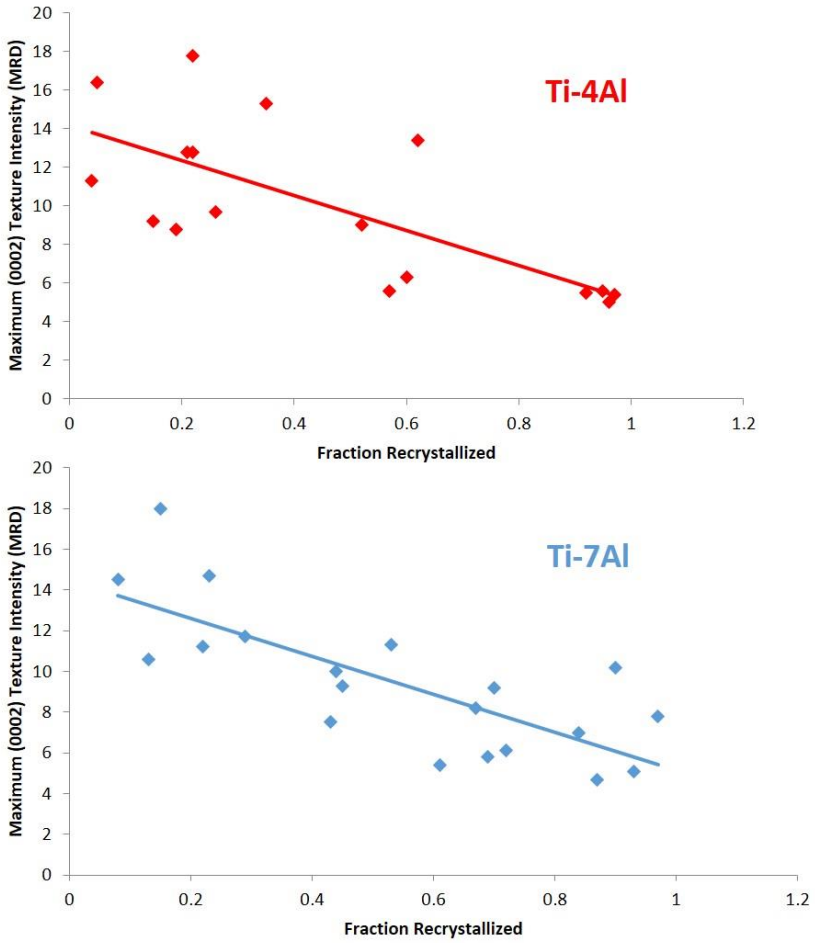

Figure 32. Evolution of (0002) texture intensity while annealing at 1073K (800°C) with respect to increasing fraction recrystallized for Ti-4Al and Ti-7Al after room temperature compression

3.4 Analytical Modeling Approach

3.4.1 Model framework

Analytical models have been developed to predict the influence of thermomechanical processing and alloying on static recrystallization kinetics [28]–[30]. The general modelling approach used in this work is based on the approach suggested by Aretxabaleta et al. [29] for steels. It was chosen because it includes the effect of solute concentration on SRX kinetics and the framework is based on the JMAK relationship.

The framework of this approach is based on a generalized JMAK relationship assuming a random distribution of nuclei and site-saturation conditions:

$$X_{REX} = 1 - exp\left[-N_{REX}\left(\int_0^t MF_{REX}(t)dt\right)^3\right] \quad (4)$$

where X_{REX} is the fraction recrystallized, N_{REX} is the initial number of recrystallization nuclei, M is the high angle grain boundary (HAGB) mobility and F_{REX} is the driving force for recrystallization. While this model was designed to include the effects of recovery by measuring the change in dislocation density with time and updating the driving force accordingly, the effect of recovery is considered to be negligible in this work as will be described in the discussion section. Therefore, the driving force is considered to be constant and the relationship can be simplified to:

$$X_{REX} = 1 - exp[-N_{REX}(MF_{REX}t)^3] \quad (5)$$

3.4.2 Model parameters

The driving force is directly related to the dislocation density, ρ, as follows:

$$F_{REX} = \frac{1}{2}\rho\mu b^2 \quad (6)$$

where μ is the temperature dependent shear modulus and b is the Burgers vector. The dislocation density can be determined by the flow stress, σ:

$$\sigma = \sigma_y + \bar{M}\alpha_T\mu b\sqrt{\rho} \quad (7)$$

where σ_y is the yield stress of the material, $\bar{M}$ is the Taylor factor, and α_T is a constant. The flow stress in this work is defined as the final flow stress after deformation and therefore the initial flow stress before annealing and recrystallization. The yield stress for the three alloys was determined via tensile tests performed on the beta cogged materials. The shear moduli were calculated from the elastic moduli also determined via the tensile tests by assuming isotropic deformation. The flow stress values were determined using the Abaqus simulation described is section 2.2. The simulation was conducted for all three alloys. For each alloy simulation, the average calculated flow stress was determined from the center region of the sample. This is the same region where all experimental measurements are taken. The resulting yield and flow

stress values are listed in Table 7. Eqs 6 and 7 are combined to calculate the driving force as follows:

$$F_{REX} = \frac{1}{2}\left(\frac{\sigma-\sigma_y}{\bar{M}\alpha_T}\right)^2 \frac{1}{\mu} \quad (7b)$$

Table 7. Alloys specific inputs for determining recrystallization driving force

Model Input	Ti-0wt%Al	Ti-4wt%Al	Ti-7wt%Al
σ_y, yield stress (determined experimentally from tensile stress strain curves)	311 MPa	586 MPa	736 MPa
σ, flow stress (determined from Abaqus simulations)	369 MPa	639 MPa	747 MPa
μ, Shear modulus (determined experimentally from tensile stress strain curves)	40.3 GPa	47.5 GPa	51.1 GPa
ρ, dislocation density (calculated from Eq 7)	$4.6\text{x}10^{13}$ m^{-2}	$2.7\text{x}10^{13}$ m^{-2}	$1.0\text{x}10^{12}$ m^{-2}
F_{REX}, driving force (calculated from Eq 6)	$8.0\text{x}10^{4}$ Pa	$5.7\text{x}10^{4}$ Pa	$2.3\text{x}10^{3}$ Pa

The initial number of recrystallized nuclei is calculated as a function of the final grain size of the fully recrystallized material, D_{REX}, which was determined experimentally. The relationship between N_{REX} and D_{REX} is (22):

$$N_{REX} = \left[\frac{4}{3}\pi\left(\frac{D_{REX}}{2}\right)^3\right]^{-1} \quad (8)$$

This relationship approximates the number of initial nuclei by assuming that for every volume of an average sized fully recrystallized grain, there was initially one nuclei within that volume. Due to experimental variability, the fully recrystallized grain size varies slightly from sample to sample however, the measured values for multiple samples from all three alloys fall within the range of 40μm to 50μm. Therefore, an average value of 45μm is used as input to the model.

In this model, the variable that takes into account the effect of solute concentration is the mobility of high angle grain boundaries. The relationship between mobility and solute concentration used in this model was originally developed by Cahn [31]. It was derived by first calculating a composition profile of impurity atoms along a grain boundary moving at a constant velocity. Then the drag force exerted by the solute atoms on the grain boundary is calculated and added to the intrinsic drag force. The cases of high and low grain boundary

velocities were analyzed separately and approximated limiting laws for the solute drag force as a function of concentration for the two regimes were derived. The relationship for the low velocity case is used in this work because the velocity values that result from this relationship are similar to those values approximated from experimental grain size measurements. For the low velocity regime, according to Cahn's model the mobility can be calculated as:

$$M_s = \left(\frac{1}{M_{INT}} + \alpha C_s\right)^{-1} \tag{9}$$

where C_s is the solute concentration, M_{INT} is the intrinsic mobility or the mobility in the solute free material, and α is a constant calculated as:

$$\alpha = \frac{\delta N_V (kT)^2}{E_b D}\left(sinh\left(\frac{E_b}{kT}\right) - \left(\frac{E_b}{kT}\right)\right) \tag{10}$$

δ is the grain boundary width that is assumed to be 0.5nm, N_V is the number of atoms per unit volume, E_b is the binding energy of solute atoms to grain boundaries and D is the cross boundary diffusion coefficient. The two parameters that have the most influence on the solute drag are the binding energy and the cross boundary diffusivity. The binding energy is calculated using Cottrell's formula [32] that assumes a grain boundary is made up of dislocations and measures how nearby solute atoms affect the stress around the dislocations:

$$E_b = \frac{4}{3} r_b^3 \mu \frac{1+\nu}{1-\nu}\left|\frac{r_b - r}{r_b}\right| \tag{11}$$

v is the Poisson's ratio of the bulk material, r_b is the atomic radius of the bulk material, and r is the atomic radius of the solute. The cross boundary diffusivity is a parameter that is not well known or easily measured and therefore is often approximated as a multiple of the diffusivity of the solute atoms in the bulk material, D_b. Therefore, a multiplication factor, D_f, is added to Eq. 11 that is used for fitting purposes [29]:

$$\alpha = \frac{\delta N_V (kT)^2}{E_b D_b \boldsymbol{D_f}}\left(sinh\left(\frac{E_b}{kT}\right) - \left(\frac{E_b}{kT}\right)\right) \tag{12}$$

All of the material constants used in this model are listed in Table 9.

Since the intrinsic mobility, M_{INT}, is the HAGB mobility in the solute free material, the experimental results for Ti-0Al are used to determine this value. N_{REX} and F_{REX} are calculated for Ti-0Al using Eq 8 and Eq 7b, respectively and are inserted into Eq 5. An experimental (t,X) data point (values at $t_{0.5}$ were chosen in this work) can then be used to solve for the intrinsic mobility. This was done for the 3 experimental annealing temperatures (Table 8) and a relationship between M_{INT} and annealing temperature was developed (Figure 33):

$$M_{INT} = 16exp\left(\frac{-234995}{RT}\right) \quad (13)$$

where R is the gas constant and T is the annealing temperature in Kelvin.

Table 8. Intrinsic mobility values calculated from model using Ti-0Al experimental (t,X) data points

Annealing Temperature	**Mobility (m^4/Js)**
773K (500°C)	$1.7x10^{-15}$
873K (600°C)	$2.0x10^{-13}$
1073K (800°C)	$5.0x10^{-11}$

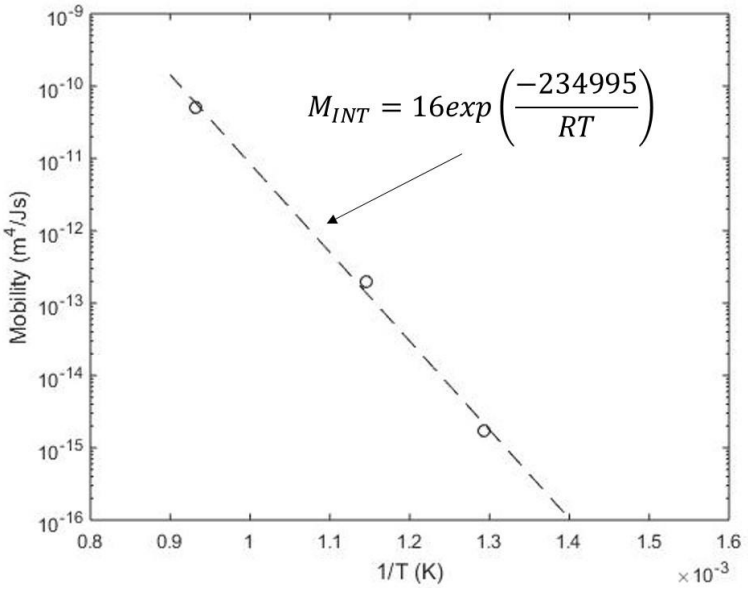

Figure 33. Relationship between annealing temperature and intrinsic grain boundary mobility for Ti-0Al

Table 9. Material constants used in SRX model

$\bar{M}$, Taylor factor	4.8 [33]
N_v, # of atoms per unit volume	5.66e28 atoms/m^3 (calculated using molar volume of titanium)
E_b, Binding energy	2.34e-19 J (calculated from Eq. 12)
D_{REX}, recrystallized grain size	45μm (determined experimentally)
b, Burgers vector	0.295nm ($\vec{a}$ dislocation in titanium) [34]
α_T, geometric constant	0.15 [29]
D_b, bulk diffusivity of Al in α-Ti	5e-18 m^2/s [35]

3.4.3 Discussion

In order to compare the analytical model and the experimental results, the D_f fitting factor was used to fit the model curves to the experimental values for $t_{0.5}$ at 800°C. This fitting was done for the T-4Al case and tested by extrapolation to Ti-7Al condition. The required fitting D_f value for Ti-4Al is approximately $4.2x10^7$, indicating that the cross grain boundary diffusivity of Al in Ti is about seven orders of magnitude greater than the bulk diffusivity of Al in Ti at 1073K (800°C). Although grain boundary diffusion information is not available for Al in Ti, the grain boundary self-diffusion at 1073K (800°C) in α-Ti has been calculated to be 10^7 faster than bulk self-diffusion in α-Ti [18]. Although this is consistent with the value of D_f determined in the current work, there is a need for a more physically based determination of this quantity. For the purposes of the current work, this parameter is used primarily to capture the experimentally observed phenomena. To compare the effect of solute concentration on recrystallization kinetics between the model and the experimental results, the fitting factor, D_f, was first adjusted so that the resulting $t_{0.5}$ value for Ti-4Al matched the experimental value. Then, holding D_f constant, the solute concentration was changed to 7% (along with the corresponding values for shear modulus, flow stress, and yield stress), resulting in a model value for $t_{0.5}$ of 1686 minutes. This is a reasonable estimate of the experimental $t_{0.5}$ value for Ti-7Al of 1240 minutes. As shown in Figure 34, both the experimental results and the model

results (with a best fit line) using a constant D_f value showing reasonably good agreement between the model and the experiments.

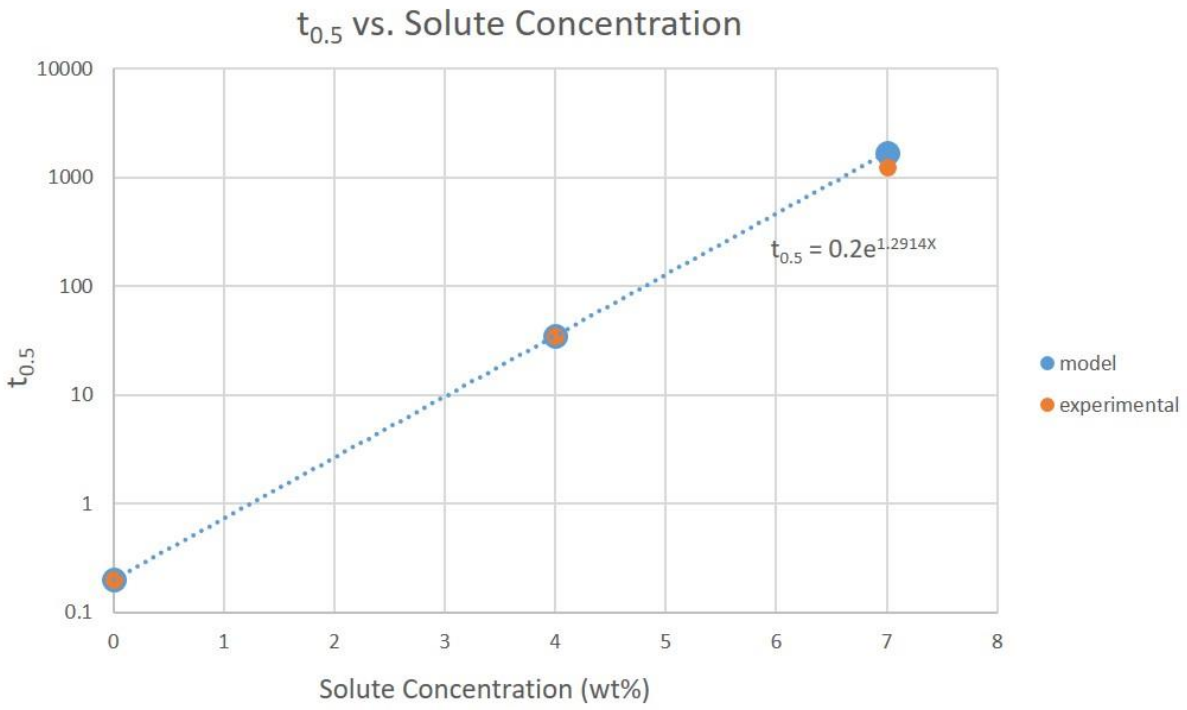

Figure 34. Effect of solute concentration on the SRX kinetics as predicted by the SRX model (using Cahn's model for solute drag) and experimentally. The model results are artificially fitted to the experimental data point for Ti-4Al using the Df fitting factor of $4.2x10^7$ and then predictions are made for other solute concentrations (e.g.7%) while holding D_f constant and the resulting $t_{0.5}$ is plotted.

As seen in Eq 9, the Cahn model predicts a linear inverse relationship between mobility and solute concentration. However, we have observed that $t_{0.5}$ increases exponentially with solute concentration. Since the model does capture the change in kinetics, a decrease in grain boundary mobility due to solute drag is not the only factor slowing down the recrystallization kinetics. As seen from the values in Table 7, the difference between yield stress and flow stress rapidly decreases with increasing aluminum content resulting in a lower dislocation density (for a given strain level) and a decrease in the driving force. This indicates that, for the current investigation, changes in the driving force also had a significant impact on the recrystallization kinetics of these Ti alloys. This is attributed to a decreasing work hardening rate during deformation with increasing aluminum content. As discussed in Chapter 2, this can be

explained by the suppression of twinning by the addition of aluminum. Twin boundaries hinder dislocation motion and therefore increase the work hardening rate. Figure 35 compares the trends in driving force and grain boundary mobility with respect to aluminum concentration. The driving force was determined from equation 6 and the values are listed in Table 7. There is a significant decrease in mobility between 0wt% and 4wt%Al but a much smaller decrease between 4wt% and 7wt%Al. However, there is a larger decrease in driving force between 4wt% and 7wt%Al than there is between 0wt% and 4wt%Al. In conclusion, it is the combined effects of solute atoms in reducing the grain boundary mobility and reducing the driving force (from reduced work hardening) that lead to the significant retardation of the static recrystallization kinetics in titanium with the addition of aluminum. The specific source of the reduced mobility due to solutes will be further expanded on in Chapter 5.

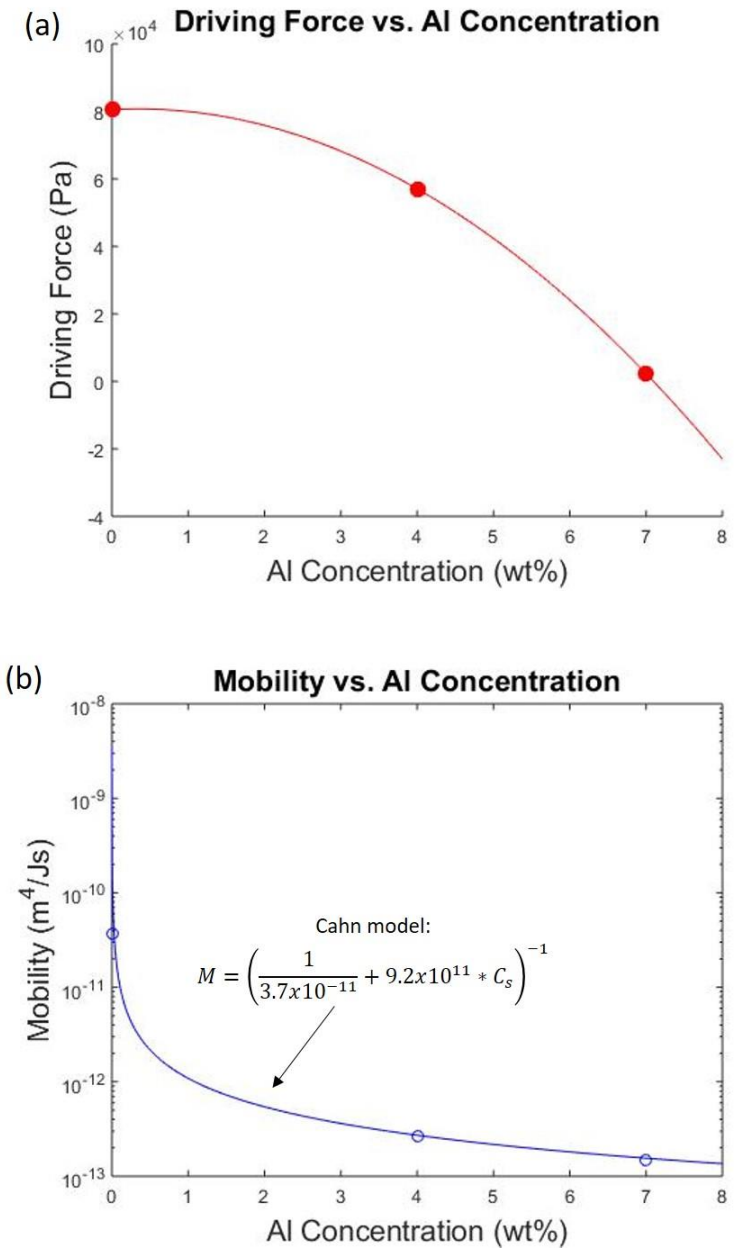

Figure 35. Model results for driving force and grain boundary mobility with respect to aluminum concentration (blue dashed lines are best fit curves to show general trends)

The results of this chapter will be used to develop and validate computational models (specifically combined crystal plasticity finite element and phase field models) that will allow for the prediction of the kinetics and microstructural evolution of titanium throughout the recrystallization process. These computational tools will be extremely valuable for both alloy development and determining thermomechanical processing variables to achieve specific

desired material properties. This work has shown how sensitive the recrystallization kinetics are to both aluminum concentration and processing conditions. Therefore, having these effects experimentally quantified and incorporated into models is extremely valuable.

3.5 Conclusions

- In pure titanium, decreasing the annealing temperature slows down the static recrystallization kinetics exponentially. Decreasing the annealing temperature from 1073K (800°C) to 773K (500°C) increases the time to 50% recrystallization from less than 1 minute to 6060 minutes.
- The resulting recrystallization activation energy for pure titanium is consistent with that of bulk self-diffusion of titanium.
- The addition of aluminum has a strong effect on the static recrystallization kinetics in α-titanium. Increasing the aluminum content from 0wt% to 7wt% increases the time to 50% recrystallization from less than 1 minute to 1240 minutes.
- The studied alloys exhibit recrystallization behavior resulting in an Avrami exponent of approximately 1. This is attributed to a change from 3D growth to 1D for strain free grains during recrystallization, which we conclude is due to an inhomogeneous distribution of nuclei because of impingement.
- An analytical model was used to successfully capture the significant retardation effect that aluminum has on the static recrystallization kinetics of titanium. This model indicates that the retardation in recrystallization is due to two separate factors, a reduction in driving force due to the higher work hardening as aluminum content increases coupled with a reduction in grain boundary mobility due to solute drag.
- Deformation leads to strong basal texture in the compression direction that is weakened but not removed during recrystallization.

3.6 References

[1] S. P. Gentry and K. Thornton, “Simulating recrystallization in titanium using the phase field method,” in *IOP Conference Series: Materials Science and Engineering*, 2015, vol. 89, no. 012024.

[2] V. Sundararaghavan, a. Kumar, and S. Sun, “Crystal plasticity simulations using nearest neighbor orientation correlation function,” *Acta Mater.*, vol. 93, pp. 12–23, 2015.

[3] H. L. Andrade, M. G. Akben, and J. J. Jonas, “Effect of Molybdenum , Niobium , and Vanadium on Static Recovery and Recrystallization and on Solute Strengthening in Microalloyed Steels,” *Metall. Trans. A*, vol. 14A, no. October, pp. 1967–1977, 1983.

[4] S. F. Medina and J. E. Mancilla, “Static Recrystallization Modelling in Hot Deformed Steels Containing Several Alloying Elements,” *ISIJ Int.*, vol. 36, no. 8, pp. 1070–1076, 1996.

[5] Z. Zhang, Y. Liu, X. Liang, and Y. She, “The effect of Nb on recrystallization behavior of a Nb micro-alloyed steel,” *Mater. Sci. Eng. A*, vol. 474, no. 1–2, pp. 254–260, Feb. 2008.

[6] C. Roucoules, S. Yue, and J. J. Jonas, “Effect of Alloying Elements on Metadynamic Recrystallization in HSLA Steels,” *Metall. Mater. Trans. A*, vol. 26A, pp. 181–190, 1995.

[7] D. He, J. C. Zhu, Z. H. Lai, Y. Liu, and X. W. Yang, “An experimental study of deformation mechanism and microstructure evolution during hot deformation of Ti–6Al–2Zr–1Mo–1V alloy,” *Mater. Des.*, vol. 46, pp. 38–48, Apr. 2013.

[8] L. Cheng, H. Chang, B. Tang, H. Kou, and J. Li, “Deformation and dynamic recrystallization behavior of a high Nb containing TiAl alloy,” *J. Alloys Compd.*, vol. 552, pp. 363–369, Mar. 2013.

[9] O. De-lai, W. Ke-lu, and C. U. I. Xia, “Dynamic recrystallization of Ti-6Al-2Zr-1Mo-1V in beta forging process,” *Trans. Nonferrous Met. Soc. China*, vol. 22, no. 4, pp. 761–767, 2012.

[10] P. Lin, A. Feng, S. Yuan, G. Li, and J. Shen, “Microstructure and texture evolution of a near-α titanium alloy during hot deformation,” *Mater. Sci. Eng. A*, vol. 563, pp. 16–20, Feb. 2013.

[11] M. Hayashi, H. Yoshimura, M. Ishii, and H. Harada, “Recrystallization behavior of comercially pure titanium during hot rolling.” Nippon Steel Techinal Report, 1994.

[12] V. M. Miller, A. E. Johnson, C. J. Torbet, and T. M. Pollock, “Recrystallization and the Development of Abnormally Large Grains After Small Strain Deformation in a

Polycrystalline Nickel-Based Superalloy," *Metall. Mater. Trans. A*, vol. 47, no. 4, pp. 1566–1574, 2016.

[13] V. M. Miller and T. M. Pollock, "Texture Modification in a Magnesium-Aluminum-Calcium Alloy During Uniaxial Compression," *Metall. Mater. Trans. A*, vol. 47, no. 4, pp. 1854–1864, 2016.

[14] L. N. Brewer, D. P. Field, and C. C. Merriman, "Mapping and Assessing Plastic Deformation Using EBSD," *Electron Backscatter Diffr. Mater. Sci.*, pp. 251–262, 2009.

[15] W. Johnson and R. Mehl, "Reaction kinetics in processes of nucleation and growth," *Trans. Am. Inst. Min. Metall. Eng.*, vol. 135, pp. 416–442, 1939.

[16] M. Avrami, "Kinetics of Phase Change . I General Theory," *J. Chem. Phys.*, vol. 7, no. 12, pp. 1103–1112, 1939.

[17] L. Cheng, H. Chang, B. Tang, H. Kou, and J. Li, "Characteristics of metadynamic recrystallization of a high Nb containing TiAl alloy," *Mater. Lett.*, vol. 92, pp. 430–432, Feb. 2013.

[18] C. Herzig, R. Willecke, and K. Vieregge, "Self-diffusion and fast cobalt impurity diffusion in the bulk and in grain boundaries of hexagonal titanium," *Philos. Mag.*, vol. 63, no. 5, pp. 949–958, 1991.

[19] T. Schambron, L. Chen, T. Gooch, A. Dehghan-Manshadi, and E. V. Pereloma, "Effect of Mo Concentration on Dynamic Recrystallization Behavior of Low Carbon Microalloyed Steels," *Steel Res. Int.*, vol. 84, no. 12, pp. 1191–1195, Dec. 2013.

[20] E. I. Galindo-Nava, A. Perlade, and P. E. J. Rivera-Díaz-del-Castillo, "A thermostatistical theory for solid solution effects in the hot deformation of alloys: an application to low-alloy steels," *Model. Simul. Mater. Sci. Eng.*, vol. 22, no. 1, p. 015009, Jan. 2014.

[21] A. Momeni and S. M. Abbasi, "On the opposition of dynamic recrystallization and solute dragging in steels," *J. Alloys Compd.*, vol. 622, pp. 318–326, Feb. 2015.

[22] H. Sun and C. Deng, "Adapted solute drag model for impurity-controlled grain boundary motion," *J. Mater. Res.*, vol. 29, no. 12, pp. 1369–1375, Jul. 2014.

[23] F. J. Humphreys and M. Hatherly, *Recrystallization and Related Annealing Phenomena*, 2nd ed. Elsevier Science, 2004.

[24] J. L. W. Warwick, N. G. Jones, K. M. Rahman, and D. Dye, "Lattice strain evolution during tensile and compressive loading of CP Ti," *Acta Mater.*, vol. 60, no. 19, pp. 6720–6731, Nov. 2012.

[25] F. Coghe, W. Tirry, L. Rabet, D. Schryvers, and P. Van Houtte, “Importance of twinning in static and dynamic compression of a Ti–6Al–4V titanium alloy with an equiaxed microstructure,” *Mater. Sci. Eng. A*, vol. 537, pp. 1–10, Mar. 2012.

[26] F. Kabirian, A. S. Khan, and T. Gnäupel-Herlod, “Visco-plastic modeling of mechanical responses and texture evolution in extruded AZ31 magnesium alloy for various loading conditions,” *Int. J. Plast.*, vol. 68, pp. 1–20, May 2015.

[27] Y. . Wang and J. . Huang, “Texture analysis in hexagonal materials,” *Mater. Chem. Phys.*, vol. 81, no. 1, pp. 11–26, Jul. 2003.

[28] M. K. Rehman and H. S. Zurob, “A Novel Approach to Model Static Recrystallization of Austenite During Hot Rolling of Nb Microalloyed Steel. Part I: Precipitate-Free Case,” *Metall. Mater. Trans. A*, vol. 44, no. 4, pp. 1862–1871, Nov. 2012.

[29] Z. Aretxabaleta, B. Pereda, and B. López, “Analysis of the Effect of Al on the Static Softening Kinetics of C-Mn Steels Using a Physically Based Model,” *Metall. Mater. Trans. A*, vol. 45, no. 2, pp. 934–947, Oct. 2013.

[30] P. J. Hurley and F. J. Humphreys, “Modelling the recrystallization of single-phase aluminium,” *Acta Mater.*, vol. 51, no. 13, pp. 3779–3793, Aug. 2003.

[31] J. W. Cahn, “The impurity-drag effect in grain boundary motion,” *Acta Mater.*, vol. 10, pp. 789–798, 1962.

[32] E. A. Simielli, S. Yue, and J. J. Jonas, “Recrystallization Kinetics of Microalloyed Steels Deformed in the Intercritical Region,” *Metall. Mater. Trans. A*, vol. 23A, pp. 597–608, 1992.

[33] M. Morita and O. Umezawa, “Slip Deformation Analysis Based on Full Constraints Model for α-Titanium Alloy at Low Temperature,” *Mater. Trans.*, vol. 52, no. 8, pp. 1595–1602, 2011.

[34] Q. Sun, Q. Guo, X. Yao, L. Xiao, J. R. Greer, and J. Sun, “Size effects in strength and plasticity of single-crystalline titanium micropillars with prismatic slip orientation,” *Scr. Mater.*, vol. 65, no. 6, pp. 473–476, Sep. 2011.

[35] Y. Mishin and C. Herzig, “Diffusion in the Ti-Al System,” *Acta Mater.*, vol. 48, pp. 589–623, 2000.

Chapter 4. The Effect of Microstructural Heterogeneities on the Static Recrystallization Kinetics

4.1 Introduction and Motivation

Static recrystallization kinetics generally take the form of a sigmoidal curve when plotting the fraction of recrystallized grains with respect to annealing time. The shallow slope at short annealing times is due to the time it takes for nuclei to grow to a critical radius and begin to grow into the deformed material. This is followed by the rapid growth of recrystallized grains that produces the steeper slope at intermediate annealing times. At longer annealing times, a decreasing slope is observed due to the decreasing amount of deformed regions in the materials and therefore the decreasing driving force for recrystallization along with the impingement of recrystallized grains. This trend is often quantified using the Johnson-Mehl-Avrami-Kolmogorov (JMAK) equation that relates X, the fraction recrystallized, to t, the annealing time [1], [2]:

$$X = 1 - exp[-B(t)^n] \tag{1}$$

where $t_{0.5}$ is the time to 50% recrystallization and n is the Avrami exponent. A number of assumptions were made in developing this relationship, the most important being that the nuclei that form during recrystallization are randomly distributed throughout the material. Given the additional assumptions that these nuclei form at a rate $\dot{N}$ and the recrystallized grains that come from these nuclei grow into the deformed material at a constant growth rate of $\dot{G}$, the JMAK equation is derived to be:

$$X = 1 - exp\left(\frac{-f\dot{N}\dot{G}^3 t^4}{4}\right) \tag{2}$$

where f is a shape factor. Therefore, for this case, the Avrami exponent is derived to be equal to four. In the case of static recrystallization, the assumption of site-saturated nucleation is also made meaning all nuclei are present at the start of recrystallization. This is a reasonable assumption for static recrystallization because of the high amount of stored energy in the material before recrystallization and the absence of further deformation during heating such as occurs during dynamic recrystallization. In the site saturation case, a constant number of nuclei, N, are assumed to exist and the JMAK equation is reduces to:

$$X = 1 - exp\left(fN\left(\dot{G}t\right)^3\right) \tag{3}$$

Therefore, with the assumptions of a random distribution of nuclei, a constant growth rate, and site saturated nucleation, an ideal Avrami exponent value of three is expected. However, an Avrami exponent, n, of three is very rarely seen experimentally. Lower values of n, often close to one, are seen in a variety of metals such as steel [3], [4], copper alloys [5], [6], magnesium alloys [7], along with titanium alloys [8]–[10]. This decrease in n from the ideal value of three is frequently attributed to a non-constant growth rate throughout the recrystallization process that can be caused by recovery along with inhomogeneities in stored energy and nuclei distribution. An inhomogeneous distribution of stored energy will create regions of the material with high stored energy and regions of the material with low stored energy. The grain boundaries of a recrystallized grain in a region of high stored energy will have a high velocity due to the large driving force. However, once those grain boundaries reach a region of lower stored energy, their velocity will slow down due to the decreasing driving force. This will create a decreasing growth rate of those recrystallized grains and therefore a lower Avrami exponent. Similarly, if nuclei are clustered to together in regions of high stored energy or along grain boundaries, they can grow at a given growth rate until they begin to impinge on each other, at which point their growth will be halted in the direction of the impinged grain boundary. This will also decrease their growth rate and therefore lower the Avrami exponent.

The previous work on the static recrystallization kinetics of binary alpha Ti-Al alloys, as described in Chapter 3, has consistently measured the Avrami exponent to be approximately equal to one for various compositions and annealing temperatures [11]. We hypothesize that

this is due to the heterogeneous nature of the nucleation sites. The goal of this work is to analyze and quantify the inhomogeneity of nuclei distribution during static recrystallization of binary alpha Ti-Al alloys in order to explain the result of the low Avrami exponent observed in single phase Ti and Ti-Al binary alloys. These results will also be compared to a phase field simulation conducted both with a random and non-random distribution of nuclei to show the effect of the distribution on the Avrami exponent value. The non-random simulation also made use of an integrated computational approach that linked crystal plasticity calculations of stored energy with phase field simulations of nucleation and growth of recrystallized grains.

4.2 Experimental Methods

4.2.1 The free surface fraction

To describe the heterogeneity of microstructure, the free surface fraction, S_v, is frequently used [12]. S_v is a measure of the total area per unit volume of unimpinged, free to move grain boundaries that separate recrystallized and unrecrystallized regions [12]. At early stages of recrystallization when recrystallized grains are small, S_v is low since the total area of grain boundaries is proportional to the grain size. As the average recrystallized grain size begins to increase, the value of S_v will increase as well. As time progresses, the recrystallized grains begin to impinge on each other, and the area of impinged grain boundaries is no longer included in the calculation of S_v, causing a decrease in the free surface fraction. The S_v value will continue to decrease to zero as the microstructure approaches fully recrystallized and there are no longer any grain boundaries that separate recrystallized and unrecrystallized regions. Therefore, plotting the free surface fraction with respect to fraction recrystallized will create a bell shaped curve. If the microstructure includes a perfectly random distribution of nuclei, then the value of S_v should peak at a fraction recrystallized of exactly 0.5. This trend is shown in Figure 36 where Vandermeer et al. [12] plotted the theoretical relationship between the free surface fraction and the fraction recrystallized. The solid line represents the case of site saturated nucleation and random nuclei distribution and peaks at a fraction recrystallized of exactly 0.5.

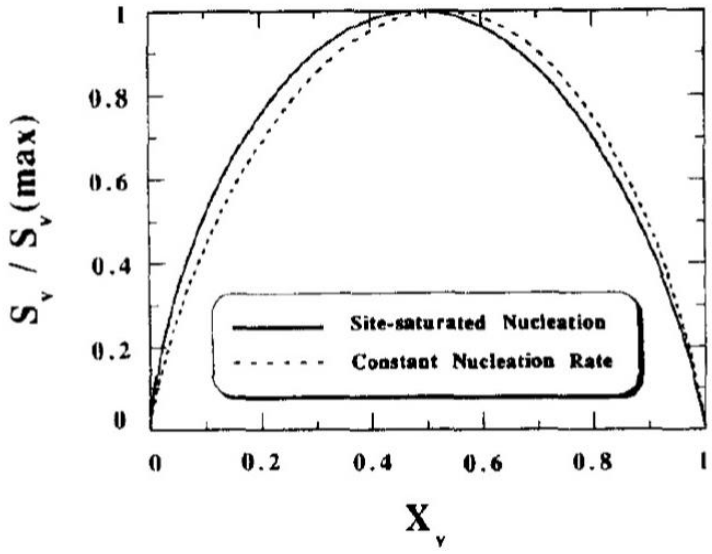

Figure 36. Theoretical plot of the relative free surface fraction with respect to the fraction recrystallized for site saturated nucleation (solid line) and random nuclei distribution showing a peak at 0.5. [12]

However, if there is a non-random distribution of nuclei or clustering of nuclei, then those recrystallized grains will begin to impinge on each other earlier than for a random distribution. Therefore, clustering of nuclei will cause the plot of S_v vs. fraction recrystallized to peak before a fraction recrystallized of 0.5. This trend has been seen experimentally both in aluminum [13], [14] and iron [12] and the S_v characteristic has also been included in recrystallization models in order to account for the effects of impingement [12]–[16]. An example of this asymmetry can be seen in Figure 37, which shows results from Vandermeer and Jensen [13] for a commercial aluminum alloy. The S_v values for this alloy peak between 0.3 and 0.4 fraction recrystallized.

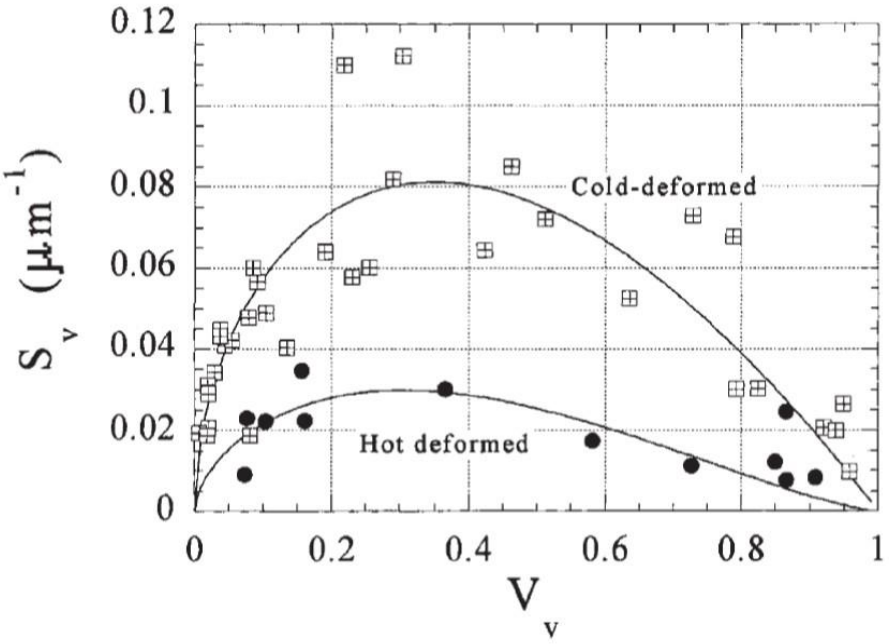

Figure 37. Sv vs. Fraction Recrystallized of AA 1050 commercial aluminum [13]

A previous method for experimentally measuring the value of S_v uses a line intercept method on 2D micrographs [14]. This is done by drawing randomly oriented test lines of known length across a micrograph. The number of intersections each line makes with an unimpinged grain boundary separating a deformed region from a recrystallized grain is counted and divided by the line length. S_v is then calculated as:

$$S_v = 2N_L \tag{4}$$

where N_L is the number of intersections per unit line length. However, a different method for experimentally measuring S_v is used in this work and is detailed in the following section.

4.2.2 S_v Measurement Technique

The previous work on static recrystallization of binary alpha titanium alloys used electron backscatter diffraction (EBSD) to image the microstructures of three alloys throughout the recrystallization process [11]. Grain orientation spread (GOS) was then used to quantify the fraction recrystallized by labeling all grains with a GOS value of 1° or less to be recrystallized.

Each of these EBSD images were then filtered so that only the recrystallized grains remained and all deformed regions are represented in black as seen in Figure 38. This was done by partitioning the data of each EBSD scan to only include grains with a GOS value of 1° or less using TSL OIM Analysis software.

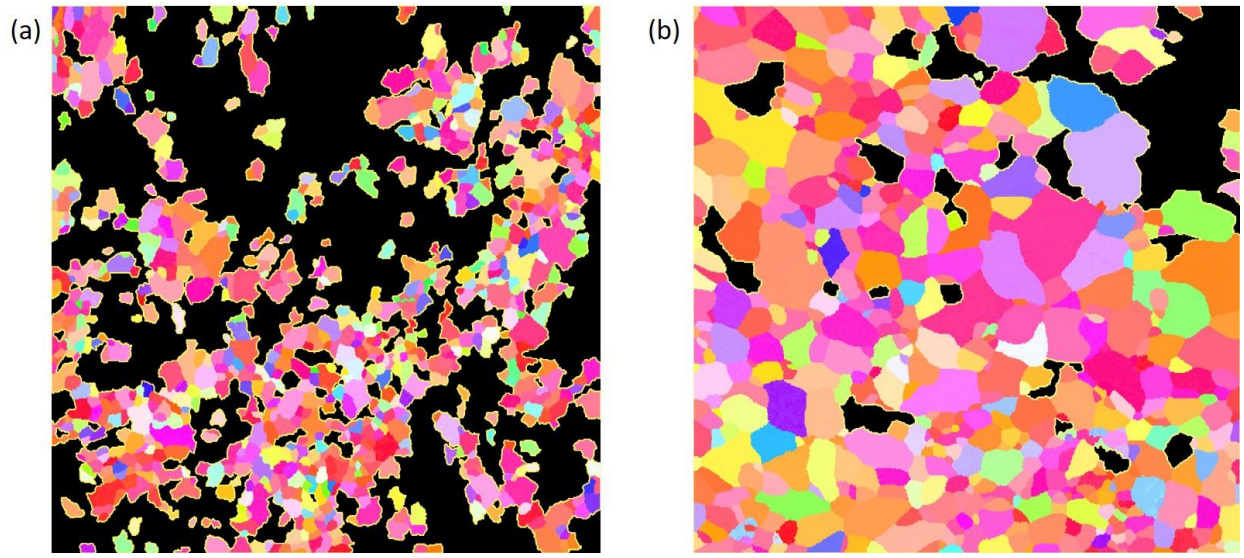

Figure 38. Examples of filtered EBSD images with recrystallized grains in color and deformed regions in black. Images are of partially recrystallized microstructures of Ti-7wt%Al. (a) 43% recrystallized, Sv=0.027, (b) 84% recrystallized, Sv=0.0098

The filtered images are then loaded into Image J software and the color threshold feature is used to differentiate the colored regions from the black regions. The perimeter of the colored or recrystallized regions is then measured because it is equivalent to the line length of all unimpinged grain boundaries separating recrystallized and unrecrystallized regions. This total length, L, is divided by the area of the entire image, A, to give the value of S_v:

$$S_v = L/A \tag{5}$$

This technique was compared to line intercept technique by performing both methods on multiple images and the results were found to be similar therefore validating the proposed technique.

4.2.3 Experimental Results

The S_V values determined for both Ti-4wt%Al and Ti-7wt%Al after being compressed and subsequently annealed at 800°C for various times are shown in Figure 39. These results were fit using a least squares fitting procedure to the form [13]:

$$S_V = CX^p(1 - X) \quad (6)$$

where C and p are constants, and the best fit curves are plotted as dashed lines. For both alloys, these plots exhibit the expected asymmetric bell curve shape and both reach a peak S_V value between 30% and 40% recrystallized, corresponding to results seen in literature [13], [14]. The peak S_V values occurring at less than 50% recrystallized indicates that there is an inhomogeneous distribution of nuclei at the start of static recrystallization in both alloys, explaining the low Avrami exponents of approximately one. This conclusion will be validated using phase field simulations in the following section. The peak values of S_V measured in this work are in the range of 0.02-0.03 μm^{-1}. This is somewhat lower than those observed in other studies [13], [14], [16] which tended to vary from 0.03 to 0.08 as seen in Figure 37, for example. This may be explained by the density of nuclei in the starting material since a higher nuclei density will lead to higher S_V magnitudes. A higher number of recrystallized grains creates a higher total grain boundary area per unit volume and therefore a higher magnitude of S_V. Vandermeer et al. [13] reports the initial nuclei density for their hot deformed and cold deformed aluminum alloys as $1.8x10^4$ mm^{-3} and $2.8x10^4$ mm^{-3}, respectively. The estimated initial nuclei density based on the fully recrystallized grain size of the titanium alloys in this is work (calculated in Chapter 3) is $1.5x10^4$ mm^{-3}. The significantly higher nuclei density explains the much higher S_V values for the cold deformed aluminum alloy, which peak around 0.08 μm^{-1}. The nuclei density for the hot deformed aluminum is very similar though slightly higher than that of the titanium alloys. The S_V values for the hot deformed aluminum peak at around 0.03 μm^{-1} while the peak values of S_V for the titanium alloys are around 0.02 μm^{-1}, corresponding perfectly to the trends in the nuclei density.

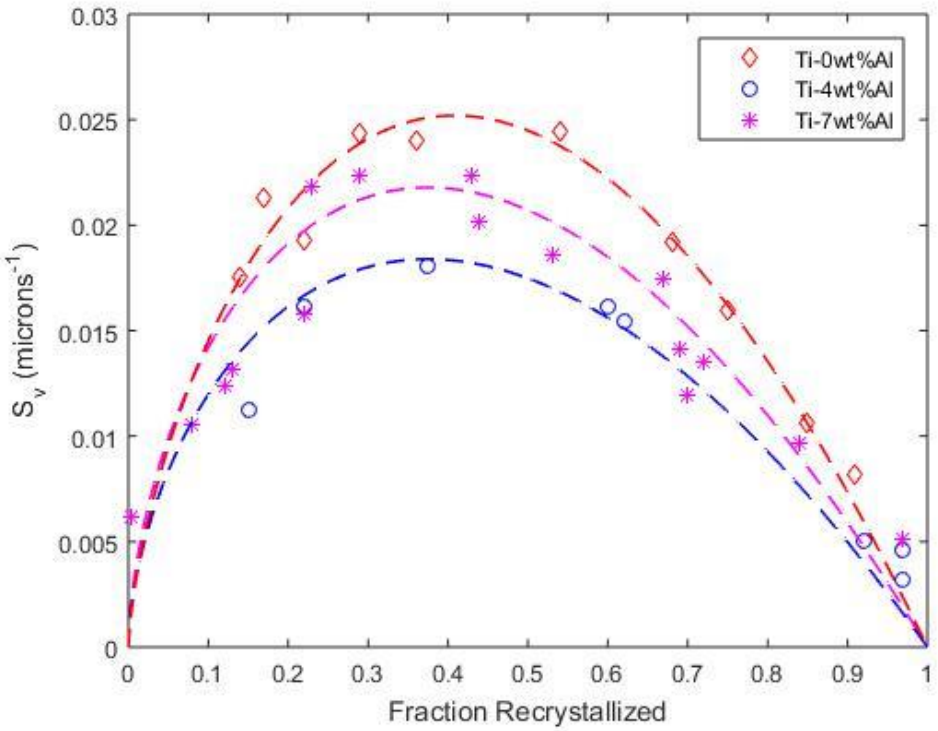

Figure 39. Sv vs. % Recrystallized results for Ti-0wt%Al at 600°C and Ti-4wt%Al and Ti-7wt%Al at 800°C

4.3 Phase Field Modeling

4.3.1 Model overview

A three-dimensional phase field simulation for recrystallization has been developed by Dr. Susan Gentry and Dr. Katsuyo Thornton at the University of Michigan [17], [18]. In these simulations, the microstructural evolution is driven by the total free energy of the system. The total free energy is described in terms of order parameters that are assigned to the grains that make up the microstructure. Each grain is assigned a unique order parameter that is evolved separately from other order parameters. The initial microstructure consists of equiaxed grains with an average grain size of 53µm that are randomly assigned a stored dislocation density within ±25% of an average value. The microstructure was then seeded with round nuclei with a diameter of 15µm based on the probability of forming a nucleus at a given point. This probability is determined based on the gradients of the order parameters, which is lowest in

the middle of a grain, high at a grain boundary, and highest at a triple point. Random points in the microstructure are selected and the nucleation probability at each point is compared to a randomly generated number between zero and one. If the random number is less than the nucleation probability, then a nucleus is seeded and this is repeated until the desired number of nuclei have been created. An example of an initial 3D microstructure with a random distribution of stored energy and nuclei is shown in Figure 40. Each new nucleus is also assigned a unique order parameter and the microstructure is then evolved by Allen-Cahn dynamics. The fraction recrystallized and time are tracked throughout the recrystallization process and can be plotted to quantify the kinetics. A correction time for nuclei growth is also included by adding the time needed for a nucleus of critical nuclei size to grow to the nuclei seed size. The model was parameterized based on literature values for CP titanium and experimental results from this work for Ti-0wt%Al at 800°C. The model was then run until a fully recrystallized microstructure was reached. The Avrami constant calculated from the resulting fraction recrystallized vs. time plot was equal to 3.1, corresponding to that of the JMAK model for site saturated nucleation.

This work was then continued by Dr. Arunabha Roy who investigated the effects of an inhomogeneous distribution of stored energy and nucleation.

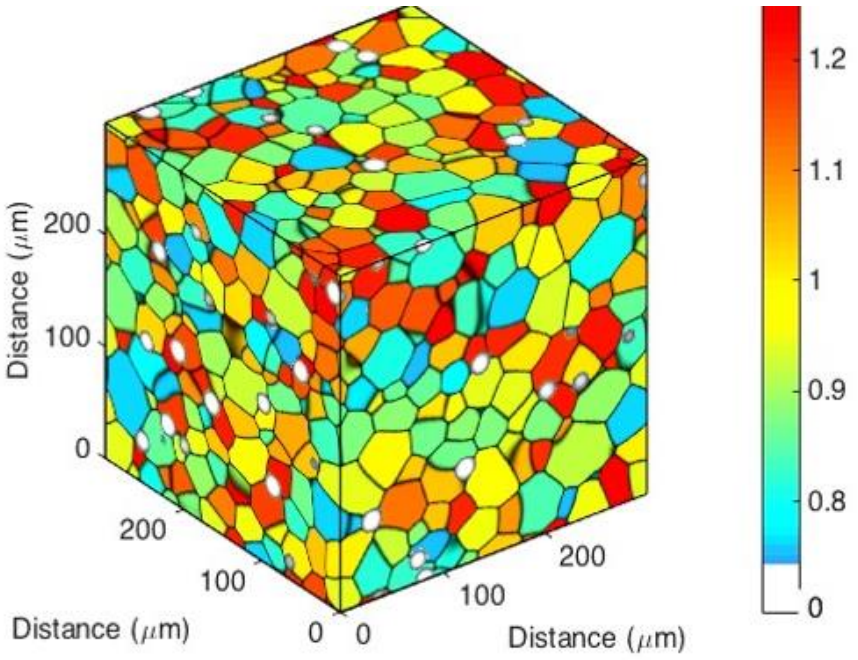

Figure 40. Initial 3D phase field model microstructure with a random distribution of stored energy and nuclei (model results by Susan Gentry)

4.3.2 Inhomogeneous Stored Energy in Phase Field Model

To provide a more realistic distribution of stored energy a crystal plasticity finite element (CPFE) model developed by Dr. Veera Sundararaghavan's group at the University of Michigan was used as input for the spatial distribution of stored energy. These results were then mapped to the phase field simulation domain to investigate the influence of non-random deformation on the spatial distribution of recrystallization and the Avrami exponent. As the starting microstructure for the CPFE simulation, a representative volume element with equiaxed grain size and shape that matched the experimentally measured texture (defined by the orientation distribution function) was used. The CPFE model was run in order to simulate the experimental compression step and to determine a realistic distribution of dislocation density. This information was then used to assign the grains of the initial phase field model microstructure with stored energy values. The microstructure was also seeded with a random distribution of nuclei and run again to simulate the recrystallization of Ti-0wt%Al at 800°C as depicted in Figure 41. The calculated Avrami exponent from the resulting kinetics is equal to

2.68, which is slightly lower than the previous result of 3.1 for random stored energy. While the inhomogeneous distribution of stored energy that was depicted by these linked simulations does lower the Avrami exponent, it is not significant enough to explain the values of about one that are seen experimentally. Therefore, the effect of non-random nuclei distribution was investigated.

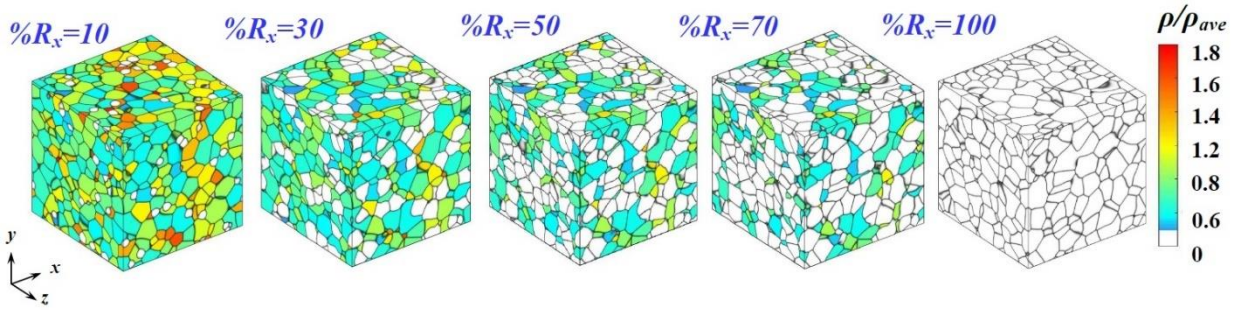

Figure 41. Phase field simulation of recrystallization for Ti-0wt%Al at 800C using CPFE stored energy distribution and a random nuclei distribution (model results by Arunabha Roy)

4.3.3 Nuclei Clustering in Phase Field Model

In order to realistically simulate how nuclei are clustered in the titanium alloys being studied, information from partially recrystallized EBSD scans was used. As seen in Figure 42, some partially recrystallized samples contained bands of clustered recrystallized grains indicating there were initially bands of clustered nuclei. It is simpler to input a single monolayer of seeded nuclei into the initial phase field microstructure (compared with random regions of clustered nuclei) and these banded regions were selected as the input for phase field simulations.

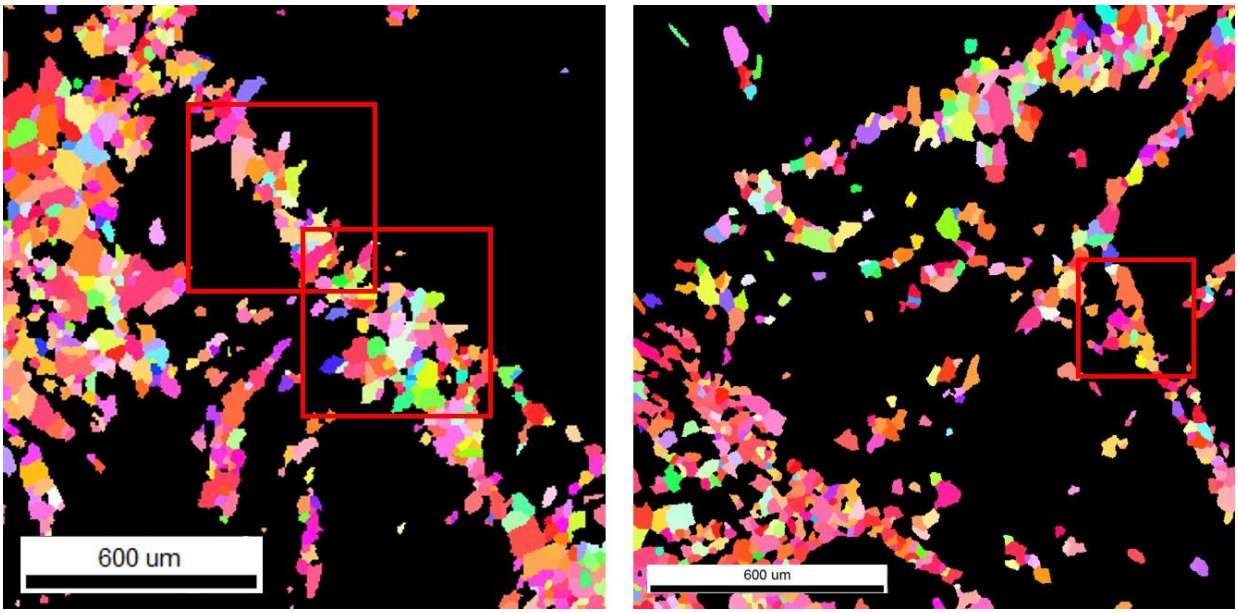

Figure 42. Partitioned EBSD scans of two different partially recrystallized Ti-4wt%Al samples. The indicated areas were used to measure nuclei density along clustered bands.

The density of grains in each of the indicated areas in Figure 42 was measured by dividing the number of grains by the area of the region. The average of these three regions was used in order to take into account sample variability. A banded zone of a thickness that is 1/16 that of the simulated microstructure was seeded with 60 nuclei. The simulation was conducted throughout the process of recrystallization as depicted in Figure 43. The results were fit to the JMAK relationship and compared to the randomly distributed nuclei simulation shown in Figure 6. A comparison of the simulated recrystallization curves is provided in Figure 44. By altering the distribution of nuclei to be non-random, the Avrami exponent decreases from 2.68 to 1.21, which more closely matches the value of 1.0 that was measured experimentally. Therefore, the combination of the stored energy distribution generated from the CPFE simulation and the clustered nuclei more accurately simulates the experimentally determined recrystallization kinetics. In these simulations, it is clear that, compared with the assumptions regarding the distribution of stored energy, the assumptions on the distributions of nuclei are more important for accurately capturing the experimental observations.

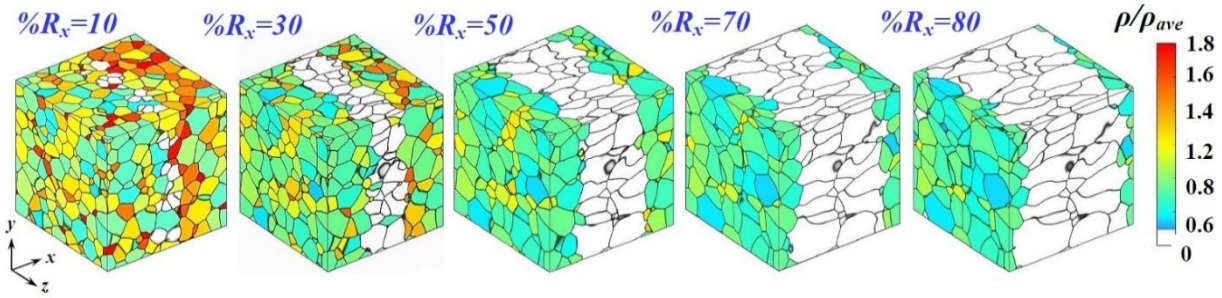

Figure 43. Progression of the phase field model with clustered nuclei (model results by Arunabha Roy)

By clustering the nuclei in a planar region, the growth of the recrystallized grains is affected in two of the three dimensions early in the recrystallization process. Before impingement, uniform growth occurs in all three directions as predicted by JMAK. However, in two of the growth dimensions, preferential impingement occurs early in the recrystallization process. The growth rate of the recrystallized grains therefore slows down and is no longer constant in those directions. This change in growth rate is what leads to a decrease in Avrami exponent and therefore deviation from the original JMAK model. In the third growth dimension that is still free and unaffected by the clustering, impingement will eventually occur with the grains from a neighboring cluster (represented by periodic boundary conditions in the phase field model).

The free surface fraction, S_V, was also calculated from the simulated microstructures for both the random and clustered nuclei cases. As seen in Figure 45, the plot of S_V vs. percent recrystallized for the random nuclei case is a symmetric bell curve that peaks at 50% recrystallized. This is consistent with the theoretical JMAK relationship for site saturated, random nucleation. The plot for the clustered nuclei case is asymmetric and peaks between a recrystallization fraction between 20% and 30%. These simulations, validates the theory that clustering of nuclei should cause the peak to be below 50%.

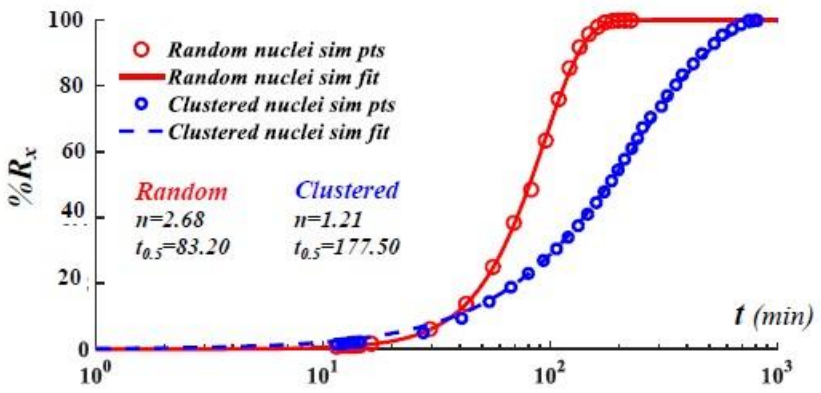

Figure 44. Percent recrystallized vs. time phase field model results for both random and clustered nuclei distributions (model results by Arunabha Roy)

This peak value is slightly lower than that of the experimental results, which peak between 30% and 40%. This may be due to the inherent variability that exists in the nucleation distribution of the real material. Nuclei do not always cluster in repeating bands in the actual material as they are simulated to in the phase field model. Some regions of the samples may have a nucleation distribution that is more spread out or random while other regions may have more globular clustering. The peak value of S_V in the model is approximately 0.035 and is slightly higher than the peak experimental value of approximately 0.023. This again can be explained by variability throughout the material.

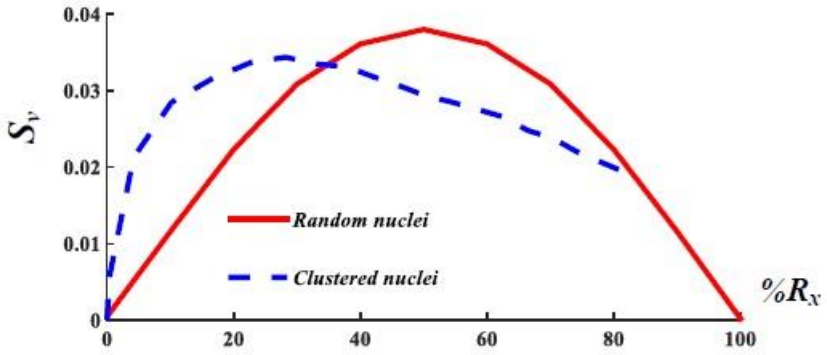

Figure 45. S_V vs. Percent recrystallized results from phase field model simulations for both random and clustered nuclei cases (model results by Arunabha Roy)

The magnitude of S_V increases with increasing nuclei density. Therefore, the lower experimental values are due to regions throughout the samples that have a lower nuclei density than what was used to describe the initial microstructure used in the phase field simulation. Despite these variations, the phase field simulation is able to correctly capture the experimental recrystallization kinetics based on the matching Avrami exponents. The phase field model therefore confirms our hypothesis that these inhomogeneities are the cause of the observed experimental Avrami exponent having a value close to one.

4.4 Conclusions

- A new analytical technique for measuring the free surface fraction, S_V, is presented.
- The S_V values for both Ti-4wt%Al and Ti-7wt%Al peak below 50% recrystallization. This indicates the likely occurrence of an inhomogeneous distribution of nuclei. This reduced peak value of S_V is due to the impingement of clustered nuclei that occurring at shorter times and earlier in the crystallization process than that of randomly distributed nuclei.
- The inhomogeneous distribution of nuclei creates a non-constant growth rate during recrystallization because of grain impingement. This produces an Avrami exponent that is significantly lower than that for a random distribution of nuclei.
- Changing the distribution of stored energy from random to non-random in the phase field simulation decreased the Avrami exponent slightly. Therefore, while an inhomogeneous distribution of stored energy may alter the growth rate, it is not sufficient to explain the low experimental Avrami exponents
- Clustering the nuclei into a planar region of the phase field simulation lowered the Avrami exponent to 1.2, matching the experimental results. The combination of inhomogeneous distributions of nuclei and inhomogeneous stored energy accurately simulate the experimentally observed recrystallization kinetics as captured by the Avrami exponent. Of these two factors the assumptions on the nucleation distribution is a much more significant factor.

- The clustering of nuclei in the phase field simulation caused the peak of the S_V curve to occur below 50% compared to right at 50% for the random distribution of nuclei. This validates the hypothesis that the experimentally determined evolution of S_V results from inhomogeneous nucleation.

4.5 References

[1] W. Johnson and R. Mehl, “Reaction kinetics in processes of nucleation and growth,” *Trans. Am. Inst. Min. Metall. Eng.*, vol. 135, pp. 416–442, 1939.

[2] M. Avrami, “Kinetics of Phase Change . I General Theory,” *J. Chem. Phys.*, vol. 7, no. 12, pp. 1103–1112, 1939.

[3] H. Wu, L. Du, Z. Ai, and X. Liu, “Static Recrystallization and Precipitation Behavior of a Weathering Steel Microalloyed with Vanadium,” *J. Mater. Sci. Technol.*, vol. 29, no. 12, pp. 1197–1203, 2013.

[4] L. Llanos, B. Pereda, B. López, and J. M. Rodriguez-ibabe, “Modelling of Static Recrystallization Behavior of High Manganese Austenitic Steels with Different Alloying Contents,” *ISIJ Int.*, vol. 56, no. 6, pp. 1038–1047, 2016.

[5] N. Hansen, T. Leffers, and J. K. Kjems, “Recrystallization Kinetics in Copper Investigated by In Situ Texture Measurements by Neutron Diffraction,” *Acta Metall.*, vol. 29, pp. 1523–1533, 1981.

[6] P. Gordon and R. Vandermeer, “The mechanism of boundary migration in recrystallization,” *Trans. Metall. Soc. AIME*, vol. 224, pp. 917–929, 1962.

[7] A. G. Beer and M. R. Barnett, “The post-deformation recrystallization behaviour of magnesium alloy Mg–3Al–1Zn,” *Scr. Mater.*, vol. 61, no. 12, pp. 1097–1100, Dec. 2009.

[8] Y. B. Chun and S. K. Hwang, “Static recrystallization of warm-rolled pure Ti influenced by microstructural inhomogeneity,” *Acta Mater.*, vol. 56, no. 3, pp. 369–379, Feb. 2008.

[9] L. Cheng, H. Chang, B. Tang, H. Kou, and J. Li, “Deformation and dynamic recrystallization behavior of a high Nb containing TiAl alloy,” *J. Alloys Compd.*, vol. 552, pp. 363–369, Mar. 2013.

[10] L. Cheng, H. Chang, B. Tang, H. Kou, and J. Li, “Characteristics of metadynamic recrystallization of a high Nb containing TiAl alloy,” *Mater. Lett.*, vol. 92, pp. 430–432, Feb. 2013.

[11] A. Trump and J. Allison, “The influence of aluminum content and annealing temperature on static recrystallization in α-titanium alloys,” 2016.

[12] R. Vandermeer, R. Masumura, and B. Rath, “Microstructural Paths of Shape-Preserved Nucleation and Growth Transformations,” *Acta Mater.*, vol. 39, no. 3, pp. 383–389, 1991.

[13] R. A. Vandermeer and D. J. Jensen, “Recrystallization in hot vs cold deformed commercial aluminum : a microstructure path comparison,” *Acta Mater.*, vol. 51, pp. 3005–3018, 2003.

[14] D. J. Jensen, “Orientation Aspects of Growth during Recrystallization,” Technical University of Denmark, 1997.

[15] R. Vandermeer and B. Rath, “Modeling Recrystallization Kinetics in a Deformed Iron Single Crystal,” *Metall. Trans. A*, vol. 20, no. 3, pp. 391–401, 1989.

[16] R. B. Godiksen, “Simulations of Recrystallization in Metals,” Roskilde University, 2007.

[17] S. P. Gentry and K. Thornton, “Simulating recrystallization in titanium using the phase field method,” in *IOP Conference Series: Materials Science and Engineering*, 2015, vol. 89, no. 012024.

[18] S. P. Gentry and K. Thornton, “Simulating static recrystallization and grain growth of deformed microstructures using the Phase-Field Method,” 2015, working paper.

Chapter 5. The Effect of Annealing Temperature and Aluminum Concentration on Grain Growth Kinetics

5.1 Introduction

The grain size of a material has a significant impact on the mechanical properties and an increased grain size often leads to unfavorable properties such as decreased strength and hardness. Therefore, it is important understand the grain growth kinetics in order to know how annealing will affect the mechanical properties. The grain growth kinetics and specifically how alloying elements affect the kinetics have been studied in various material systems [1]–[7] such as magnesium, aluminum, and steel. This topic has also been studied in titanium alloys [8]–[15]. However, the studies that have been done on the effects of alloying elements have mostly been on beta stabilizing elements such as Mo [14]. Therefore, the goals of this work are to quantify how aluminum, the most commonly used alpha stabilizing element, affects the grain growth kinetics and to understand the mechanisms behind this effect.

5.2 Materials and Experimental Procedure

5.2.1 Materials

The alloys studied in this work are single phase alpha binary Ti-Al alloys with varying Al concentrations (0wt%, 4wt%, and 7wt% Al). The composition and beta transus temperatures of these alloys are listed in Table 1. The ingots of these alloys were produced by TIMET Corp and were processed via vacuum arc remelting (VAR) to ensure composition homogeneity. The ingots were then hot forged at 93°C above their beta transus temperatures from 7.5” round to

4” square and air cooled. An optical image of the initial microstructure is seen in Figure 46. A lamellar microstructure was produced by cooling the alloys from the beta regime to the alpha regime.

Table 10. Chemical composition and beta transus temperatures of alloys studied

Alloy	**Chemical Composition**			**Beta transus temperature**
	Al (wt%)	**Fe (wt%)**	**O (wt%)**	
Ti-0wt%Al	0.005	0.008	0.086	1163K (890°C)
Ti-4wt%Al	3.85	0.013	0.096	1263K (990°C)
Ti-7wt%Al	6.92	0.016	0.087	1322K (1049°C)

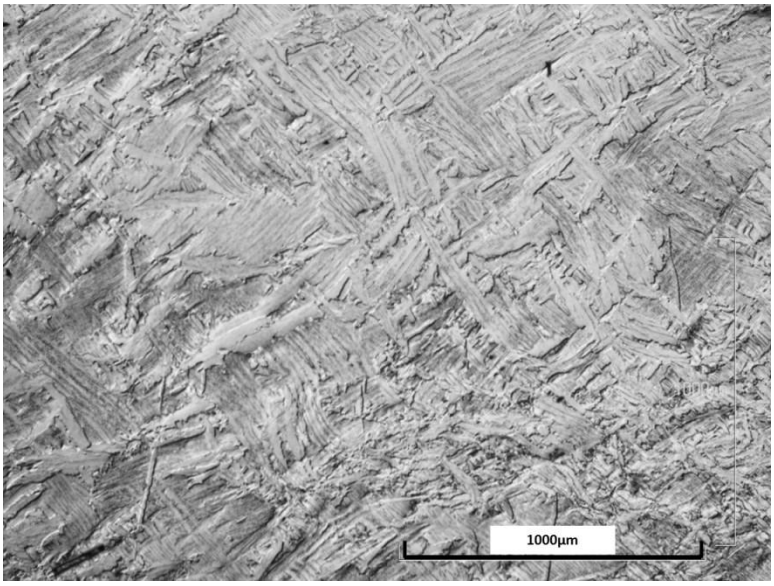

Figure 46. Optical micrograph of Ti-4wt%Al as beta forged microstructure

5.2.2 Recrystallization Heat Treatments

Due to the forging process, the microstructure of the as received materials was a distorted lamellar microstructure containing a significant amount of stored energy. This leads to two problems in studying the grain growth kinetics. The first is that there is no known initial grain size to compare to the final grain size. Also, upon heating, recrystallization can occur and the grain growth kinetics will not be isolated but rather compounded with the recrystallization

kinetics. Therefore, it was necessary to perform recrystallization heat treatments before beginning grain growth studies in order to produce an equiaxed and fully recrystallized microstructure. This was accomplished by first compressing cylindrical samples that were 9mm in height and 6mm in diameter to a 20% height reduction at room temperature. The purpose of this compression step is to increase the amount of stored energy in the material along with creating a more uniform distribution of stored energy in order to induce faster and more uniform recrystallization upon heating. The compression tests were performed using an Instron load frame equipped with a 100kN load cell and at a strain rate of 0.03 mm/min). The samples were then subsequently annealed at a given time and temperature in order to produce a fully recrystallized and equiaxed microstructure. The heat treatment times and temperatures for each alloy was selected based on previous recrystallization studies of these alloys [16]. The heat treatments used are 90 minutes at 600°C, 8 hours at 800°C, and 30 minutes at 950°C for Ti-0wt%Al, Ti-4wt%Al, and Ti-7wt%Al respectively and were performed in a ceramic tube furnace. All samples were immediately water quenched following annealing. EBSD scans of the resulting microstructures are seen in Figure 47, all of which have average grain sizes of approximately 40µm. Therefore, all subsequent grain growth tests begin with similar microstructures and average starting grain size for all three alloys.

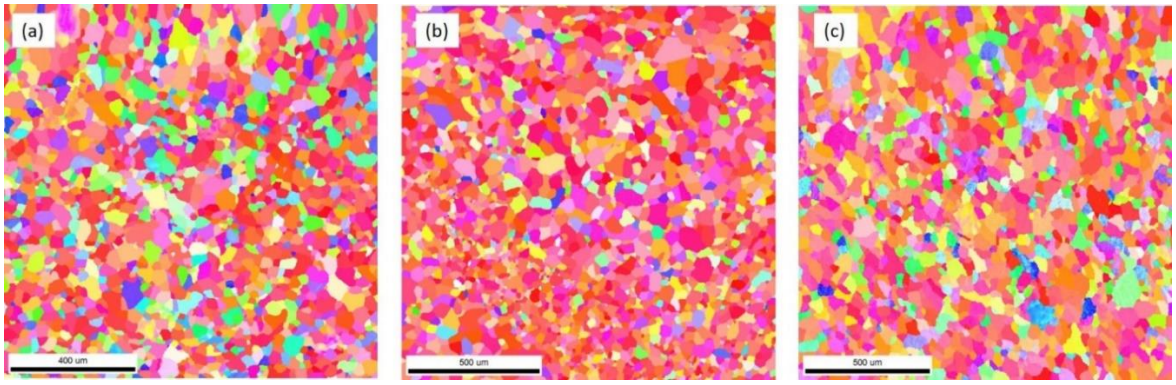

Figure 47. EBSD scans of (a) Ti-0wt%Al, (b) Ti-4wt%Al, and (c) Ti-7wt%Al after homogenization heat treatments of 600°C/90 minutes, 800°C/8 hours, and 950°C/30 minutes, respectively.

5.2.3 Grain Growth Heat Treatments and Grain Size Measurements

Following the recrystallization heat treatments, the samples were heat treated in a tube furnace for varying times and temperatures. All temperatures were below the beta transus

temperatures. Annealing was done at 700°C and 800°C for all three alloys and at 900°C for Ti-4wt%Al and Ti-7wt%Al. The samples were then water quenched, sectioned perpendicular to the compression axis at the center, mounted in epoxy, and prepared for imaging. The preparation steps include grinding using 800 grit SiC paper, polishing with a colloidal silica and hydrogen peroxide mixture and etching using Kroll's solution (4% hydrofluoric acid, 8% nitric acid, and the balance DI water) for approximately 45 seconds. Over etching could not be eliminated in the Ti-0wt%Al and the microstructures for this alloy were imaged using a Zeiss optical microscope with cross polarization. In all cases the average grain size was measured using the line intercept method (LIM) based on the ASTM standard for determining average grain size (E 112). The line intercept method was performed by drawing lines in varying directions across the image and counting the number of intersections each line makes with grain boundaries. The total length of the lines is divided by the total number of intersections to give the mean lineal intercept. Given the assumption of circular grains, the mean lineal intercept, l, can be related to the average grain area, A, as follows:

$$l = \left(\frac{\pi}{4}A\right)^{1/2} \tag{1}$$

and

$$A = \pi\left(\frac{D}{2}\right)^2 \tag{2}$$

where D is the average grain diameter. Although the grains are not perfectly circular, this assumption was verified by measuring the grain size of the same sample using both LIM and EBSD. This was done on multiple samples of all three alloys and very good agreement was seen between the two methods.

5.3 Results

5.3.1 Grain Growth Results

Figure 48 shows examples of some optical micrographs of both Ti-0wt%Al and Ti-4wt%Al throughout the grain growth process at 800°C. Polarized light alone is used to image the grains in Ti-0Al while etching of the grain boundaries combined with polarized light is used

for Ti-4Al. Both methods allow for the imaging of individual grains. The equiaxed microstructure that is created during the recrystallization heat treatments remains during grain growth. It is clear that the grain size increases with increasing annealing time. Although both alloys were annealed at the same temperature, the Ti-0Al grain size is significantly larger than that of Ti-4Al. The grain size results for all three alloys can be seen in Figure 49 where the average grain size is plotted versus annealing time (following the recrystallization heat treatment). These plots show the expected classic grain growth kinetics trend with an initial steep slope where grain growth is occurring rapidly followed by a decreasing slope that eventually approaches steady state. This decrease in growth rate can be explained by the increase in grain size leading to a decrease in the total grain boundary area per unit volume. A lower grain boundary area per unit volume means a lower grain boundary interfacial energy per unit volume and therefore a lower driving force.

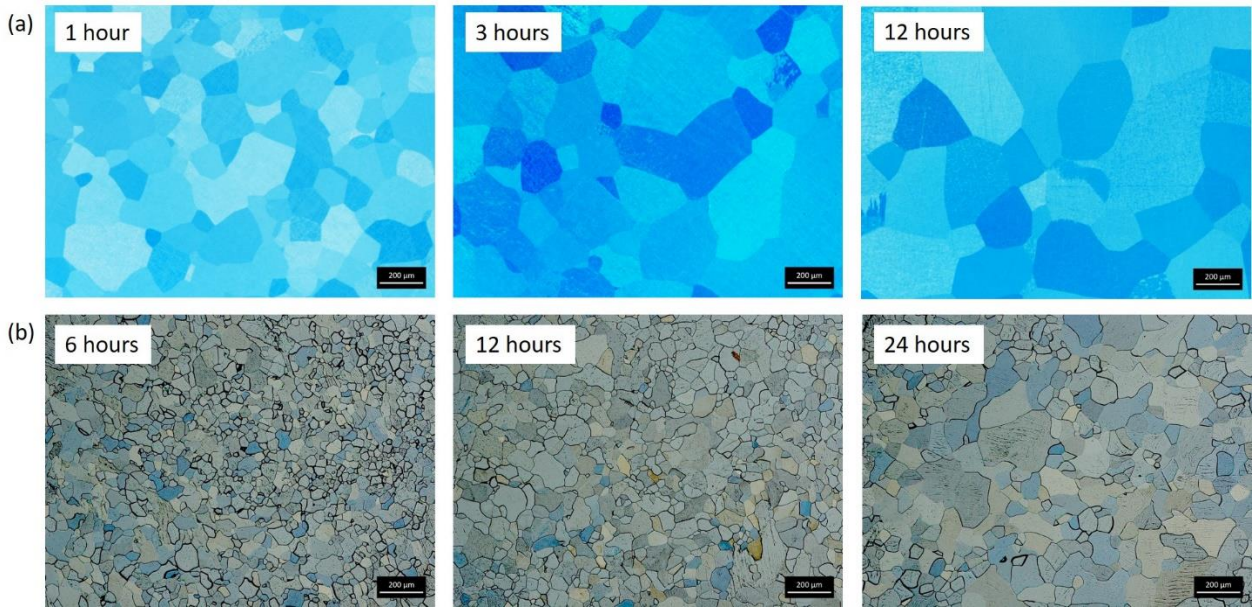

Figure 48. Examples of optical micrographs for (a) Ti-0wt%Al and (b) Ti-4wt%Al after grain growth heat treatments at 800C for varying times.

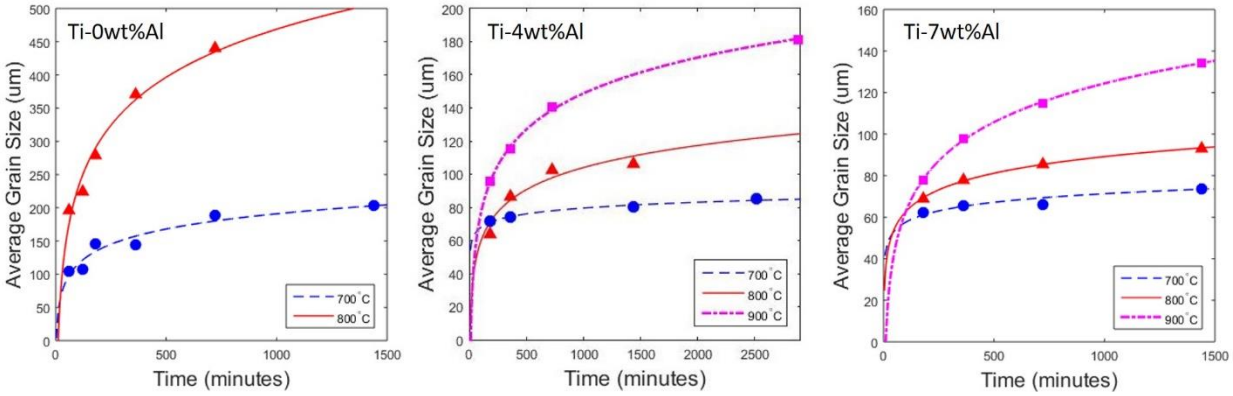

Figure 49. Average Grain Size vs. Annealing Time plots showing grain growth kinetics results for the three alloys at various annealing temperatures

Figure 49 also clearly shows more rapid grain growth kinetics with increasing annealing temperature for all three alloys. This can be explained by the fact that grain growth is a thermally activated, diffusion controlled process and the diffusion of atoms across the grain boundaries that leads to grain boundary motion is able to occur more rapidly at higher temperatures. The resulting grain growth kinetics shown in Figure 49 can be quantified by the following equation:

$$D - D_0 = kt^n \tag{3}$$

where D is the average grain size at a given annealing time, D_0 is the initial grain size, t is annealing time, n is the grain growth exponent and k is a constant. The grain growth exponent can be determined by linearizing Eq. 3 by taking the logarithm of both sides of the equation as follows:

$$ln(D - D_0) = n\, ln(t) + \ln(k) \tag{4}$$

Therefore, the slope of a plot of $\ln(D-D_0)$ vs. ln(t) gives the value of n. Linearized plots of all the results from Figure 49 can be seen in Figure 50 with the resulting grain growth exponents listed in Table 11. Grain growth was observed to have an increasing n value with increasing temperature for all three alloys.

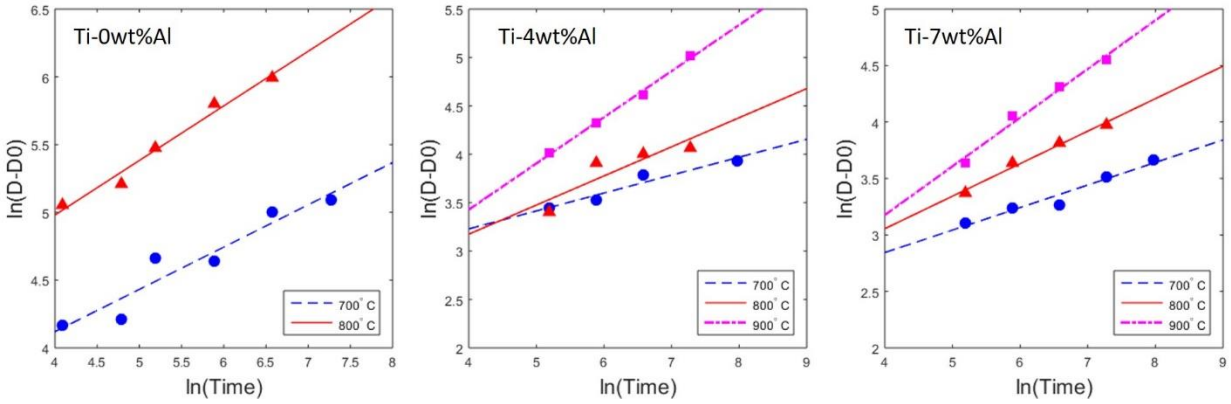

Figure 50. Linear plots used to calculate the grain growth exponents for all three alloys at various annealing temperatures

Table 11. Grain growth exponent, n, values

	700°C	**800°C**	**900°C**
Ti-0wt%Al	0.31	0.40	-
Ti-4wt%Al	0.20	0.30	0.48
Ti-7wt%Al	0.20	0.29	0.43

Eq. 3 was originally developed by Burke and Turnbull [17] who made a number of assumptions in deriving this relationship. Two key assumptions are that the driving force for grain growth is due only to grain boundary curvature and the boundary velocity is proportional to that driving force [18]. The derivation of this relationship gives an n value of 0.5 for an ideal material, however very few experimental results actually observe this value. Factors such as solute drag and texture are however not accounted for in this relationship and these factors may lead to lower n values. For pure titanium an n value of 0.40 is observed at 800C. This value is close to the ideal value of 0.5. Gil et al. [13] studied the grain growth kinetics of CP titanium and measured a grain growth exponent of 0.30 and 0.50 for 700°C and 800°C respectively, which is consistent with the results in this work. The deviation from the ideal value is potentially related to the weak basal texture exhibited by this condition, although the trace amounts of solutes as listed in Table 10 may also play a role. In conditions with a non-random texture, grain

boundaries generally have lower misorientation angles and therefore lower grain boundary energies. This can decrease the overall driving force for grain growth.

Table 11 also shows that the grain growth exponent decreases with increasing aluminum concentration, especially between Ti-0Al and Ti-4Al. This trend can be clearly seen in Figure 51 with Ti-0Al having the most rapid grain growth and largest average grain size at long annealing times. This trend has been seen in other grain growth studies on solute effects in titanium with beta stabilizing elements such as Mo [14] and Pd [13]. This effect is generally attributed to solute drag that causes solute atoms slow down the migration of grain boundaries. Grain growth is a diffusion controlled process and occurs when atoms diffuse across a grain boundary causing that grain boundary to migrate. Therefore, when the diffusion of the solute atoms across a grain boundary is slower than that of the bulk atoms, the addition of solute atoms slows the kinetics of the grain growth process. The results in Figure 51 suggest that the diffusion of aluminum atoms across grain boundaries is slower than that of the bulk alpha titanium atoms.

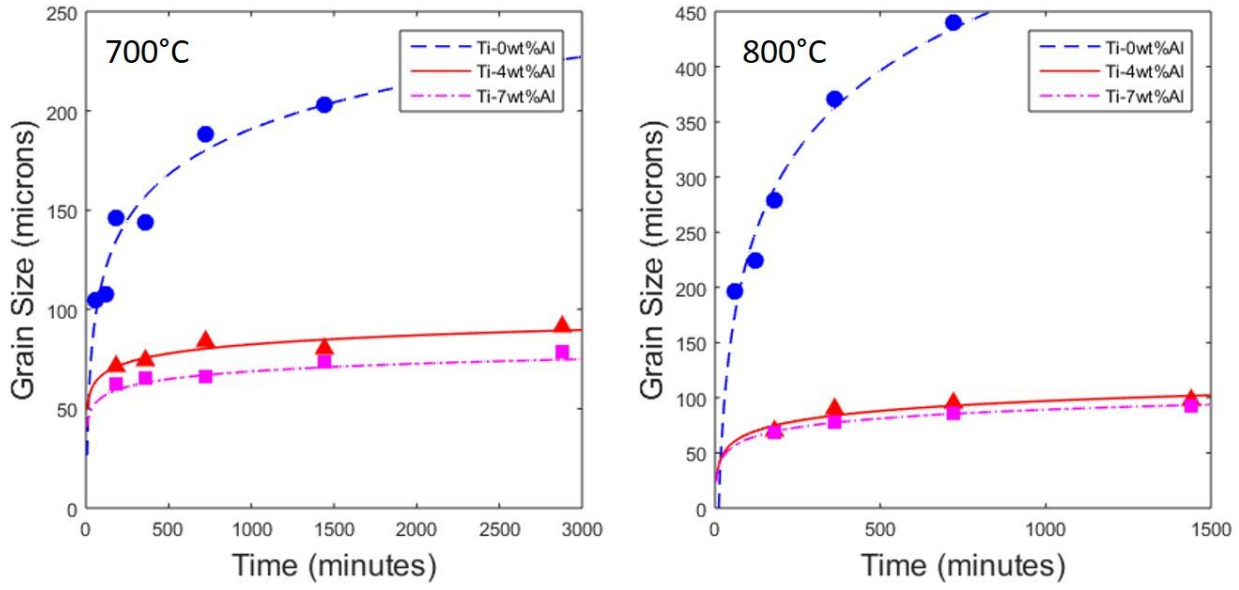

Figure 51. Comparison of grain growth results between the three alloys at both 700C and 800C

5.3.2 Grain boundary mobility

As discussed in Section 3.2, the addition of solute atoms slows the migration of the grain boundaries during grain growth. Therefore, it is of interest to study to relationship between the amount of aluminum added to titanium and the grain boundary mobility. The grain boundary mobility, M, is related to the grain boundary velocity, V, by the common relationship:

$$V = MP \tag{5}$$

where P is the driving force for grain growth. For curvature driven grain growth, the driving force is defined as:

$$P = \frac{\alpha \gamma_b}{R} \tag{6}$$

where α is a geometric constant usually assumed to be 2, γ_b is the grain boundary energy, and R is the average grain radius. Combining Eqs 5 and 6, the grain boundary velocity can be defined as:

$$\frac{\mathrm{dR}}{\mathrm{dt}} = \frac{\mathrm{M}\alpha\gamma_\mathrm{b}}{\mathrm{R}} \tag{7}$$

Rearranging this gives Eq 7b, which can be used to determine the mobility, M.

$$M = \frac{dR/_{dt}}{\alpha \gamma_b * R} \tag{7b}$$

The grain boundary energy for this work is set to 0.7 J/m^2, which is an approximate value for high angle grain boundaries in titanium [19]. The grain boundary velocity can then be determined as a function of time by taking the derivative of the best fit lines from the experimental data in Figure 51 and the mobility can be determined using Eq 7b. The calculated grain boundary mobility is plotted with respect to aluminum concentration for 700°C in Figure 52. It is clear that there is a significant decrease in mobility between 0wt% and 4wt%. This result corresponds well with the results plotted in Figure 51. The trend in mobility can be represented by the model for solute drag developed by Cahn [20], as shown in Figure 52.

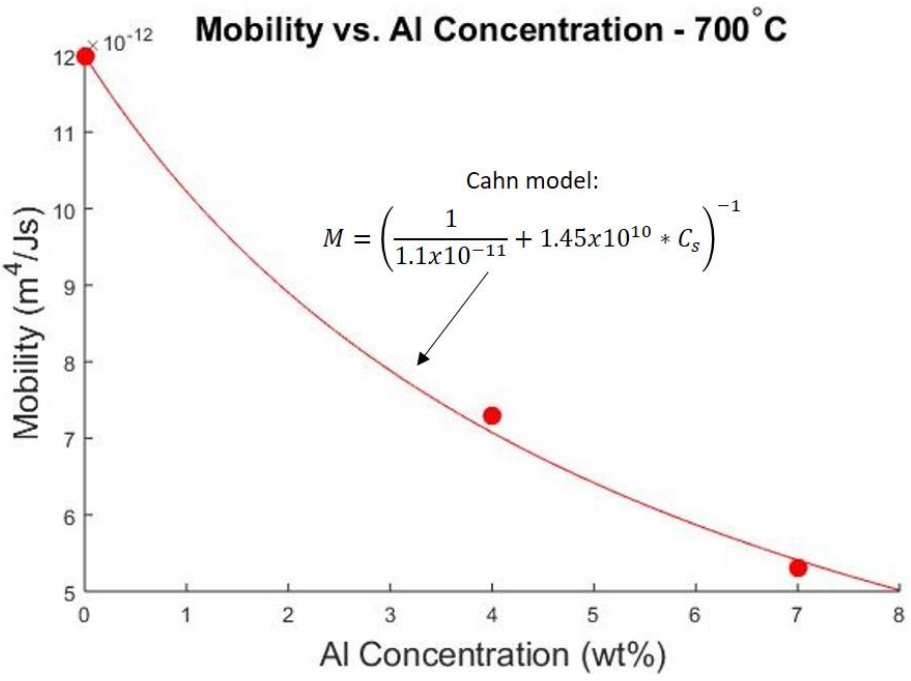

Figure 52. Calculated grain boundary mobility vs. Al concentration results for grain growth at 700C fit to the Cahn model for solute drag (solid line)

In Figure 53 the inverse mobility is plotted against aluminum concentration at both 700°C and 800°C. These results show that there is a linear relationship between the inverse mobility and aluminum concentration. This results corresponds to the relationship predicted by the CLS (Cahn, Lücke, and Stüwe) model for solute drag [20], [21]:

$$M_s = \left(\frac{1}{M_{INT}} + \alpha C_s\right)^{-1} \quad (8)$$

where C_s is the solute concentration, M_{INT} is the intrinsic mobility or the mobility in the solute free material, and α is a constant. A similar relationship was also developed by Gordon and Vandermeer [22] as well. There are also multiple examples in literature where this relationship is seen both from experiments and computational models. Huang and Humphreys [23] observed a linear relationship between inverse mobility and Mg concentration in binary Al-Mg alloys at concentrations of 1% and less. Sun et al. [24] used atomistic simulations to study the effects of solutes on grain boundary motion. Their results showed a linear decrease in the log

of grain boundary mobility with an increase in the log of number of solute atoms for both Al-Ni and Al-Pb systems.

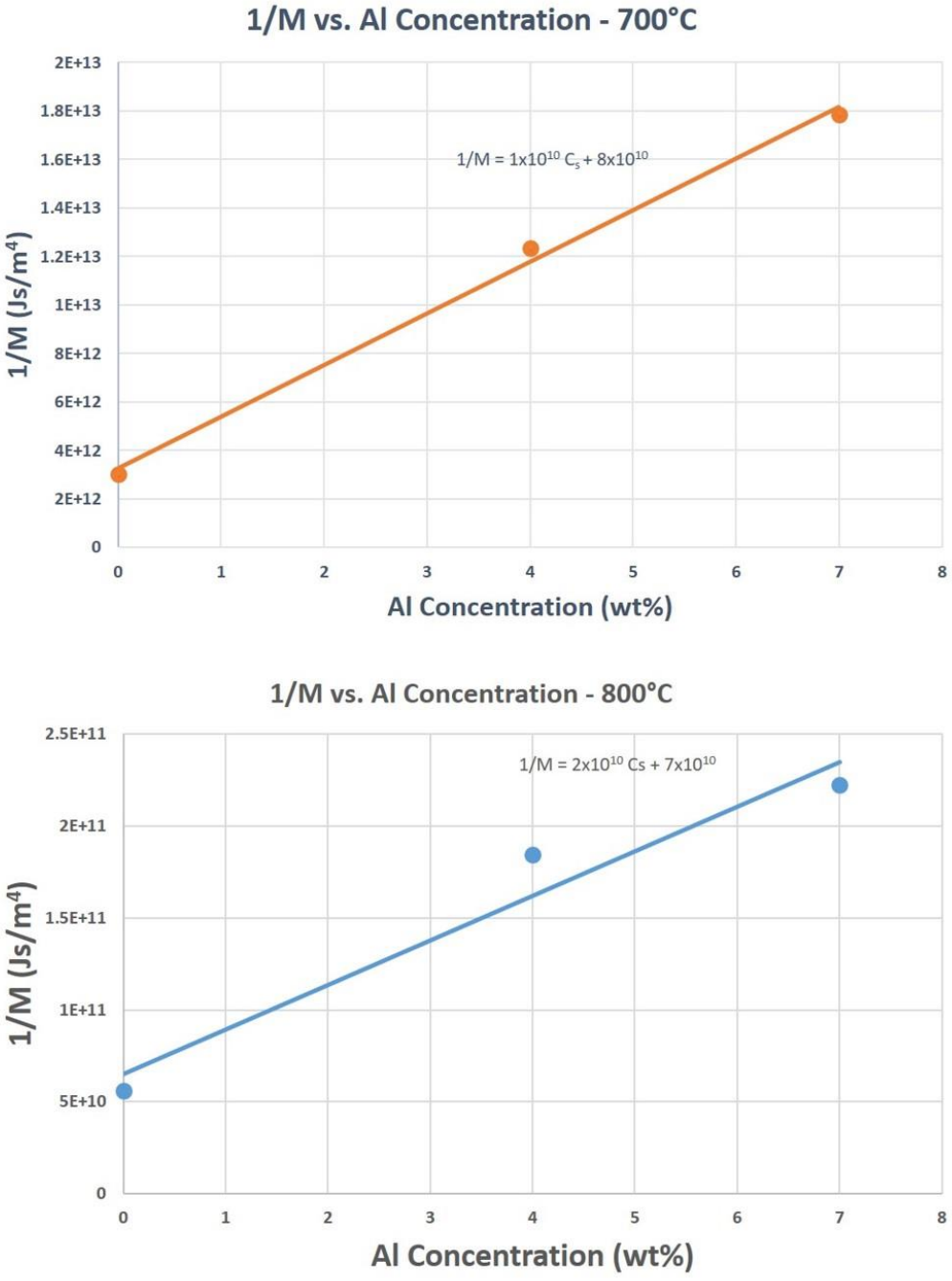

Figure 53. Inverse grain boundary mobility vs. aluminum concentration for grain growth at 700°C and 800°C (the solid lines represent linear fits to the data points with the corresponding equations listed above each line)

5.4 Discussion

The retardation of grain growth kinetics with increasing solute concentration is generally attributed to the solute drag effect. The majority of research investigating this decrease in grain growth kinetics due to solutes has explained this phenomenon by assuming that solutes segregate at grain boundaries and thus retard the growth by solute drag. However solute segregation has rarely been confirmed experimentally. The limited cases where segregation has been observed via microscopy have been in alloys with dilute solute concentrations [25]–[28].

In principal, the drag effect that segregated atoms have on grain boundaries during grain growth can be explained both by kinetics and thermodynamics. The kinetic effect is based on the difference in diffusivities of the solute atoms compared with the matrix (base) atoms. The argument is that If the solute atoms that are sitting at the grain boundary have a slower diffusivity in the matrix material than the solvent atoms do, then the grain boundary must drag those solute atoms along, slowing down the mobility of the boundary. The thermodynamic effect is based on the decrease in grain boundary energy due to solute atoms segregated at the grain boundary and lowers the overall driving force for grain growth. Based on both the kinetic and thermodynamic effects of solute segregation, the higher the concentration of solute atoms at the grain boundaries, the stronger the solute drag effect will be on the grain growth kinetics. Therefore, given the significant retardation in grain growth kinetics with increasing aluminum concentration seen in this work, a significant amount of aluminum segregation would be expected to be seen at the grain boundaries. Scanning transmission electron microscopy (STEM) combined with energy dispersive spectroscopy (EDS) mapping was performed at a grain boundary of a Ti-7wt%Al sample by Peng-Wei Chu. However, as seen in Figure 54, no obvious aluminum segregation was observed. In order to be certain that no segregation was occurring, higher magnification STEM and EDS was performed by Qianying Shi (Figure 55), but again no segregation was observed. This same result was also seen in Ti-4wt%Al. In order to understand this results, it is necessary to analyze what determines whether or not segregation will occur.

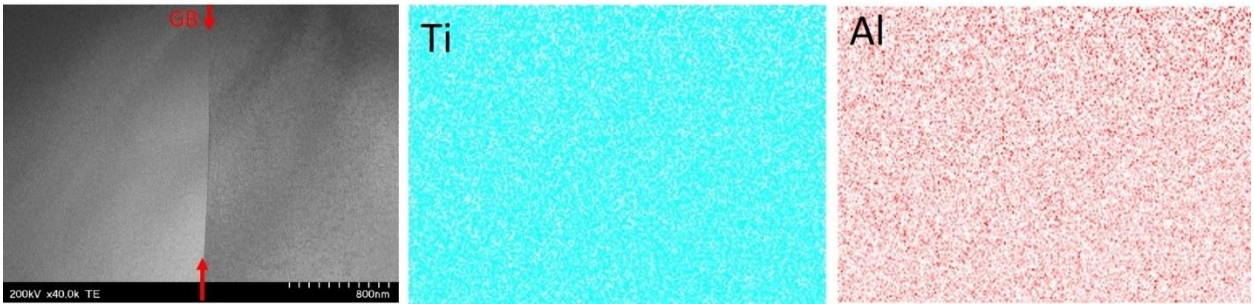

Figure 54. STEM and EDS maps at a grain boundary in a recrystallized Ti-7wt%Al sample (imaging performed by Peng-Wei Chu)

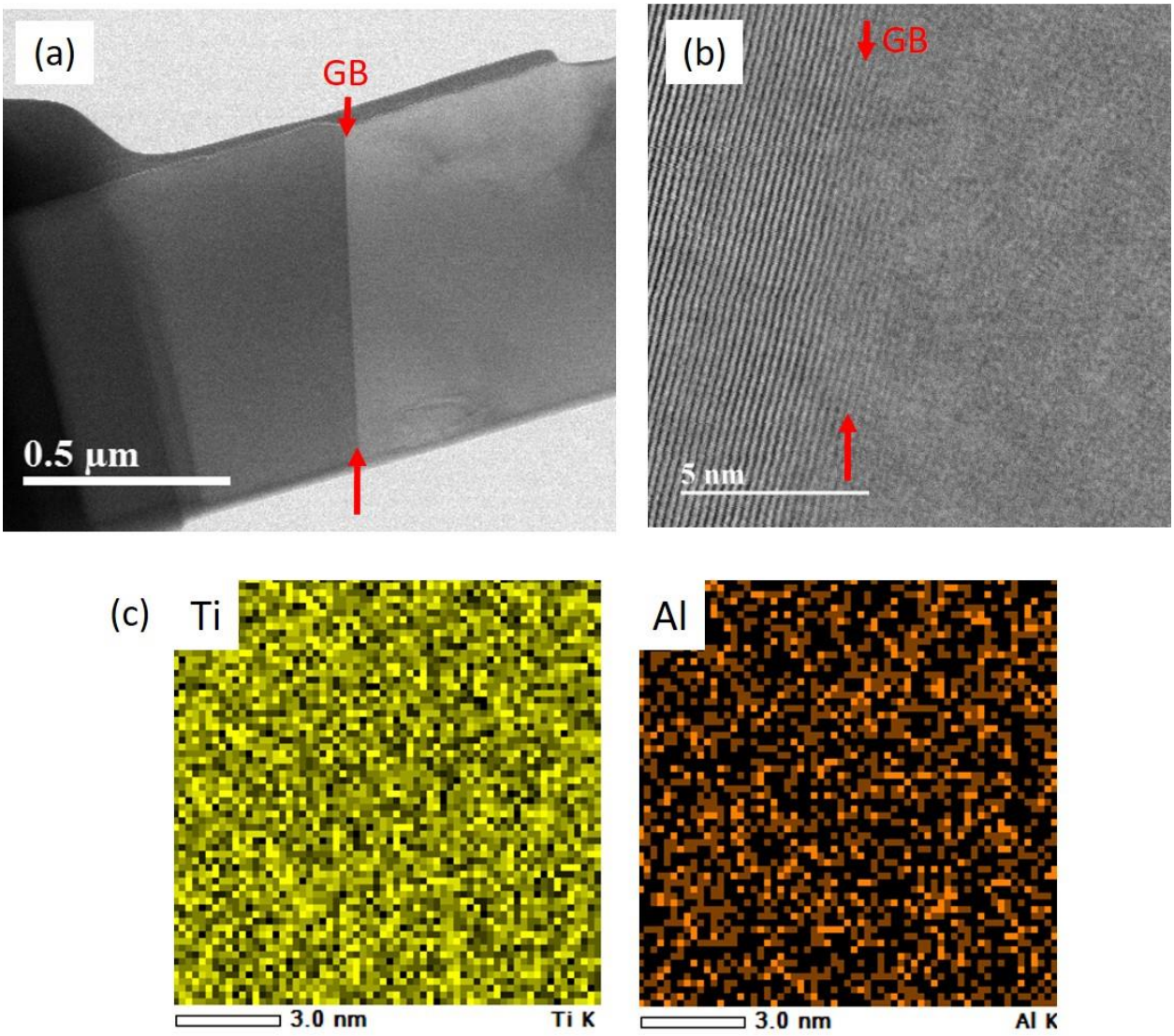

Figure 55. (a) Low magnification and (b) high magnification of a grain boundary in a fully recrystallized Ti-7wt%Al sample along with (c) the corresponding high magnification EDS maps for titanium and aluminum (imaging performed by Qianying Shi)

The segregation of solute atoms to the grain boundaries is determined by the segregation energy (also referred to as segregation enthalpy or binding energy), which describes how much more or less energetically favorable it is for solute atoms to sit at the grain boundaries compared to in the bulk. However, there are variations in literature about how segregation energy is defined and what factors affect it. Some models only include elastic distortion effects due to solute-solvent atomic size mismatch [29]–[31]. When a substitutional atom sits in a lattice of matrix atoms, the difference in atomic radii will cause elastic distortions and therefore a strain energy penalty. However, because a grain boundary is made up of dislocations and is not a perfect lattice, the elastic distortions due to solutes are smaller and thus a smaller energy penalty is imposed when solute atoms sit at a grain boundary. Therefore, the larger the difference in atomic radii and the greater the elastic distortion, the more the overall energy of the system will decrease if the solute atoms segregate at the grain boundaries. Other models also include chemical effects (atomic bonding) and interfacial effect (grain boundary energy) [32], [33]. These effects are taken into account by comparing the energy required for a bond between A-B atoms to the energy required for a bond between either A-A atoms or B-B atoms in the bulk or at a grain boundary [33]. However, these models generally assume a constant value of segregation energy independent of solute concentration in the alloy. This assumption does not take into account solute-solute interactions [34], [35]. While ignoring solute-solute interactions may be appropriate for dilute solutions (<1wt%) in which these interactions are negligible due to the distance between solute atoms, this effect cannot be ignored at higher solute concentrations. In alloys with higher solute concentrations, the solute atoms are closer to each other and the solute-solute interactions become stronger. The closer the solute concentration is to the solubility limit, the more energetically favorable it is for the solute atoms to be near each other, which leads to precipitation once the solubility limit is passed. Therefore, the more the solute atoms are attracted to each other and prefer to be near each other, the less energetically favorable it is for them to segregate at the grain boundaries. If it is unfavorable for segregation to occur, then the solute atoms “repel” the grain boundaries instead of being attracted to them. The notation for segregation energy varies in literature and in the current work we define a negative segregation energy to mean solute

atoms are attracted to the grain boundaries and segregation is likely to occur and we define a positive segregation energy to be the opposite. The approach for accounting for solute-solute interaction in models and the determination of its value also varies in literature. Peng et al. [35] defined segregation enthalpy, H_{seg}, to be a function of the solute concentration in the bulk, X^b, and in the grain boundaries, X^{GB}:

$$H_{seg} = H_0 - C_1 X^{GB} + C_2 X^b \quad (9)$$

where H_0 includes the elastic and grain boundary energy effects and C_1 and C_2 are constants. Therefore, a higher value of the bulk term than the grain boundary term in Eq 9 will create a positive H_{seg}, meaning segregation will not occur at high concentrations. Gong et al. [34] included an interaction term when calculating segregation enthalpy and, due to the difficulty in measuring it, used it as a fitting term. After fitting their model to experimental results for $Pd_{81}Zr_{19}$, the authors found an extremely low absolute value of segregation enthalpy. They attribute this low value to the very high Zr concentration in the alloy. Another approach to determining segregation energy is by using molecular dynamic simulations [24], [36]. This is done by running an atomistic simulation for diffusion both with solute atoms in the grain boundaries and with the solutes in the bulk at 850K and then temperature was then reduced to 0K. The difference in energy between those simulations at 0K divided by the number of solute atoms is used as the segregation energy. Sun et al. [24] used this method to determine the segregation energy of both Ni atoms and Ti in Al. They found a negative segregation energy for Ni in Al and a positive segregation energy for Ti in Al. Due to the lack of segregation, the effects of Ti on grain boundary mobility in Al were not investigated. This supports the common belief that segregation is required for a decrease in grain boundary mobility. Therefore, a unique aspect of the current work is investigating the effect of solutes on grain boundary mobility for the case of a high solute concentration and no observed segregation of solutes on grain boundaries.

The lack of Al segregation in both Ti-4wt%Al and Ti-7wt%Al can be explained by the tendency of Al atoms to remain near each other. In alloys with sufficiently high Al content this is demonstrated by the formation of the ordered α_2 phase, which has the Ti_3Al stoichiometry.

Ti-Al alloys are also known to exhibit short range ordering [37], [38]. This occurs when the Al atoms prefer to order rather than occupy random atomic positions. Short range ordering has been reported in Ti-Al alloys with Al concentrations of as low as 4wt% via electrical resistivity measurements [39]. Thus this ordered atomic configuration of Ti and Al atoms would tend to be preferred over segregation to the grain boundaries. Since significant solute effect on grain growth kinetics have been observed without any observable solute segregation, it is concluded that at aluminum concentrations of 4 and 7wt%, there is a positive segregation energy causing the solute atoms to repel the grain boundaries and decrease their mobility. In John Cahn's original paper on solute drag, he states that the equation for impurity drag, "is independent of the sign of E (binding energy), and predicts that drag for impurities that avoid the boundary is the same as it is for impurities that are adsorbed. The former are pushed ahead of the boundary; the latter are dragged along by the boundary. [20]" The results in this work not only confirm that a drag effect is seen in alloys with positive segregation energies and no solute segregation, but also that the linear relationship between inverse mobility and solute concentration holds true regardless of the sign of the segregation energy, as Cahn predicted.

5.5 Conclusions

- The grain growth kinetics of the three alpha titanium alloys studied follow a normal growth trend with rapid growth at early annealing times and slowing growth at longer annealing time approaching a constant grain size.
- The grain growth kinetics are significantly faster at higher annealing temperatures for all three alloys, which is expected due to increased diffusivity.
- The grain growth exponent for all alloys and annealing temperatures are substantially lower than the ideal value of 0.5. We attribute this to solute additions and the presence of a weak basal texture in the starting microstructure.
- The addition of aluminum to titanium significantly retards the grain growth kinetics and results in much smaller grain sizes at long annealing times.

- A linear relationship between the inverse mobility and aluminum solute concentration is observed, corresponding to the relationship predicted by the CLS model for solute drag.
- Due to the lack of observed grain boundary segregation, the effect of Al to retard grain boundary mobility is attributed to a process in which the grain boundary must push or repulse Al atoms forward in order to migrate. This effect is due to the preference for Al atoms to attract one another. This effect is indicated by short range order and precludes grain boundary segregation. This is consistent with the CLS model, however for the case of a positive segregation energy.

5.6 References

[1] C. J. Silva, A. Kula, R. K. Mishra, and M. Niewczas, “Grain growth kinetics and annealed texture characteristics of Mg-Sc binary alloys,” *J. Alloys Compd.*, vol. 687, pp. 548–561, 2016.

[2] S. K. Behera, “Kinetics of grain growth in La-doped ultrapure Al2O3,” *J. Alloys Compd.*, vol. 683, pp. 444–449, 2016.

[3] H. Kotan, K. A. Darling, and M. Saber, “Thermal stability and mechanical properties of nanocrystalline Fe – Ni – Zr alloys prepared by mechanical alloying,” *J. Mater. Sci.*, vol. 48, pp. 8402–8411, 2013.

[4] C. Qiu, H. S. Zurob, and C. R. Hutchinson, “The coupled solute drag effect during ferrite growth in Fe–C–Mn–Si alloys using controlled decarburization,” *Acta Mater.*, vol. 100, pp. 333–343, 2015.

[5] E. Hersent, K. Marthinsen, and E. Nes, “On the Effect of Atoms in Solid Solution on Grain Growth Kinetics,” *Metall. Mater. Trans. A*, vol. 45A, pp. 4882–4890, 2014.

[6] A. Karmakar, S. Kundu, S. Roy, S. Neogy, D. Srivastava, and D. Chakrabarti, “Effect of microalloying elements on austenite grain growth in Nb – Ti and Nb – V steels,” *Mater. Sci. Technol.*, vol. 30, no. 6, pp. 653–664, 2014.

[7] C. Qiu, H. S. Zurob, D. Panahi, Y. J. M. Brechet, and G. R. Purdy, “Quantifying the Solute Drag Effect on Ferrite Growth in Fe-C-X Alloys Using Controlled Decarburization Experiments,” *Metall. Mater. Trans. A*, vol. 44A, pp. 3472–3483, 2013.

[8] D.-G. Lee, C. Li, Y. Lee, X. Mi, and W. Ye, “Effect of temperature on grain growth kinetics of high strength Ti–2Al–9.2Mo–2Fe alloy,” *Thermochim. Acta*, vol. 586, pp. 66–71, Jun. 2014.

[9] F. J. Gil and J. A. Planell, “Behaviour of normal grain growth kinetics in single phase titanium and titanium alloys,” *Mater. Sci. Eng. A*, vol. 283, no. 1–2, pp. 17–24, May 2000.

[10] S. L. Semiatin, J. Soper, and I. Sukonnik, “Grain growth in a conventional titanium alloy during rapid, continuous heat treatment,” *Scr. Mater.*, vol. 30, no. 7, pp. 951–955, 1994.

[11] J. Fan, J. Li, H. Kou, K. Hua, B. Tang, and Y. Zhang, “Influence of solution treatment on microstructure and mechanical properties of a near b titanium alloy Ti-7333,” *Mater. Des.*, vol. 83, pp. 499–507, 2015.

[12] P. Xiaona, “Isothermal Beta Grain Growth Kinetics of TC4-DT Titanium Alloy under Two Different Prior Processing Conditions : Deformed vs . Undeformed,” *Rare Met. Mater. Eng.*, vol. 43, no. 8, pp. 1855–1861, 2014.

[13] F. J. Gil, J. A. Picas, J. M. Manero, A. Forn, and J. A. Planell, “Effect of the addition of palladium on grain growth kinetics of pure titanium,” *J. Alloys Compd.*, vol. 260, no. 1–2, pp. 147–152, Sep. 1997.

[14] J.-W. Lu, Y.-Q. Zhao, P. Ge, and H.-Z. Niu, “Microstructure and beta grain growth behavior of Ti–Mo alloys solution treated,” *Mater. Charact.*, vol. 84, no. 96, pp. 105–111, Oct. 2013.

[15] B. Cherukuri, R. Srinivasan, S. Tamirisakandala, and D. B. Miracle, “The influence of trace boron addition on grain growth kinetics of the beta phase in the beta titanium alloy Ti–15Mo–2.6Nb–3Al–0.2Si,” *Scr. Mater.*, vol. 60, no. 7, pp. 496–499, 2009.

[16] A. Trump and J. Allison, “The influence of aluminum content and annealing temperature on static recrystallization in α-titanium alloys,” 2016.

[17] J. E. Burke and D. Turnbull, “Recrystallization and grain growth,” *Prog. Met. Phys.*, vol. 3, pp. 220–292, 1952.

[18] F. J. Humphreys and M. Hatherly, *Recrystallization and Related Annealing Phenomena*, 2nd ed. Elsevier Science, 2004.

[19] M. S. Wu, A. A. Nazarov, and K. Zhou, “Misorientation dependence of the energy of symmetrical tilt boundaries in hcp metals : prediction by the disclination-structural unit model,” *Philos. Mag.*, vol. 84, no. 8, pp. 785–806, 2004.

[20] J. W. Cahn, “The impurity-drag effect in grain boundary motion,” *Acta Mater.*, vol. 10, pp. 789–798, 1962.

[21] K. Lucke and H. P. Stuwe, “On the theory of impurity controlled grain boundary motion,” *Acta Metall.*, vol. 19, pp. 1087–1099, 1971.

[22] P. Gordon and R. Vandermeer, “The mechanism of boundary migration in recrystallization,” *Trans. Metall. Soc. AIME*, vol. 224, pp. 917–929, 1962.

[23] Y. Huang and F. J. Humphreys, “The effect of solutes on grain boundary mobility during recrystallization and grain growth in some single-phase aluminium alloys,” *Mater. Chem. Phys.*, vol. 132, no. 1, pp. 166–174, 2012.

[24] H. Sun and C. Deng, “Direct quantification of solute effects on grain boundary motion by atomistic simulations,” *Comput. Mater. Sci.*, vol. 93, pp. 137–143, 2014.

[25] J. D. Robson, S. J. Haigh, B. Davis, and D. Griffiths, “Grain Boundary Segregation of Rare-Earth Elements in Magnesium Alloys,” *Metall. Mater. Trans. A*, vol. 47, no. 1, pp. 522–530, 2015.

[26] J. Takahashi, J. Haga, K. Kawakami, and K. Ushioda, “Observation of co-segregation of titanium and boron at the interface between recrystallized and unrecrystallized grains in cold-rolled interstitial-free steel sheets,” *Ultramicroscopy*, vol. 159, pp. 299–307, 2015.

[27] H. Van Landeghem, B. Langelier, D. Panahi, G. R. Purdy, C. R. Hutchinson, G. A. Botton, and H. S. Zurob, “Solute Segregation During Ferrite Growth : Solute / Interphase and Substitutional / Interstitial Interactions,” *JOM*, vol. 68, no. 5, pp. 1329–1334, 2016.

[28] Z. Chen, Y. Y. Tang, Q. Tao, Q. Chen, and T. Liang, “The mechanism of grain growth and thermal stability in Ni-1 at .% Pb alloy,” *J. Alloys Compd.*, vol. 662, pp. 628–633, 2016.

[29] Z. Aretxabaleta, B. Pereda, and B. López, “Analysis of the Effect of Al on the Static Softening Kinetics of C-Mn Steels Using a Physically Based Model,” *Metall. Mater. Trans. A*, vol. 45, no. 2, pp. 934–947, Oct. 2013.

[30] M. K. Rehman and H. S. Zurob, “A Novel Approach to Model Static Recrystallization of Austenite During Hot Rolling of Nb Microalloyed Steel. Part I: Precipitate-Free Case,” *Metall. Mater. Trans. A*, vol. 44, no. 4, pp. 1862–1871, Nov. 2012.

[31] W. U. Chuan, Y. He, L. I. Hongwei, and F. A. N. Xiaoguang, “Static coarsening of titanium alloys in single field by cellular automaton model considering solute drag and anisotropic mobility of grain boundaries,” *Chinese Sci. Bull.*, vol. 57, no. 13, pp. 1473–1482, 2012.

[32] T. Chookajorn and C. A. Schuh, “Nanoscale segregation behavior and high-temperature stability of nanocrystalline W – 20 at .% Ti,” *Acta Mater.*, vol. 73, pp. 128–138, 2014.

[33] T. Chookajorn and C. A. Schuh, “Thermodynamics of stable nanocrystalline alloys : A Monte Carlo analysis,” *Phys. Rev. B*, vol. 89, 2014.

[34] M. M. Gong and R. H. R. C. F. Liu, “Modeling grain growth kinetics of binary substitutional alloys by the thermodynamic extremal principle,” *J. Mater. Sci.*, vol. 50, pp. 4610–4621, 2015.

[35] H. Peng, Y. Chen, and F. Liu, “Effects of Alloying on Nanoscale Grain Growth in Substitutional Binary Alloy System : Thermodynamics and Kinetics,” *Metall. Mater. Trans. A*, vol. 46, no. 11, pp. 5431–5443, 2015.

[36] H. Sun and C. Deng, “Adapted solute drag model for impurity-controlled grain boundary motion,” *J. Mater. Res.*, vol. 29, no. 12, pp. 1369–1375, Jul. 2014.

[37] T. Neeraj and M. J. Mills, “Short-range order (SRO) and its effect on the primary creep behavior of a Ti – 6wt% Al alloy,” *Mater. Sci. Eng. A*, vol. 321, pp. 415–419, 2001.

[38] H. Wood, G. D. W. Smith, and A. Cerezo, “Short range order and phase separation in Ti – Al alloys,” *Mater. Sci. Eng. A*, vol. 250, pp. 83–87, 1998.

[39] T. Namboodhiri, C. McMahon, and H. Herman, “Decomposition of the α-phase in titanium-rich Ti-Al alloys,” *Metall. Mater. Trans.*, vol. 4, no. 5, pp. 1323–1331, 1973.

Chapter 6. Conclusions and Future Work

6.1 Conclusions

The static recrystallization kinetics in binary Ti-Al alloys were analyzed by quantifying the area of recrystallized grains throughout the recrystallization process. An EBSD grain orientation spread method was used for this characterization. Recrystallization kinetics were characterized for pure titanium at three different annealing temperatures and it was found that decreasing the annealing temperature slowed down the recrystallization kinetics exponentially. Decreasing the annealing temperature from 800°C to 500°C increased the time to 50% recrystallization from less than a minute to 6060 minutes. This can be explained by a slower diffusion rate at lower temperatures decreasing the mobility of the high angle grain boundaries surrounding the recrystallized grains. The relationship between $t_{0.5}$ and annealing temperature was then used to calculate the activation energy for static recrystallization in pure titanium, which was found to be consistent with that of bulk-self diffusion of titanium. Therefore, the rate of recrystallization is dependent on the diffusivity of titanium atoms in the bulk alpha titanium.

The same technique was then used to study the effect of aluminum concentration on the static recrystallization kinetics. Similar to decreasing the annealing temperature, increasing the aluminum content significantly slowed the recrystallization kinetics. Increasing the aluminum concentration from 0wt% to 7wt% increased the time to 50% recrystallization from less than 1 minute to 1240 minutes. An analytical model was used to capture this solute effect. The model chosen used a JMAK based framework equation that included both driving force and mobility. The effect of solute concentration on grain boundary mobility was captured using Cahn's model for solute drag that predicts a linear relationship between inverse mobility and

solute concentration. If mobility alone is changed with respect to aluminum concentration, the model underestimates $t_{0.5}$. However, by accounting for the decrease in driving force that occurs with increasing aluminum concentration, the trend in $t_{0.5}$ is predicted very well. Therefore, we can conclude that the retardation in recrystallization is due to a combination of two factors, a reduction in driving force and a reduction in grain boundary mobility with the addition of aluminum. The reduction in driving force is due to a lower work hardening rate with increasing aluminum content. Adding aluminum solute atoms suppresses twinning in alpha titanium and twin boundaries hinder dislocation motion, leading to dislocation pile ups around them. Therefore, a lower twin density leads to a lower dislocation density for a given strain and a lower driving force for recrystallization.

The overall texture was measured before and after deformation and throughout the recrystallization process. A fairly random texture was seen before deformation while a strongly basal texture in the direction of the compression axis was seen after deformation. Therefore, the basal poles are rotating towards the compression direction. This basal texture was then seen to weaken during recrystallization but was not removed. This remaining basal texture shows that the recrystallized grains are not nucleating with a random texture, but rather take on a similar texture as their parent grain.

The static recrystallization kinetics were quantified using the JMAK relationship and the alloys studied all exhibited recrystallization behavior resulting in an Avrami exponent of approximately one. This differs from the theoretical value of 3, which is derived based on the assumptions of site-saturated nucleation and a constant growth rate throughout recrystallization. It is concluded that the resulting Avrami exponent of one is attributed to a decreasing growth rate for recrystallized grains due to an inhomogeneous distribution of nuclei and stored energy. This is due to both the impingement of recrystallized grains and the transition from high to low stored energy regions. This conclusion was then verified by quantifying the distribution of nucleation by measuring the free surface fraction, S_v, throughout recrystallization. A random distribution of nuclei will produce a symmetric curve about 50% recrystallization, however the results for all three alloys showed an asymmetric curve with the peak values of S_v occurring below 50%. This reduced peak value of SV is due to the

impingement of clustered nuclei that occur at shorter times and earlier in the recrystallization process than that of randomly distributed nuclei.

These results were also validated by phase field simulations for recrystallization. Changing the distribution of stored energy from random to non-random in the phase field simulation decreased the Avrami exponent only slightly. Therefore, while an inhomogeneous distribution of stored energy may alter the growth rate, it is concluded that stored energy alone is not sufficient to explain the low experimental Avrami exponents. The phase field simulations were then set up with the initial nuclei clustered into a planar region within the initial microstructure and the Avrami exponent was lowered to 1.2, matching the experimental results. Therefore, the combination of inhomogeneous distributions of nuclei and inhomogeneous stored energy accurately simulate the experimentally observed recrystallization kinetics as captured by the Avrami exponent. Of these two factors the clustering of nucleation sites is a much more significant factor.

The grain growth kinetics in fully recrystallized alloys were studied using optical microscopy and were found to follow a normal growth trend with rapid growth at early annealing times and slowing growth at longer annealing times due to a decreasing driving force. The grain growth kinetics are significantly faster at higher annealing temperatures for all three alloys, which is expected due to increased diffusivity. While the grain growth exponent for an ideal material is expected to be 0.5, the measured exponents for all of the studied alloys were found to be less than 0.5. This result is constant with literature and is attributed to solute additions and the presence of a weak basal texture in the starting microstructure. The addition of aluminum is seen to significantly retard the grain growth kinetics and results in much smaller grain sizes at long annealing times. This is generally attributed to the solute drag effect. However, no aluminum segregation is observed in grain boundaries these alloys. It is concluded that the tendency for short-range ordering of Al atoms precludes grain boundary segregation, which would tend to randomize the Al sites. In Ti-Al alloys, short range ordering has been seen in aluminum concentrations as low as 4wt%. With increasing amounts of aluminum, this ordering eventually leads to α_2 precipitation. These solute-solute interactions cause the solute atoms to prefer not to segregate at the grain boundaries and, therefore, solutes must be

pushed ahead of the migrating grain boundaries in ordered sites, decreasing the grain boundary mobility.

The measured grain growth kinetics were then used to calculated the change in grain boundary mobility with respect to aluminum concentration. A linear relationship was seen between the inverse mobility and aluminum concentration, matching the relationship predicted by Cahn. This trend was also used in the static recrystallization model that correctly captured the experimental results. Cahn predicted that this relationship would hold true regardless of the direction of the solute drag force. Therefore, this work is novel in studying the "solute drag" effect at high solute concentrations in both recrystallization and grain growth along with also validating Cahn's model for the case of solute repulsion (vs drag) without grain boundary segregation.

6.2 Future Work

Further investigations should be done in order to support the conclusion that the aluminum atoms in alpha titanium are avoiding the grain boundaries at high concentrations and are therefore pushed ahead of the migrating boundaries, decreasing the grain boundary mobility. A possible method for investigating this is altering the oxygen content in the alloys. In alpha titanium, oxygen enhances short range ordering. Therefore, the oxygen content can be increased to enhance short range ordering and the effect on the kinetics will be studied. If the kinetics slow down, then the hypothesis that short range ordering causes the Al atoms to repel the grain boundaries will be supported.

An important next step in this research is to quantify the static recrystallization and grain growth kinetics in binary Ti-Al alloys with lower aluminum concentrations such as 1wt% or 2wt%. This will add more information between 0wt% and 4wt% to clarify trends with respect to aluminum concentration, allowing for the extrapolation of the current findings to lower solute levels. These trends include $t_{0.5}$, driving force, and grain boundary mobility for recrystallization along with grain boundary mobility for grain growth. It would also be valuable

to experimentally determine whether or not solute segregation occurs at lower concentrations. It is hypothesized that segregation would occur at low concentrations based on the lack of experimental evidence that short range ordering occurs at these concentrations and based on the relatively large difference in atomic radii between aluminum and titanium. If segregation does occur at these lower concentration levels, it would allow understanding of how segregation affects classical solute drag versus the repulsion we hypothesize occurs at higher concentrations.

The forged material used in this research lead to a very non-uniform starting material, both in texture and stored energy, along with a complicated starting microstructure. This caused some difficulties including variability from sample to sample that created scatter in the recrystallization results. Also, a complicated and non-equiaxed microstructure is difficult to simulate in computational models. For these reasons, another plan for future work includes studying static recrystallization in the same alloys, but with a more uniform starting material. This might be achieved by hot deformation below the beta transus to achieve a partially recrystallized structure and cross rolling to achieve a more uniform texture and distribution of stored energy. This would provide an opportunity to heat treat the material in order to more carefully control the starting microstructure. Recrystallization studies on alloys with a more uniform microstructure will allow for a more detailed analysis on the effects of starting microstructure on recrystallization kinetics including the slope as defined by the Avrami exponent. It would also allow for more clear visualization of nuclei and therefore analysis of where nucleation is occurring.

The influence of alloying on dynamic recrystallization is another important topic to study This would entail hot deformation of these alloys and the effects that thermomechanical processing parameters such as strain, strain rate, and temperature along with alloy composition have on the dynamic recrystallization kinetics. These tests could be performed using a Gleeble thermomechanical simulator and the results used to develop constitutive models that can be used to predict the effects of processing variables. These results could also be used to further develop and validate both crystal plasticity and phase field models as part of larger ICME efforts.